

Copyright

by

Javier Mateo Solis

2005

**Development and Testing of a Track-Terrain Interaction
Model for Planar Motion Analysis of a Robotic Tracked
Vehicle**

by

Javier Mateo Solis, B.S.M.E

Thesis

Presented to the Faculty of the Graduate School of

The University of Texas at Austin

in Partial Fulfillment

of the Requirements

for the Degree of

Master of Science in Engineering

The University of Texas at Austin

May 2005

Development and Testing of a Track-Terrain Interaction Model for Planar Motion Analysis of a Robotic Tracked Vehicle

**Approved by
Supervising Committee:**

Raul G. Longoria, Supervisor

S.V. Sreenivasan

To my family

Acknowledgments

I would like to first and foremost thank Dr. Raul G. Longoria for his guidance, confidence, and generosity. He has served as my mentor and has inspired me to further my education. I would also like to thank Dr. S.V. Sreenivasan for his examination of my thesis. I owe many thanks to the faculty and staff at the University of Texas Pan American for their recommendations and for encouraging me to pursue graduate study. I would like to thank my family and friends for their love and support. Many thanks go to the Southwest Research Institute and UDLP, for their financial support.

JAVIER MATEO SOLIS

The University of Texas at Austin

May 2005

Development and Testing of a Track-Terrain Interaction Model for Planar Motion Analysis of a Robotic Tracked Vehicle

Javier Mateo Solis, M.S.E

The University of Texas at Austin, 2005

Supervisor: Raul G. Longoria

This thesis describes the formulation and evaluation of a dynamic model for predicting the mobility of a robotic tracked vehicle on flat two-dimensional terrains. The model relies on simplified predictions of track-terrain interaction, facilitating computationally efficient estimates of motion on both deformable and non-deformable terrains. A major contribution of this thesis is the development and implementation of a new approach to modeling track-terrain interaction, in which the track-terrain interface continuum is approximated by discretized parameterizable force elements. Normal and shear forces acting at the track-terrain interface are modeled using classical soil mechanics equations, such as Bekker and Jansoi correlations. Nominal parameter data, obtained from the literature, is used to characterize the response of the terrain. A kinematic model taking the form of a partial differential equation for shear displacement is approximated by a series of ordinary differential equations. The steady-state response predicted by this model is theoretically exact, but the transient response is relatively slow.

To demonstrate the applicability of this approach, a model of the test vehicle is constructed using solid modeling software and integrated into a commercial multi-

body dynamics software environment. The main components of the system model include the main-body, tracks, terrain, and a dual motor and drive train system. The track-terrain interaction forces acting on the system and the equations of motion are evaluated and numerically solved simultaneously. Vehicle maneuvers can be specified by driver inputs conveyed as individual drive motor voltage signals. In order to validate this model, physical tests were conducted with an iRobot PackBot at Southwest Research Institute's robotic vehicle test range. The PackBot was driven on asphalt and dry sand, and the test vehicle was subjected to four different types of maneuvers: go-and-stop, j-turn, double-lane-change, and zero radius turn. Measurements were made of the vehicle's ideal forward velocity, yaw angular velocity and the currents supplied to the motors. The simulated results on asphalt match very well with those obtained from field tests providing some validation that this vehicle model can be effective for motion analysis on flat non-deformable terrains. The simulated results on dry sand also match well with those obtained from field tests, with the exception of the zero radius turn maneuver. As expected, the effect of slip-sinkage gives rise to a bulldozing effect and has a profound impact on the motion of the test vehicle for large radius turn maneuvers. These effects are neglected in the vehicle model yielding unrealistic results for large radius turn maneuvers. Parametric studies were conducted to observe the sensitivity of the vehicle model to the change in terrain parameters. This analysis shows that the lateral force model can greatly affect the response of the vehicle model. Planned extensions to this model include improving the lateral force model, and extending the model formulation for three-dimensional terrain environments.

Contents

Acknowledgments	v
Abstract	vi
List of Tables	xiii
List of Figures	xiv
Chapter 1 Introduction	1
1.1 Background and Motivation	1
1.2 Previous Works	6
1.3 Problem Statement	9
1.4 Thesis Contributions	10
1.5 Thesis Outline	10
Chapter 2 Classical Mechanics of Track-Terrain Interaction	12
2.1 Introduction	12
2.2 Methods for Predicting Track-Terrain Interaction	13
2.2.1 Analytical Methods	13
2.2.2 Empirical Methods	17
2.2.3 Parametric Methods	18

2.3	Measurement and Characterization of Terrain Response Using the Bevameter Technique	21
2.3.1	Pressure-Sinkage Relationship	22
2.3.2	Shear Stress-Shear Displacement Relationship	26
2.4	Mechanics of Track-Terrain Interaction	31
2.4.1	Introduction	31
2.4.2	Motion Resistance of the Track and the “Bulldozing” Effect .	32
2.4.3	Tractive Effort Developed by the Track	35
2.5	Conclusion	39

Chapter 3	A Mathematical Model to Approximate Track-Terrain Interaction	40
3.1	Introduction	40
3.2	Overview Of Vehicle Model	41
3.3	The Discrete Approach to Modeling the Dynamics at the Track-Terrain Interface	43
3.3.1	Motivation	44
3.3.2	Concept of Discrete Approach	46
3.4	Modeling of the Dynamics at the Track-Terrain Interface Using the Discrete Concept	50
3.4.1	Discrete Normal Force Distribution Underneath the Track . .	50
3.4.2	Development of Kinematical Model for Longitudinal Shear Displacement	56
3.4.2.1	Base-Line Equations for Modeling Longitudinal Shear Displacement	56
3.4.2.2	Defining the Value of z^* To Satisfy Boundary Conditions	60

3.4.2.3	Implementing Longitudinal Shear Displacement Model in ADAMS	63
3.4.3	Model Derivation of Longitudinal Shear Forces	66
3.4.3.1	Baseline Equations for Modeling Longitudinal Shear Forces	66
3.4.3.2	Implementing Longitudinal Force Model In ADAMS	68
3.4.4	Development of Kinematical Model for Lateral Shear Dis- placement	70
3.4.4.1	Baseline Equations for Modeling Lateral Shear Dis- placement	71
3.4.4.2	Modifying Dynamic Model of Lateral Shear Displace- ment to Satisfy Boundary Conditions	73
3.4.4.3	Implementing Lateral Shear Displacement Model In ADAMS	75
3.4.5	Model Derivation of Lateral Shear Forces	76
3.4.5.1	Baseline Equations for Modeling Lateral Shear Forces	76
3.4.5.2	Implementing Lateral Force Model Into ADAMS . .	77
3.4.6	Resistive Forces	77
3.4.6.1	Implementing Motion Resistance Model Into ADAMS	79
3.5	Summary of Limiting Assumptions Made for Track-Terrain Model .	80
3.6	Conclusion	84

Chapter 4 Modeling and Testing of Power System and Description

	of Field Test Experiments	87
4.1	Introduction	87
4.2	Physical Description of Actual Robotic Tracked Vehicle	88
4.3	Motor and Drive Train Model	90
4.3.1	Description of Motor and Drive Train Model	90

4.3.2	Experimental Motor and Drive Train Tests	95
4.3.3	Verifying Motor and Drive Train Model	98
4.4	Field Test Experiments	100
4.5	Conclusion	102
Chapter 5	Simulation Results and Discussion	103
5.1	Introduction	103
5.2	Simulation Environment in ADAMS	103
5.3	Simulation Results and Comparisons	105
5.3.1	Go-Stop Maneuver	106
5.3.2	J-turn Maneuver	112
5.3.3	Double-Lane-Change Maneuver	114
5.3.4	Zero Radius Turn Maneuver	117
5.4	Parametric Analysis	120
5.4.1	Sensitivity of Speed to Current	120
5.4.2	Effects of Perturbations in Terrain Parameters	126
5.5	Conclusion	136
Chapter 6	Conclusion and Recommendation for Future Work	138
6.1	Future Work	140
6.1.1	Shear Displacement Model	140
6.1.2	Lateral Force Model and Slip-Sinkage	141
6.1.3	Internal Resistance of Track	142
6.1.4	Test Vehicle	142
6.2	Conclusion	143
Appendix A	Specifications of PackBot	144

Appendix B Derivation of Motor and Drive Train Model	146
B.1 Deriving the Effective Inertias of Motor/Drivetrain System	146
Appendix C Extended Information for Chapter 3	153
C.1 Validation of Lateral Shear Displacement Model	153
C.2 Dimensions of Discretized Track-Terrain Interface	156
C.3 Values for Computational Based Parameters	157
Appendix D Sensitivity of Vehicle Response to the Change in Terrain	
Parameters	158
Bibliography	162
Vita	165

List of Tables

3.1	One-sided Impact Parameters	55
3.2	List of Model Based Parameters	86
3.3	List of Computational Based Parameters	86
4.1	Estimated Values for Friction Parameters	97
5.1	Nominal Terrain Parameters for Dry Sand	105
5.2	Nominal Terrain Parameters for Asphalt	105
5.3	Estimated Values for Internal Track Damping Coefficient on Dry Sand and Asphalt	106
5.4	Estimated Values for the Modified Internal Resistance Parameter b_{int}^* on Dry Sand and Asphalt	125
5.5	Nominal Values for Terrain Parameters for Various Sands [1]	126
5.6	Values of Terrain Parameters Used for Sensitivity Analysis	129
B.1	Motor Data	151
B.2	Inertia Values of Motor, Drive Train, and Track Components	152
B.3	Values for Motor, Drive Train, and Track Parameters	152
C.1	Values for Computational Based Parameters	157

List of Figures

2.1	Stress-Strain Behavior of an Ideal Elastoplastic Material	14
2.2	Finite Element Mesh, from [20]	16
2.3	The Basic Components of a Cone Penetrometer, from [21]	17
2.4	Various Ideal Normal Pressure Distributions Underneath a Track, from [22]	19
2.5	Measured Normal Pressure Distributions Below the Surface Under Various Tracked Vehicles, from [2]	20
2.6	Schematic View of a Bevameter for Measuring Terrain Properties, from [6]	22
2.7	Response of a Sandy Soil to Repetitive Normal Loading	25
2.8	Shear Stress vs. Shear Displacement Relationship for Plastic Soils .	27
2.9	Shear Strength of Ideal Cohesive and Noncohesive Soils, modified from [2]	28
2.10	Shear Strength Relationship of Common Soils	29
2.11	Shear Stress-Shear Displacement Relationship of Elastic and Organic Terrains	30
2.12	Resistive Forces Acting on a Tracked Vehicle Arising From Sinkage .	32
2.13	Computing the Bulldozing Resistance Using Principles Based on Earth Pressure Theory	34

2.14	Development of Shear Displacement Underneath a Track, modified from [2]	36
2.15	Shear Displacement Distribution Under Steady-State Conditions	37
3.1	Solid Model of PackBot Integrated Into ADAMS Environment	41
3.2	Model Scheme Implemented in ADAMS Environment	42
3.3	Different Approaches to Modeling Track-Terrain Interaction	44
3.4	Illustration of Discrete Approach	47
3.5	Approximating the Area Under a Curve Using a Riemann Sum	49
3.6	Flow Diagram for Modeling the Forces at the Track-Terrain Interface	51
3.7	One-Sided Impact Model Used in ADAMS to Compute Normal Forces Acting on Discrete Elements	53
3.8	Longitudinal Shear Displacement Developed Underneath Track	56
3.9	Longitudinal Shear Displacement Increasing Linearly Along the Track	58
3.10	Top View of Partitioned Contact Patch	61
3.11	Determining the Position of Track Frame	62
3.12	Illustration of STEP5 Function	65
3.13	Modified Longitudinal Shear Displacement Modeled Using the STEP5 Function in ADAMS	66
3.14	Forces Applied at the Origin of the Wheel's Reference Frame	68
3.15	Implementation of Longitudinal Forces In ADAMS Using the STEP5 Function	69
3.16	Lateral Shear Displacement Developed Underneath Track	72
3.17	Analogy to Describe Lateral Shear Displacement	74
3.18	Resistive Forces Acting on Track	80
3.19	Illustration of Motion Resistive Force Implemented Into ADAMS	81
4.1	PackBot System	88

4.2	Illustration of Power System Components and Model	91
4.3	Reduced Bond Graph of Motor and Drive Train Model	92
4.4	Experimental Tests Conducted to Obtain Unknown Friction Parameters	96
4.5	Estimating the Steady State Torque	97
4.6	Results of Experimental Tests to Estimate the Values for the Friction Parameters b_{eff} and τ_{stick}	98
4.7	Input Motor Voltage Profile	99
4.8	Comparisons of Motor and Drive Train Simulation Results and Ex- perimental Results	99
4.9	Various Maneuvers Performed to Verify Vehicle Model	100
4.10	Terrains Used to Conduct Maneuver Tests	101
5.1	ADAMS Modeling and Simulation Environment	104
5.2	Comparisons of Simulation Results and Field Test Results for Go- Stop Maneuver on Dry Sand	107
5.3	Comparisons of Simulation Results and Field Test Results for Go- Stop Maneuver on Asphalt	111
5.4	Comparisons of Simulation Results and Field Test Results for J-turn Maneuver on Dry Sand	113
5.5	Comparisons of Simulation Results and Field Test Results for J-turn Maneuver on Asphalt	115
5.6	Comparisons of Simulation Results and Field Test Results for Double- Lane-Change Maneuver on Dry Sand	116
5.7	Comparisons of Simulation Results and Field Test Results for Double- Lane-Change Maneuver on Asphalt	118
5.8	Comparisons of Simulation Results and Field Test Results for Zero Radius Turn Maneuver on Dry Sand	119

5.9	Comparisons of Simulation Results and Field Test Results for Zero Radius Turn Maneuver on Asphalt	121
5.10	Comparisons of Simulation Results and Field Test Results for Go-Stop Maneuver on Dry Sand. The steady-state speed of the vehicle is 2 m/s	123
5.11	Simulations Results Showing the Sensitivity of Ideal Speed to Current	124
5.12	Simulation Results for Go-Stop Maneuver on Sand Using Modified Internal Track Resistance Model	125
5.13	Simulation Results for Go-Stop Maneuver on Sand Using Modified Internal Track Resistance Model. The steady-state speed of the vehicle is 2 m/s	127
5.14	Simulation Results for Double Lane Change Maneuver on Sand Using Modified Internal Track Resistance Model	128
5.15	Simulated Trajectories of Vehicle Model for Various Sandy Terrains .	129
5.16	Sensitivity Response of Vehicle Model to Changing Cohesion, c . . .	130
5.17	Sensitivity Response of Vehicle Model to Changing Angle of Internal Shearing Resistance, ϕ	132
5.18	Sensitivity Response of Vehicle Model to Changing Shear Deformation Modulus, K	133
5.19	Sensitivity Response of Vehicle Model to Changing Internal Track Resistance, b_{int}^*	134
5.20	Steady-State Parametric Analysis	135
A.1	Geometric Dimensions of PackBot	145
B.1	Track/Drive-train Components	147
B.2	Bond Graph of Motor and Drive Train System	147

C.1	Characterizing the Lateral Shear Displacement Using the Eulerian Viewpoint for Modeling Track-Terrain Interaction	154
C.2	Discretizing of Contact Patch for PackBot Track-Terrain Interaction Model	156
D.1	Forces Acting on a Single Track	159

Chapter 1

Introduction

1.1 Background and Motivation

The mobility performance of a tracked vehicle is greatly influenced by the manner in which the vehicle interacts with the terrain. Understanding the mechanics of the vehicle-terrain interaction is essential for the proper selection of vehicle configuration and design parameters needed to meet specific operational requirements [1]. Consequently, a great deal of studies have been conducted to quantify the complex phenomenon involving the interaction between the dynamics of a vehicle and the properties of various terrains. These efforts have contributed to mathematical models that provide valuable information for predicting the performance of tracked vehicles. “From these models stem the definition of design and performance parameters, which in turn, yield themselves to the optimization of vehicle concept, in the so-called definition phase.”[2]

With increasing demands to improve the relationship between payload and vehicle weight, transport productivity, power efficiency and ride quality over rough terrain, there is a need to broaden the understanding of what vehicle parameters affect the tractive performance of tracked vehicles and how [3]. However, the analysis

and design of tracked vehicles is time-intensive and often requires testing of physical prototypes. The use of physical prototypes is often expensive and is limited due to the difficulties in varying the parameters in a controlled and simple manner, especially when tests must be conducted in the field away from the laboratory. With the utilization of mathematical models, virtual experiments can be conducted quickly, in which several parameters can easily be controlled to any desired specification; thus, the amount of field tests required can be minimized to facilitate production and reduce development costs.

During the past few decades, many mathematical models have been integrated into the design process to analyze the performance of tracked vehicles prior to field-testing and the final design. In particular, tracked vehicle modeling has been mainly dealt within the literature with three different goals [4]:

1. analysis of steerability
2. analysis of ride characteristics
3. theoretical prediction of ground pressure distribution and tractive performance.

In the first case, the motion of the vehicle is modeled in a horizontal plane in order to investigate the steering dynamics of the vehicle. There are several methods that can be used to accomplish the steering of tracked vehicles, which include skid-steering, articulated steering and curved track steering. Among these, skid-steering is probably the most widely used due to its simplicity in design. In skid-steering, the thrust of one track is increased while the other is reduced or fully braked, in order to generate a turning moment to overcome both the moment of turning resistance developed by the sliding of the tracks on the ground and the rotational inertia of the vehicle in yaw. However, experimental evidence has shown that the magnitude of the moment of turning resistance that must be overcome to turn the vehicle

can be considerably large resulting in significant power losses. Therefore, studies have been conducted using mathematical models to analyze how factors such as the terrain, design of the track and the motion of the vehicle influence the magnitude of the moment of turning resistance in order to maximize the power efficiency of the vehicle during skid-steering operation.

Another major issue often studied in the first case is the analysis of controllability and stability of tracked vehicles operating at high speeds. In recent years, the operational running speed of tracked vehicles has greatly increased due to the development of more powerful engines. Studies have shown that tracked vehicles have peculiar steering characteristics such as oversteering and response delay when operating at high speeds, which greatly affects their stability and control performance [5]. In order to explain the steering behavior of tracked vehicles operating at high speeds, the effects of the fundamental parameters such as vehicle speed, steering ratio, adhesion of track-ground contact area and steering mode of input are investigated using both experimental tests and computer simulations.

In the second case, the attention is focused on the ride dynamics response (vibrations) in a vertical plane. The terrain is assumed to be non-deformable with the vehicle moving horizontally forward at constant speed. The suspension system of the vehicle is studied to improve the comfort level for passengers and to prevent high acceleration levels from damaging weapons and instruments on board the vehicle. Finally in the third case, the objective is to predict the ground pressure distribution along the track and the tractive effort as a function of the track slip. Assuming stationary motions, a detailed model of the track-terrain interaction is performed to investigate different track configurations to optimize the tractive efficiency of the vehicle.

Although there have been considerable efforts devoted to the study of tracked vehicle dynamics in off-road applications, little has been added during the past few

years on the mathematical modeling or to support the experimental determination of the obstacle performance of tracked vehicles. In practical off-road applications, the vehicle is subject not only to various soils, but also obstacles such as large rocks and different sizes of crests and troughs that often impose severe limitations to the mobility of the vehicle. Most often under such situations the issues of vehicle speed or vibrations may rank lower than the issue of a “go or no go” consideration [6]. Preliminary studies found in the literature on analyzing the obstacle performance of tracked vehicles have mainly focused on three different types of obstacles:

1. step-obstacle
2. ditch-crossing
3. slope-climbing

In the first case, the step-obstacle is typically modeled as a non-deformable vertical wall. Because such an obstacle is usually approached with a minimum speed or acceleration, equations of equilibrium rather than motion are applied to obtain a solution. A complete clearance over a step obstacle first requires that the front end of the vehicle overcome the obstacle. In this stage of the analysis the minimum coefficient of friction is formulated from the equations of equilibrium [7, 8]. Once, the front end of the tracked vehicle overcomes the step, a complete obstacle clearance requires that the center of gravity be passed in a stable fashion. In this stage of the analysis, analytical models using a geometrical approach are used to calculate the maximum height the vehicle can overcome [9].

In the second case, the ditch-obstacle is modeled as a non-deformable horizontal cavity. The success in overcoming this obstacle is based on the initial velocity of the vehicle at the take-off point and the clearance of the vehicle with respect to the terrain. Studies in this area provide information for the maximum length ditch the vehicle can overcome for given conditions. In the last case, analysis of the tracked

vehicle is conducted in order to determine if the vehicle can overcome a given slope without stalling the vehicle. Studies have been conducted considering both hard and soft terrains in which equations of equilibrium are used to obtain a solution [10].

Analyzing the obstacle performance of tracked vehicles is a very complicated task and for this reason many of the studies found in literature present simplified models often neglecting affects such as: motion resistance, slip-sinkage, load transfer due to centrifugal forces and the interaction between the grousers of the track and the obstacle. Moreover, during off-road operation a tracked vehicle is most likely to encounter an obstacle surrounded by soft terrain unlike the assumptions made in previous studies where the terrain is assumed to be non-deformable. Because of these simplifications most of these studies do not yield realistic results and it is therefore imperative to expand the knowledge in this area to advance in the development of more robust designs for tracked vehicles.

Over the years, studies on tracked vehicle dynamics have predominantly been performed with respect to large and heavy vehicles (over 2000 lbs.), usually for military and agricultural means. In recent years, however, the employment of small robotic tracked vehicles has gained considerable interest in the use of off-road applications such as: reconnaissance, exploration, mining and safe-and-rescue missions. Developing mathematical models that provide metrics describing the mobility performance of small robotic tracked vehicles are highly desirable because they would facilitate the design of control and path planning algorithms used to maneuver these vehicles through various terrains.

Since most works dealing with the analysis of tracked vehicles have been focused towards large vehicles, it is uncertain whether the equations and relationships provided by these studies are applicable to small robotic vehicles. For example, many of the accepted relationships used in the analysis of tracked vehicles are based

on semi-empirical formulas, in which experimental tests were conducted specifically for large tracked vehicles in order to obtain certain unknown parameters. However, there are uncertainties associated with these parameters that lead to errors in simulation results. Because the dynamics associated with heavy tracked vehicles are at a large scale, the sensitivity of simulation errors may be within an allowable range. This may not be the case for small tracked vehicles where the dynamics are at a significantly smaller scale. The simulation errors may be very sensitive to the uncertainties associated with unknown parameters. If this is the case, then new relationships will have to be developed in order to describe the dynamics at the track-terrain interface for small tracked vehicles.

This thesis represents research dedicated to developing models that can be used for predicting the mobility performance of small robotic tracked vehicles. The results would allow virtual test simulations to determine whether a given robotic tracked vehicle will successfully maneuver over a given terrain. The benefits of using modern simulation technology will aid in comparing different tracked vehicle designs in an efficient manner so as to support for a successful tracked vehicle mission.

Preliminary work has been conducted, in which the obstacle performance of a particular robotic tracked vehicle was analyzed both analytically and experimentally [11]. The aim of the study was to investigate ways of developing, verifying, and validating mobility models for the three idealized obstacle geometries: steps, ditches and slopes. The purpose of the present work is to build and verify a dynamic model for predicting the mobility performance of a particular robotic tracked vehicle operating over flat two-dimensional terrain.

1.2 Previous Works

As previously mentioned, various researchers have presented models designed for analyzing the different behaviors of tracked vehicles traveling over level ground.

Most of these studies have been influenced by the works of Bekker [2, 6, 12], who is credited to be the first person to make extensive ground work in the field of tracked vehicle dynamics. Many of his proposed concepts and formulations on tracked vehicle mechanics have been widely accepted and are still used by researchers in this field. His works have been reviewed and revised by Wong [1, 13].

The different models presented in the literature vary in complexity from those that consider stationary (steady-state) motions over firm level ground to the more sophisticated models that consider non-stationary (transient) motions over soft level terrains. One of the first studies presented considering stationary motions on firm level ground was performed by [14]. Steeds discusses the kinematics of skid-steering and derives equations for steering forces, including the affects of longitudinal track resistance. In his analysis, he assumes that the shear stress developed under the track obeys the law of Coulomb friction. This implies that the shear stress on the track-ground interface reaches a maximum value instantly, as soon as a small relative movement between the track and ground takes place. He also presents a general case of steering dynamics where the effect of lateral friction is considered. However, Steeds' work utilizes a trial and error type solution for track forces, and he neglects the effects of centrifugal forces developed during turning maneuvers.

A more detailed model was presented by [15], in which they investigate the problems concerning steerability, stability and relevant behavior at high speeds. They develop equations for uniform turning motions based on the assumptions that the ground pressure are modeled as concentrated forces acting underneath each road wheel and the friction between the tracks and ground were Coulomb friction with the friction coefficients being constant and isotropic in the longitudinal and lateral directions. They also include the effects of load transfer due to the centrifugal force and track tension.

A few years later, [16] developed a more detailed model allowing for the

study of non-stationary motions in order to disclose the effects of initial forward velocities on the transients of the track slip velocity, side slip angle, yaw rate, and acceleration of the center of gravity of the vehicle. The authors modeled the shear stress as anisotropic Coulomb friction with the friction coefficients being described by a pull-slip equation.

One of the major issues in modeling the mobility performance of tracked vehicles is the characterization of the lateral forces developed under the tracks. As previously mentioned, the lateral forces are developed due to the relative motion between the tracks and ground, which in turn contribute to a moment of turning resistance. Many works modeled the lateral forces using a constant coefficient of friction, meaning the magnitude of the lateral forces are the same regardless of vehicle speed and turning radius. This view was argued by [17], in which he investigates the variation of the track forces with the turning radius of the vehicle. Kar argues that the lateral coefficient of friction is a function of the turning radius of the vehicle, explaining why the track forces decrease with an increasing turning radius. This argument was also supported by [1], in which he develops a general theory for skid-steering on firm ground that can be used to calculate the lateral coefficient of friction as a function of vehicle speed and turning radius.

Kitano's model along with two other less sophisticated models, were slightly modified and evaluated by [18]. Simulation results of these modified models were compared to experimental testing data. The work was aimed at finding out the best possible analytical model that could be used for simulations to investigate the turning resistance of tracked vehicles. Their results reveal that the modified Kitano model can be used to predict the turning radius of the vehicle with good accuracy. Thus, radius enlargement factors could be determined by means of the Kitano model, and thus utilized to improve the accuracy of the other two models, which had much faster computation times.

With increasing computer technology, advanced computer software packages allowing more sophisticated models to be built while still maintaining efficiency in simulation. The work by [4] presents a 3D dynamic model of an agricultural vehicle within a modeling and simulation environment based on Object-Oriented tools and techniques. One of the interesting contributions of this work is the derivation of a dynamic model for the shear displacement. The work by [19] utilizes a multi-body software package to build a very sophisticated dynamic model of a particular tracked vehicle. The model includes a detailed representation of the track system including individual track links and a suspension.

1.3 Problem Statement

This thesis describes the formulation and evaluation of a dynamic model for predicting the mobility of a particular robotic tracked vehicle operating on flat two-dimensional terrains. There are increasing demands to develop model-based studies for quantifying the performance metrics of small robotic tracked vehicles. The information extracted from these studies would be beneficial to the proper development of both the control and power systems of the vehicle, to the experimental evaluation of prototype systems, and to help maximize the predictability of successful missions. Since, the mobility of a vehicle is highly dependent on the way it engages the terrain, the focus of this thesis is on the development of a dynamic track-terrain interaction model.

A virtual representation of the vehicle is constructed in CAD software and then implemented into a multi-body dynamics program. The latter provides a software environment where all the forces due to the track-terrain interaction are modeled and the equations of motion are assembled and solved numerically. The formulation of the forces are adopted from the literature, and extensions are made to reduce the complexity of the system without losing significant accuracy. An objec-

tive of this work is to verify whether applying existing methods used for analyzing the mobility performance of large scale tracked vehicles suffice for evaluating small robotic tracked vehicles.

In order to validate the vehicle model, field tests are conducted subjecting the test vehicle to various maneuvers on different terrains. The vehicle model is then simulated to reproduce the field tests, in which the vehicle maneuvers can be specified by driver inputs conveyed as individual drive motor voltage signals. Comparisons are then made between the simulated results and those obtained from the field tests to evaluate the effectiveness of the vehicle model.

1.4 Thesis Contributions

The main contributions of this thesis are summarized as follows:

1. A new approach is presented for modeling the track-terrain interaction.
2. The model can be integrated into a multi-body dynamics software package allowing for visualization feedback.
3. A dynamic model capable of analyzing non-stationary maneuvers is evaluated, which includes a basic model of the power sources and drive-train.
4. Comparisons are made to experimental studies.

1.5 Thesis Outline

The thesis is divided into six chapters. **Chapter 1** presents the premise and background of the thesis, including its main contributions. The study of soil mechanics, based on the parametric approach, along with the fundamental concepts and formulations used to describe the track-terrain interaction are discussed in **Chapter 2**. In **Chapter 3** a detailed analysis is presented describing the development of

the track-terrain model, in which the construction of the various force models is explained. Further discussion is given about the process of implementing the model into a multi-dynamics software package. **Chapter 4** describes the modeling and testing of the power system used to drive the vehicle model. Also, descriptions of the field tests conducted with the test robotic tracked vehicle is given. **Chapter 5** discusses the comparison between the simulation results with results obtained from the field tests. **Chapter 6** presents the conclusions of the thesis along with recommendations for future work.

Chapter 2

Classical Mechanics of Track-Terrain Interaction

2.1 Introduction

The development of the tracked vehicle dates back to 1770, when Englishman Richard Lovell Edgeworth patented his “portable railway” idea. Many more patents followed during the 19th century, but because of the insufficient technology and lack of resources most of these designs failed to reach commercialization. It was during the early 1900’s that companies such as the Hornsby Company and the Holt Company began to make real progress in tracked vehicle technology by contributing to the improvement of the steering mechanism design and to the architecture of the tracks. Recognizing the capabilities of these vehicles to maneuver across rugged terrains and over various size trenches, lead to the first deployment of tanks on the battlefield during World War I. However, problems were still encountered with many of the tanks breaking down. Heavy artillery and engines with high power-to-weight ratios often caused the tanks to make craters too large and too deep to cross or climb out of. As a result, new fields for studying how a vehicle interacts with its

environment began to evolve, but because the mechanical adjustments of existing mechanisms to new requirements consumed much of the efforts no time was left for basic studies [2]. It wasn't until later on, particularly since World War II, that systematic studies of the principles underlying the rational development and design of off-road vehicles gained considerable interest [1]. The study of the performance of an off-road vehicle in relation to its operating environment (the terrain) has now become known as "terramechanics".

A central issue in terramechanics is to understand the mechanical properties of a given terrain and its response to vehicular loading in order to establish a quantitative relationship between the design and performance of an off-road vehicle. Since the late 1950's, numerous methods have been developed to predict the performance of off-road vehicles operating over unprepared terrain. These methods can be categorized into three groups: analytical methods, empirical methods and parametric methods. In reference to the analysis of tracked vehicles, a discussion of these methods will be given.

2.2 Methods for Predicting Track-Terrain Interaction

2.2.1 Analytical Methods

The theoretical methods are commonly based on the principles using the theory of plastic equilibrium and on techniques based on the finite element method (FEM). In the theory of plastic equilibrium, it is assumed that the terrain behaves like an ideal elastoplastic material. This means that when a load exerted on the terrain surface reaches a certain level, the terrain within a specific volume will approach a state of failure. An infinitely small increase in the load beyond this level will produce a rapid increase in strain, often referred to as plastic flow, while the stress remains relatively constant as shown in Figure 2.1. The state that precedes plastic flow,

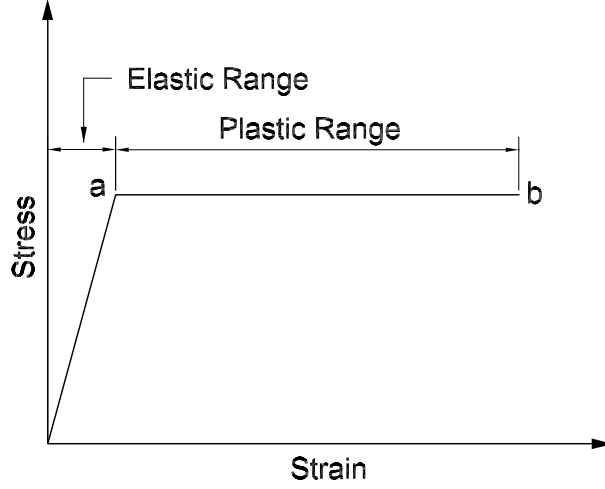


Figure 2.1: Stress-Strain Behavior of an Ideal Elastoplastic Material

point “a”, is usually referred to a plastic equilibrium. The transition from the state of plastic equilibrium to plastic flow constitutes the failure of the mass. One of the widely used criterion for determining the condition of shear failure by plastic flow is given by Mohr-Coulomb’s equation,

$$\tau_{max} = c + \sigma \tan \phi, \quad (2.1)$$

where τ_{max} is the maximum shear strength of the material, c is the apparent cohesion of the material, σ is the normal stress on the sheared surface and ϕ is the angle of internal shearing resistance of the material. A more detailed description of these parameters will be given in Section 2.3.2.

A particular application using the theory of plastic equilibrium is in the prediction of the maximum load that a tracked vehicle can be supported by on a particular soil without causing failure. When the load of the vehicle on the ground is light, the soil will be in a state of elastic equilibrium. However, once the load increases beyond a certain threshold, the soil beneath the track will enter into a state

of plastic flow causing the track to sink abruptly. This information is useful because the external resistive forces hindering the motion of the vehicle are highly dependent on the sinkage (Section 2.4.2). Therefore, using the theory of plastic equilibrium we can estimate whether the resistive forces will be significant by knowing if the soil beneath the track is in a state of plastic flow.

Although the theory of plastic equilibrium provides some insight in the evaluation and prediction of tracked vehicles in off-road applications, there are many limitations. The theory of plastic equilibrium is based on the assumption that the terrain behaves like a perfectly plastic material. Even though some soils exhibit this behavior, such as dense sand, many other terrains like snow and organic terrain have a high degree of compressibility. This implies that failure zones in these terrains under the load of the vehicle may not develop in a manner similar to that assumed in the theory of plastic equilibrium, and the sinkage of the vehicle running gear is primarily due to compression and not to plastic flow of the soil. Moreover, the theory of plastic equilibrium is mainly concerned with the prediction of the maximum load that causes failure of the soil mass, but does not deal with the deformation (such as sinkage and slip) of the terrain under load, which is often required in analyzing the off-road operation of tracked vehicles. For these reasons, in practical applications only very approximate assumptions may be made using the theory of plastic equilibrium in order to evaluate the response of soils subject to vehicular-loading [6].

In recent years, researchers have applied the finite element method to model the track-terrain interaction. In this method, the terrain is represented by a system of elements with specified constitutive relationships interconnected at nodes to form a mesh. Figure 2.2 shows a mesh of triangular elements, which are commonly used, developed for the analysis of terrain deformation under a track system. In this particular case, only half of the problem domain is modeled due to symmetry.

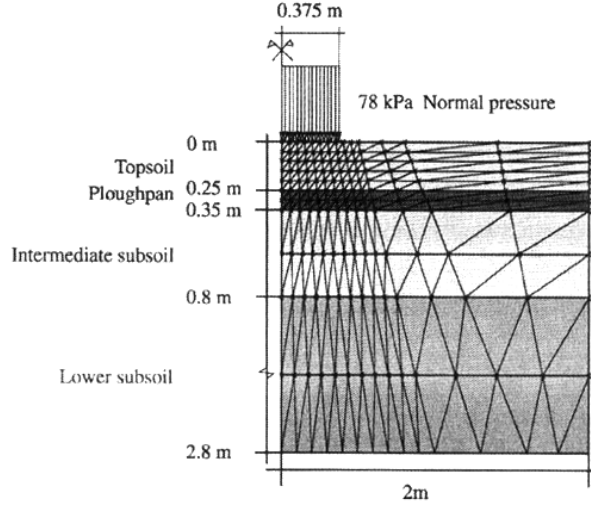


Figure 2.2: Finite Element Mesh, from [20]

Using the finite element method, there are generally two types of studies performed in relation to track-soil mechanics: the response to the terrain to vehicular loading and the prediction of the track performance. In the first case, the inputs to the system are the normal and shear stress distributions at the contact patch along with the load-unload stress-strain relations of the terrain. The output to the simulations are the stress, strain rate and the velocity fields within the terrain. In the second case the track-soil interaction is calculated using constitutive relations to describe the mechanical behavior of the soil in terms of critical state soil mechanics.

There are some limitations in the application of the finite element method to soil mechanics. For example, the finite element method requires known constitutive relationships of the terrain input such as: modulus of elasticity, Poisson's ratio and many other mechanical properties of the terrain that are usually difficult to define. Moreover, to simplify the analysis the stress-strain relationship and the strain hardening property of the soil are commonly assumed to be similar to those of metals, which cannot be rationalized with empirical evidence. The finite element

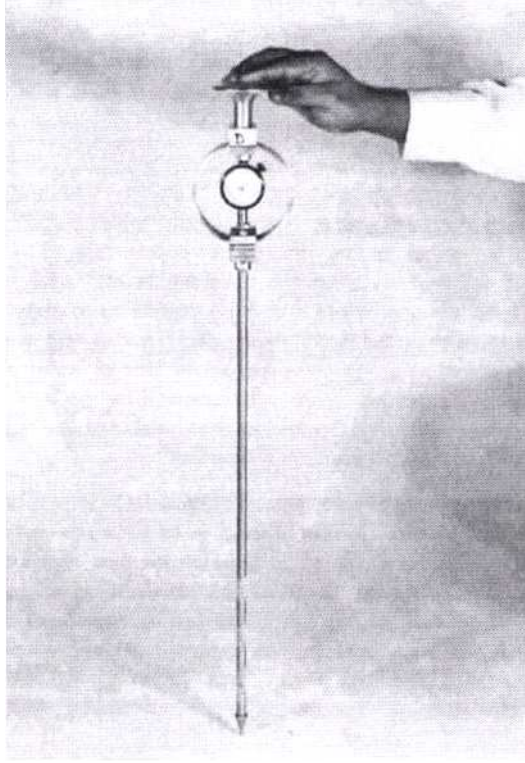


Figure 2.3: The Basic Components of a Cone Penetrometer, from [21]

method can also be very computationally expensive.

2.2.2 Empirical Methods

The development of empirical methods originated during World War II by the U.S. Army Waterway Experiment Station (WES) to provide military intelligence and reconnaissance personnel with a simple means for assessing vehicle mobility on a "go or no go" basis on various soils [1]. The general approach to these methods is to conduct experimental tests on a select group of vehicles over a range of terrains of interest. Based on the measured data, the terrain is characterized and identified. With the results of the vehicle performance testing and the terrain characteristics identified, the two sets of data are then empirically correlated.

The terrain characteristics are identified by a parameter known as the cone index (CI), which is obtained using a cone penetrometer as seen in Figure 2.3. The penetrometer consists of a 30° circular cone with a 0.5 in.^2 base area, a proving

ring and a gauge dial for indicating the force required to push the cone into a given soil. The CI is the force indicated by the gauge dial divided by the area of the cone base. Therefore, the CI has a unit of pressure, but it is commonly used as a non-dimensional parameter. With this information along with use of other empirical indices the values of the performance parameters of a tracked vehicle, such as the net maximum drawbar pull coefficient (the ratio of drawbar pull to vehicle weight), maximum slope negotiable and the towed motion resistance coefficient can then be empirically determined as functions of the vehicle type, number of passes to be completed or the IC.

Empirical methods are easy to implement and they provide useful information in estimating the performance of vehicles with design features similar to those that have been tested under similar operating conditions. However, these methods cannot be extrapolated beyond the conditions upon which they were derived; meaning, it is uncertain whether these methods can be utilized in evaluating new vehicle design concepts or the predicting the vehicle performance in new operating environments. Moreover, if a large number of parameters are required to define the problem, then an empirical approach may not necessarily be cost-effective.

2.2.3 Parametric Methods

Parametric methods for analyzing the performance of tracked vehicles are based on both the measurement of the terrain response under loading conditions similar to those exerted by a tracked vehicle and on a detailed analysis of the mechanics of the track-terrain interaction. Experimental tests are conducted measuring various relationships to characterize the response of the terrain when subject to different normal and shearing loads, in which equations with unknown parameters are then postulated to fit the measured data. In order to rationally determine the unknown parameters, statistical techniques, such as the least squares method, are

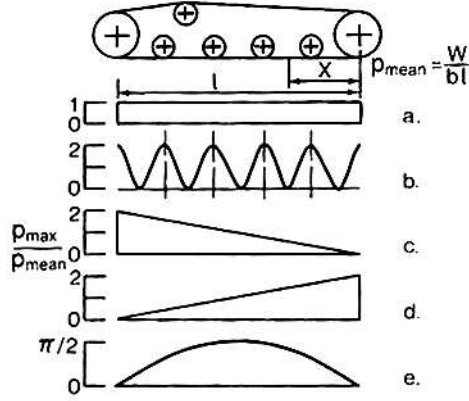


Figure 2.4: Various Ideal Normal Pressure Distributions Underneath a Track, from [22]

often adopted so that the residuals between the measured values and those predicted by the proposed equation are minimized. Two key relationships often required by parametric methods are the pressure-sinkage and the shear stress-shear displacement relationships, which are used in modeling the mechanics of the track-terrain interface and will be discussed in subsequent sections.

In analyzing the mechanics of the track-terrain interaction, it is assumed that the track in contact with the terrain is similar to a rigid footing, meaning it does not conform to the contour of the terrain. If the center of gravity of the vehicle is located at the mid-point of the track contact area, then the normal pressure distribution is assumed to be uniform. If the location, however, of the center of gravity is located away from the mid-point, then other profiles are assumed as shown in Figure 2.4. With this information, along with the pressure-sinkage and the shear stress-shear displacement relationships, the dynamics of the track-terrain interaction such as: motion resistance due to the compacting of the terrain, tractive effort and the moment of turning resistance can be modeled in order to predict the mobility performance of the tracked vehicle.

There are limitations to these methods in that the idealization of the track

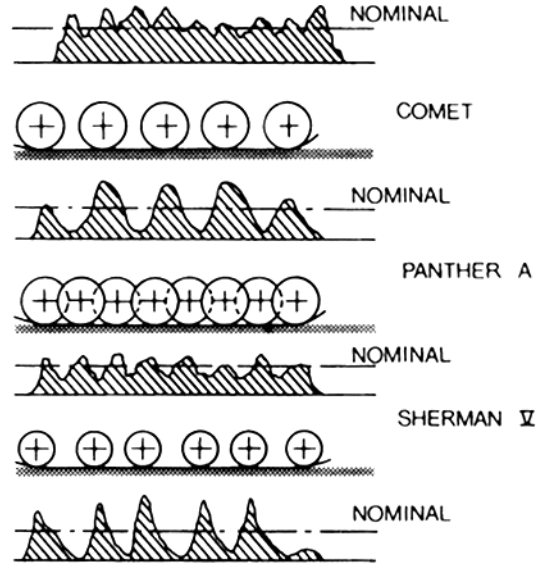


Figure 2.5: Measured Normal Pressure Distributions Below the Surface Under Various Tracked Vehicles, from [2]

being modeled as a rigid footing is not realistic for tracked vehicles having high ratios of roadwheel spacing to track pitch. In these cases, the track deflection can be significant on soft terrains causing the ground pressure to be concentrated under the roadwheels and to be far from uniform. On soft terrains, the actual length of the track in contact with the ground increases causing both a reduction of the sag of the top run of the track and an increase in track tension. This change in track tension greatly influences factors such as the normal pressure distribution and the thrust developed by the tracks. Consequently, using parametric methods to model the dynamical interaction at the track-terrain interaction of such track configurations would yield unrealistic performance predictions on soft terrain.

Fortunately, however, the particular tracked vehicle used in this study uses many small road wheels spaced closely together, which prevents its track from deforming on soft terrains. Therefore, for this particular vehicle it is reasonable to

model its tracks as rigid footings. Moreover, because the analytical and empirical methods each have a major drawback in the requirement of extensive computational power and cost-effectiveness respectively, the methods of parametric analysis will be used to model the track-terrain interaction. The particular methods to be adopted are based on the techniques developed by Bekker [2, 6, 12] and Wong [1]. The measurements and characterizations of terrain response are discussed in the next sections, which are based on a technique developed by Bekker known as the bevameter technique. The mechanics of track-terrain interaction and methods for the parametric analysis of off-road vehicle performance will be discussed in subsequent sections.

2.3 Measurement and Characterization of Terrain Response Using the Bevameter Technique

The forces developed at the track-terrain interface are highly dependent upon the properties of the terrain and its response to vehicular loading. During operation, a tracked vehicle subjects the terrain to normal loads due to the weight and any inertial load transfer by the vehicle, which results in sinkage and giving rise to external resistive forces. Also, when a torque is applied to the sprocket, a shearing action is developed between the track and the terrain, which results in slip giving rise to thrust. Therefore, experimental data is needed that can be used to characterize the deformation and compressibility (bearing capacity) of the terrain and the reaction of the soil particles (shear strength) when subject to various normal and shearing loads respectively.

A well known technique to measure and characterize the terrain response was proposed and developed by Bekker known as the bevameter technique, which is composed of two sets of tests where one is a set of plate penetration tests and

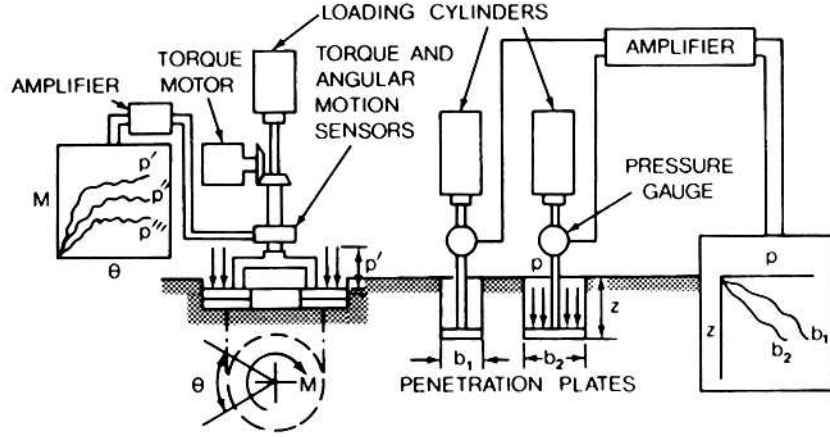


Figure 2.6: Schematic View of a Bevameter for Measuring Terrain Properties, from [6]

the other is a set of shear tests. In the plate penetration test, a hydraulic ram is usually used to apply a normal load to a plate of suitable size in order to simulate the contact area of the vehicle running gear. The applied pressure and the sinkage of the plate are measured to obtain the pressure-sinkage relationship. In the shear test, a shear ring or a shear plate is used apply a shear loading on the terrain surface under various normal pressures. For a given pressure, the torque applied to the shear ring is recorded along with the angular displacement of the shear ring to obtain both the shear stress-shear displacement relationship and the shear strength properties of the terrain. A schematic view of a bevameter apparatus is shown in Figure 2.6.

2.3.1 Pressure-Sinkage Relationship

After the pressure-sinkage data has been collected and properly characterized, a different mathematical expression is proposed depending on the type, structure and conditions of the terrain. According to Bekker [2], if the soil is considered to be

homogenous within the depth of interest then it may be characterized by:

$$p = \left(\frac{k_c}{b} + k_\phi \right) z^n \quad (2.2)$$

where p is pressure, b is the smaller dimension of the contact patch, z is the sinkage and n, k_c and k_ϕ are the pressure sinkage parameters known as the exponent of terrain deformation, cohesive modulus of terrain deformation and frictional modulus of terrain deformation, respectively. The pressure-sinkage was previously proposed by [23] as $p = kz^n$; however the k -value was found to be very sensitive to the radius of the test plate. Therefore, Bekker introduced the soil parameters k_c and k_ϕ . The parameter k_c is mainly dependent on the soil cohesion c , which is affected by the soil clay content and moisture. The parameter k_ϕ is related to the friction angle of the soil ϕ and depends on the compaction degree (bulk density), particle diameter distribution and form, and to some degree on the moisture content of the soil.

In order to obtain the unknown parameters n, k_c and k_ϕ , Wong [13] developed a weighted least squares method using a data processing procedure that is computerized and incorporated into the automatic data processing unit. It has been shown that the parameters n, k_c and k_ϕ are insensitive to using rectangular plates with high aspect ratios (greater than 5-7) or using circular plates having radii equal to the widths of the rectangular plates. Equation 2.2 is essentially an empirical equation and the parameters k_c and k_ϕ have dimensions that vary depending on the value of n .

An alternative equation based on a more fundamental nature in soil mechanics and by experimental evidence was proposed by Reece [24], in which he proposed the following pressure-sinkage relationship:

$$p = (ck'_c + \gamma_s bk'_\phi) \left(\frac{z}{b} \right)^n \quad (2.3)$$

where n , k'_c and k'_ϕ are the pressure-sinkage parameters, γ_s is the weight density of the terrain and c is the cohesion. In this equation, the parameters k'_c and k'_ϕ are dimensionless. There are some interesting properties about equation 2.3 that allow it to capture certain trends observed from pressure-sinkage tests. Experimental evidence has shown that for frictionless clay soils the pressure, when plotted against z/b , is practically the same regardless of the width of plate used. This should imply that k'_ϕ is negligible making equation 2.3 consistent with experimental observations. Experimental tests have also shown that the pressure increases linearly with the width of the plate for a given value z/b for clay cohesionless sand. Therefore, this would imply that k'_c is negligible, making equation 2.3 consistent with the observed data.

Although equation 2.3 differs from equation 2.2 in the effect of the plate width, Reece argued that this was sufficient to make a radical improvement. Unfortunately, the additional parameters that must be estimated in equation 2.3 complicate the track-soil model, and experimental data that provides values for these pressure-sinkage parameters are scarce.

There are two other types of terrain often encountered in off-road applications that have distinct pressure-sinkage properties, thus requiring different equations to characterize their behavior. For organic terrain (muskeg), which consists of a mat of living vegetation on the surface with a layer of saturated peat beneath it, Wong proposed the following pressure-sinkage relationship,

$$p = k_p z + 4m_m z^2 / D_h, \quad (2.4)$$

where p is the pressure, z is the sinkage, k_p is a stiffness parameter for the peat, m_m is a strength parameter for the surface mat and D_h is the hydraulic diameter of the contact area or sinkage plate, which is equal to $4A/L$, where A and L are the area and the perimeter of the contact patch, respectively. The other terrain often

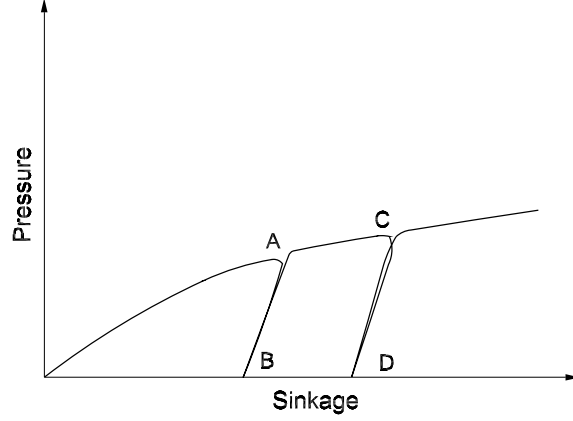


Figure 2.7: Response of a Sandy Soil to Repetitive Normal Loading

encountered is snow covers with ice layers, in which Wong proposed the following pressure-sinkage relationship,

$$p = p_{\omega}[1 - \exp(-p/p_{\omega})], \quad (2.5)$$

where again p is the pressure, z is the sinkage, z_{ω} defines the asymptote of the pressure-sinkage curve and p_{ω} is an empirical parameter.

Typically, the soil is under repetitive loading by the running gear when the vehicle is traveling along a straight line, in which the portion of terrain under the running gear is first subject to the load applied by the leading road wheel of the track system. After the leading wheel has passed, the load on the terrain is reduced, in which the process is repeated until the last road wheel has passed. Figure 2.7 shows the response of a sandy terrain subject to repetitive loading. The pressure initially increases along the curve OA . When the load applied to the terrain is reduced at A , the pressure-sinkage relationship follows the along the curve AB . When the force is reapplied at B , the pressure-sinkage relationship nearly follows the same path as that during unloading. Similar, but slightly different, behaviors occur on both

organic and snow terrains. In order to characterize this behavior, Wong proposed the following equation that represents the average response of the terrain:

$$p = p_u - k_u(z_u - z) \quad (2.6)$$

where p and z are the pressure and sinkage during unloading and reloading, p_u and z_u are the pressure and sinkage, respectively, when unloading begins and k_u is the pressure-sinkage parameter representing the average slope of the unloading-reloading line at AB . The value of the parameter k_u is a function of the sinkage z_u which may be expressed by

$$k_u = k_0 + A_u z_u \quad (2.7)$$

where k_0 and A_u are parameters characterizing the response of the terrain to repetitive loading. The value of k_u represents the slope of the unloading-reloading line AB , in which if the line AB is vertical then there is no elastic rebound and the deformation of the terrain is entirely plastic.

2.3.2 Shear Stress-Shear Displacement Relationship

The tractive effort initiated onto the vehicle is caused by the sliding action of the tracks relative to the ground, which generate shearing forces at the track-terrain interface. This shearing phenomenon can be characterized by the shear stress-shear displacement relationship obtained from data using the bevameter technique. Similar to the pressure-sinkage relationship, a different mathematical expression is used to predict the shear stress-shear displacement relationship depending on the structure and state of the terrain. From experimental data, it is found that there are typically three types of shear stress-shear displacement relationships observed.

For loose sand, saturated clay, dry fresh snow and most other distributed soils, the shear stress-shear displacement relationship has a profile, in which the

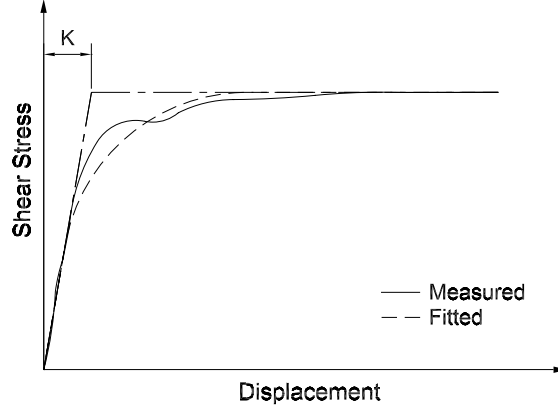


Figure 2.8: Shear Stress vs. Shear Displacement Relationship for Plastic Soils

stress initially increases rapidly with increasing shear displacement and then approaches a constant value with a further increase in shear displacement as shown in Figure 2.8. To describe this trend, Junosi and Humumoto proposed the equation,

$$\tau = (c + \sigma \tan \phi)(1 - e^{-j/K}), \quad (2.8)$$

where τ is the shear stress, j is the shear displacement, c and ϕ are the cohesion and angle of internal shearing resistance, respectively and K is the shear deformation modulus.

The soil is made up of aggregations of granular mass that may exhibit cohesive and frictional properties. Cohesion c refers to the strength gained from the ionic bond between grain particles irrespective of the pressure exerted by one particle upon another and is predominately in clayey (cohesive) soils. The angle of friction ϕ refers to the strength gained from internal frictional resistance highly dependent on the pressure exerted between the soil particles and is predominately in granular (cohesionless) soils. Therefore, the shear strength of clay or plastic snow, for example, does not theoretically depend upon the applied load, whereas that of a

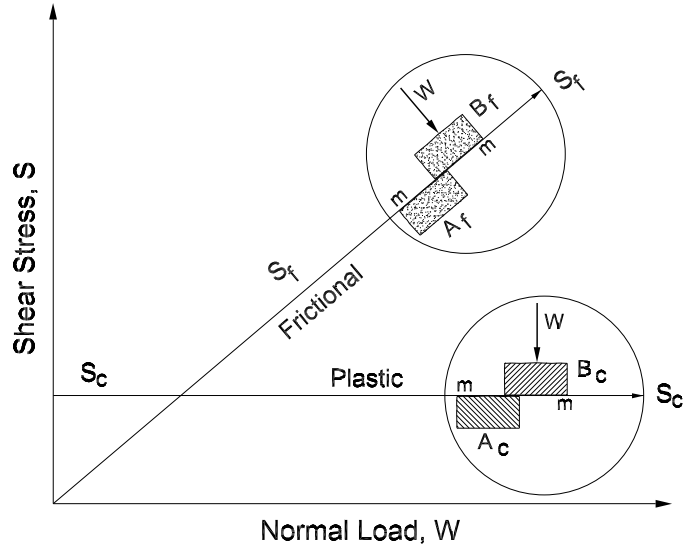


Figure 2.9: Shear Strength of Ideal Cohesive and Noncohesive Soils, modified from [2]

dry sand increases linearly with the increasing load as shown in Figure 2.9. Recall, the shear strength of a soil is given by the Mohr-Coulomb equation 2.1,

$$\tau = (c + \sigma \tan \phi),$$

which implies that for an ideal plastic clay soil, the angle ϕ vanishes so that,

$$\tau = c, \tag{2.9}$$

and for dry sand, the cohesion term c vanishes so that,

$$\tau = \sigma \tan \phi. \tag{2.10}$$

However, granular masses that cover most of the trafficable earth are usually composed of both cohesive and frictional properties .

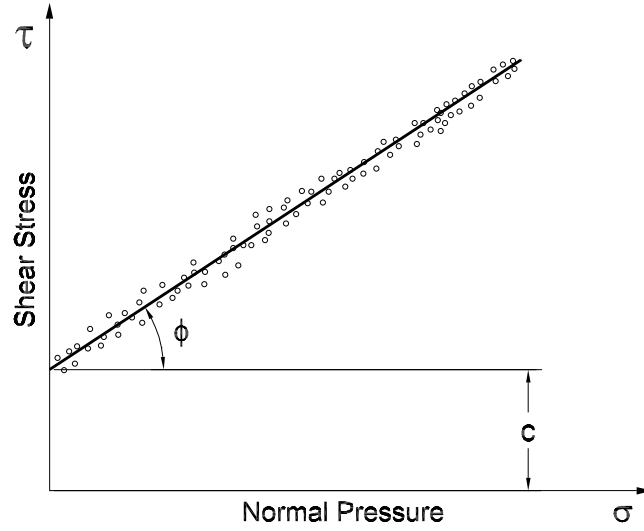


Figure 2.10: Shear Strength Relationship of Common Soils

If the maximum shear strength of the stress of a given terrain is plotted against the corresponding normal pressure, a straight line will be obtained as shown in Figure 2.10. The slope of the straight line determines the value of the angle of internal shearing resistance, ϕ and the intercept of the line where it crosses the shear stress axis defines the cohesion c of the soil. The value of K in equation 2.8 represents the measure of the magnitude of the shear displacement required to develop the maximum shear stress, in which its value is determined using the weighted least square principle [13]. Thus, equation 2.8 implies that the maximum shear stress will be reached only after a certain amount a shear displacement has taken place. It is important to point out that the parameters c , ϕ and K are actually empirical coefficients rather than soil constants having any physical meaning. The principles discussed above are to promote a better understanding of the relationship between the soil and the loads applied to them by the vehicle.

For compact sand, silt and loam, and frozen snow, their shear stress-shear displacement relationship has a profile, in which the stress increases rapidly and

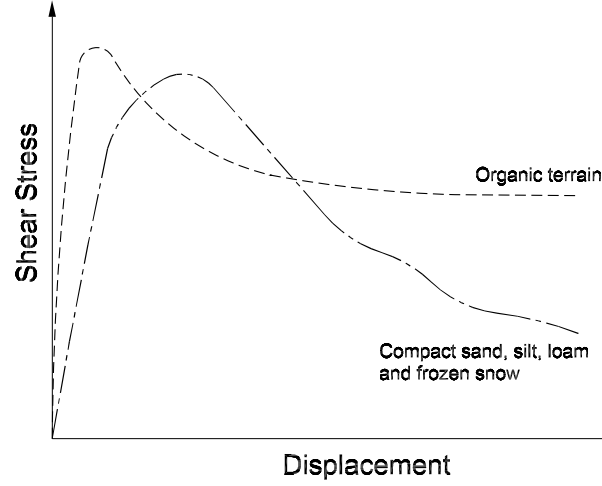


Figure 2.11: Shear Stress-Shear Displacement Relationship of Elastic and Organic Terrains

reaches a hump of maximum shear stress at a particular value of shear displacement. With a further increase in shear displacement, the shear stress decreases and reaches a relatively constant value as shown in 2.11. To characterize this behavior, Wong proposed the equation,

$$\tau = \tau_{max} K_r \{1 + [1/K_r(1 - 1/e)) - 1] \exp(1 - j/K_\omega)\} [1 - \exp(-j/K_\omega)], \quad (2.11)$$

where K_r is the ratio of the residual shear stress τ_r to the maximum shear stress τ_{max} , and K_ω is the shear displacement where the maximum shear stress occurs.

For organic terrain (muskeg), the shear stress-shear displacement relationship has characteristics in which the shear stress initially increases rapidly and reaches a hump at a particular value of shear displacement. With a further increase in shear displacement, the shear stress continually decreases as the peat beneath the mat offers a lower shearing resistance than the surface mat. This type of shearing

behavior may be characterized by and equation proposed by Wong,

$$\tau = \tau_{max}(j/K_{\omega}) \exp(1 - j/K_{\omega}), \quad (2.12)$$

where K_{ω} is the shear displacement where the maximum shear stress τ_{max} occurs.

During shear tests, an important phenomenon occurs as either the ring is being rotated or the shear plate is being moved horizontally, in which soil is being displaced away from the contact patch; thus, causing additional sinkage. Therefore, the total sinkage of the vehicle during off-road operation is composed of the static sinkage (previous section) and the sinkage due to the slip of the running gear relative to the terrain. This behavior is often referred to as the slip sinkage phenomenon. Because the motion resistance of the tracks is highly dependent of the sinkage of the vehicle, it is important to take this factor into account. Many attempts have been made to characterize this behavior; however, most proposed methods greatly complicate the original-empirical methods or require many additional tests. Therefore, a modified approach was proposed and developed by [25], where the soil values are obtained by applying normal and shearing loads simultaneously so that the total sinkage is taken into account.

2.4 Mechanics of Track-Terrain Interaction

2.4.1 Introduction

When torques are applied to the sprockets of a tracked vehicle on soft terrain, the tracks slide relative to the ground generating longitudinal shear forces or thrust. In order for the vehicle to move, the developed thrust must overcome the resistive forces arising from the sinkage of the vehicle. Utilizing the pressure-sinkage and shear stress-shear displacement relationships described in the pervious section, the resistive forces acting on the vehicle and the developed thrust can be predicted,

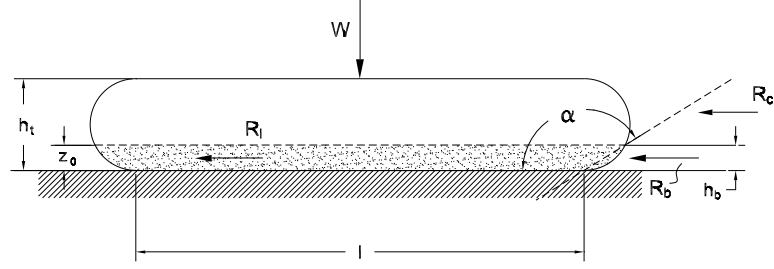


Figure 2.12: Resistive Forces Acting on a Tracked Vehicle Arising From Sinkage

respectively. The predictions are made using the method developed by Bekker, in which the track in contact with the terrain is assumed to be similar to a rigid footing.

2.4.2 Motion Resistance of the Track and the “Bulldozing” Effect

The deformation of the terrain initiated by the sinkage of the vehicle consumes a definite amount of energy, which is wasted in the form of external resistance to the motion of the vehicle. The external resistance is composed of three factors: motion resistance due to the compaction of the terrain, bulldozing resistance and soil drag. These resistive forces are illustrated in Figure 2.12.

The first form of external resistance arises due to the compaction of the terrain as a result of weight of the vehicle and any inertial load transfer. In the case of the track, it is reasonable to assume that there is only a vertical motion of the soil particles when compacted, since the track is comparable to a rigid plate. Using the pressure-sinkage relationship proposed by Bekker, the work done in compacting the terrain of a single track making a rut of track width b , track length l and depth

z_0 is given by,

$$\begin{aligned}
Work &= bl \int_0^{z_0} p \, dz \\
&= bl \int_0^{z_0} (k_c/b + k_\phi) z_n \, dz \\
&= bl \left(\frac{k_c}{b} + k_\phi \right) \left(\frac{z_0^{n+1}}{n+1} \right). \tag{2.13}
\end{aligned}$$

In computing the work done in compacting the terrain, an assumption has to be made about the pressure distribution profile underneath the bottom portion of the track (see Figure 2.4 for possible options). Assuming the pressure distribution to be uniform, then we can express z_0 in terms of the pressure p using the pressure-sinkage relationship as,

$$\begin{aligned}
z_0 &= \left(\frac{p}{k_c/b + k_\phi} \right)^{1/n} \\
&= \left(\frac{W/bl}{k_c/b + k_\phi} \right)^{1/n}. \tag{2.14}
\end{aligned}$$

Substituting this expression into equation 2.13 for z_0 and rearranging terms, the work done in compacting the terrain of a single track becomes,

$$Work = \frac{bl}{(n+1)(k_c/b + k_\phi)^{1/n}} \left(\frac{W}{bl} \right)^{(n+1)/n}. \tag{2.15}$$

The work done by the motion resistance R_c as the track is pulled a distance l can be equated to the work done in compacting the terrain making a rut of length l giving,

$$R_c l = \frac{bl}{(n+1)(k_c/b + k_\phi)^{1/n}} \left(\frac{W}{bl} \right)^{(n+1)/n}.$$

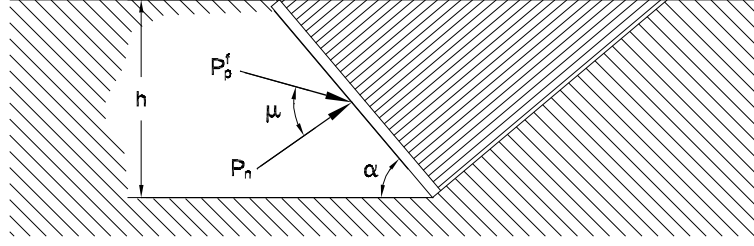


Figure 2.13: Computing the Bulldozing Resistance Using Principles Based on Earth Pressure Theory

Hence the motion resistance for a single track may be expressed by,

$$\begin{aligned}
 R_c &= \frac{bl}{(n+1)(k_c/b + k_\phi)^{1/n}} \left(\frac{W}{bl} \right)^{(n+1)/n} \\
 &= \frac{b^n}{(n+1)(k_c/b + k_\phi)^{1/n}} \left(\frac{W}{l} \right)^{(n+1)/n}.
 \end{aligned} \tag{2.16}$$

The second component of the external resistance of the vehicle is due to the bulldozing effect. When the ratio between the sinkage z_0 and the height of the tracked gear h_t becomes relatively large, there is drag caused by the bulldozing effect of the frontal portion of the track submerged in the soil to depth h_b , usually equal to the sinkage z_0 . Using principles based on earth pressure theory, it is assumed that the value of the bulldozing force R_b is equal to the horizontal projection of the passive earth pressure P_p^f . It is further assumed that there is no surcharge ($q = 0$) and that the angle of friction μ is equal to the angle of internal shearing resistance ϕ . Thus, the total bulldozing force for one track is given by,

$$R_b = \frac{2b \sin(\alpha + \phi)}{\sin \alpha \cos \phi} (2z_0 c K_c + \gamma z_0^2 K_\gamma), \tag{2.17}$$

where K_c and K_γ are dimensionless coefficients that depend, respectively, only on the cohesion c and the soil density γ .

The third contribution to the longitudinal external resistance is due to the drag of the adhering soil mass that penetrates above the track-soil interface and is pulled along the track and suspension of the vehicle. This shearing resistance between the moving and stationary parts of the soil acts over an area A' and is significant in cohesive soils, especially in dense muds. According to Bekker [2], this drag may be estimated as,

$$R_t = k_r z_0 l c \quad (2.18)$$

for a single track, where k_r may vary from 2 to 4, depending on the width of the belly.

2.4.3 Tractive Effort Developed by the Track

The tractive effort of a track is developed by its sliding action relative to the ground, which is often referred to as slip. In tracked vehicle performance evaluation, it is often desirable to determine the variation of thrust with the track slip over a full operating range. Recall in Section 2.3.2, the shear stress developed under a test plate is a function of shear displacement, which will be shown to be closely related to slip. Therefore, to predict the relationship between thrust and slip, it is necessary to determine the variation of shear displacement along the bottom portion of the track.

The shear displacement at various points along the track is shown schematically in Figure 2.14. At point 1, the grouser is just coming into contact with the terrain, meaning no shear displacement has taken place. However, the grouser at point 2 has been in contact with the terrain for some time t_2 , in which shear displacement has occurred due to the shearing of the terrain. The grousers at points 3, 4 and 5 have increasingly been in contact with the terrain implying that the shear displacement j increases along the track with the maximum value occurring at the rear of the contact area. Because the track cannot stretch, every point of the track

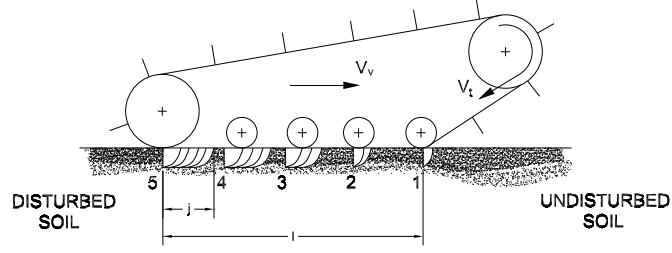


Figure 2.14: Development of Shear Displacement Underneath a Track, modified from [2]

in contact with the terrain has the same velocity relative to the ground given by

$$\begin{aligned} V_s &= R_s \omega_s - V_v \\ &= V_t - V_v, \end{aligned} \quad (2.19)$$

where V_s is referred to as the slip velocity, V_t is the tangential velocity of the track given by the product of the sprocket radius R_s and the angular velocity of the sprocket ω_s and V_v is the absolute longitudinal velocity of the vehicle. When the vehicle is driving $|V_t| > |V_v|$ the slip velocity V_s is in the opposite direction of the vehicle velocity V_v . On the other hand, when the vehicle is skidding (braking) $|V_t| < |V_v|$ the velocity V_s is in the same direction of V_v .

If an arbitrary point p is fixed to the belt of the track and is at a distance x from the front of the contact patch (see Figure 2.15), then the shear displacement at p is determined by integrating its velocity relative to the terrain V_s with respect to the amount of time it has been in contact with the terrain. Therefore, the shear displacement at the point p is determined by

$$\begin{aligned} j &= \int_0^{t^*} V_s dt \\ &= (V_t - V_v)t^*, \end{aligned} \quad (2.20)$$

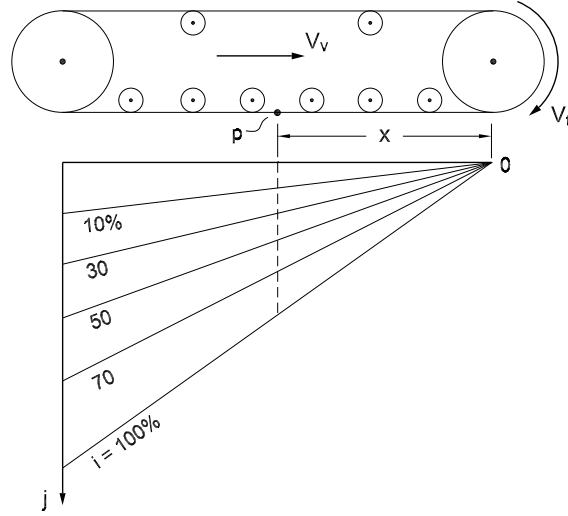


Figure 2.15: Shear Displacement Distribution Under Steady-State Conditions

where t^* is the amount of time the point p is in contact with the terrain. However, the time that the point p is in contact with the terrain is given by the distance it has traveled relative to the track x divided by its relative velocity to the track V_t so that,

$$t^* = \left(\frac{1}{V_t} \right) x. \quad (2.21)$$

Inserting this result into equation 2.20 the shear displacement at the point p is given by,

$$j = \left(\frac{V_t - V_v}{V_t} \right) x. \quad (2.22)$$

Since the location of the point p was arbitrarily chosen, equation 2.22 represents the shear displacement profile along the length of the bottom portion of the track. The term in parenthesis in equation 2.22 is referred to as slip i so that equation 2.22 can be rewritten as,

$$j = ix. \quad (2.23)$$

This result gives the relationship between the shear displacement and the slip of

the track. Notice that the shear displacement increases linearly with the distance x along track. Figure 2.15 shows the shear displacement profiles for different slip i values. It must be mentioned that the procedure presented to arrive at equation 2.23 only applies to steady-state conditions.

Now that the shear displacement profile under the track has been determined, the shear stress distribution may be obtained using the shear stress-shear displacement relationship given by one of the equations from Section 2.2.3. If equation 2.8 is used to calculate the shear stress, then the tractive effort for a single track may be given by

$$\begin{aligned}
 F_t &= b \int_0^l \tau \, dx \\
 &= b \int_0^l (c + \sigma \tan \phi) \left(1 - e^{-j/K}\right) \, dx \\
 &= b \int_0^l (c + \sigma \tan \phi) \left(1 - e^{-ix/K}\right) \, dx.
 \end{aligned} \tag{2.24}$$

Depending on the normal pressure distribution underneath the track σ , the tractive effort for a single track may be determined. If the pressure underneath the track is assumed to be uniform ($p = W/lb$) then the tractive effort for a single track is,

$$\begin{aligned}
 F_t &= b \int_0^l \left(c + \frac{W}{bl} \tan \phi\right) \left(1 - e^{-ix/K}\right) \, dx \\
 &= (Ac + W \tan \phi) \left[1 - \frac{K}{il} \left(1 - e^{-il/K}\right)\right],
 \end{aligned} \tag{2.25}$$

where b , l are the width and length of bottom portion of the track in contact with the terrain and W is the normal load on the track. Equation 2.25 expresses the thrust developed by a single track in terms of the track slip i assuming a uniform normal pressure distribution.

Another important calculation in predicting the performance of a tracked vehicle is the drawbar pull, which is the force available for external work in a direction

parallel to the surface of the terrain over which the vehicle is moving. The drawbar pull is determined by

$$F_d = 2F_t - 2R_c - 2R_b - 2R_l \quad (2.26)$$

Because steady-state conditions are assumed, all the resistive forces are constant and the tractive effort is only a function of slip. Therefore, studies can be conducted to determine how the variation of slip affects the thrust and drawbar pull of the vehicle over various terrains.

2.5 Conclusion

This chapter has summarized the various methods used for predicting the performance of tracked vehicles over unprepared terrain. In particular, the method of parametric analysis was presented discussing the mechanics between the soil and the tracks of a tracked vehicle through key relationships that have a dominant effect on the developed forces at the track-terrain interface. In the next chapter, these relationships will be utilized and expanded for modeling the mechanics of the track-terrain interface to predict the motion of a tracked vehicle subject to non-stationary maneuvers.

Chapter 3

A Mathematical Model to Approximate Track-Terrain Interaction

3.1 Introduction

The goal of this work is to develop a dynamical model of a particular robotic tracked vehicle suitable for predicting its motion over various level terrains. This chapter presents the development of the vehicle model. In particular, the concepts of a new approach to modeling the track-terrain interaction is presented. Applying this new approach, a derivation is presented of the baseline equations used to model the dynamics at the track-terrain interface.

An advantage of this new model is that it can be implemented into a multi-body dynamics modeling and simulation environment. This greatly facilitates the modeling process, since multi-body dynamics software can generate and solve the equations of motion for complex systems numerically. What is often difficult or not incorporated in these modeling environments is a comprehensive way of dealing with

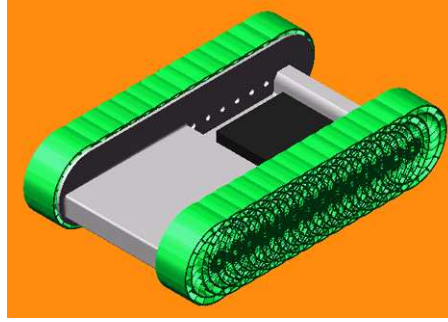


Figure 3.1: Solid Model of PackBot Integrated Into ADAMS Environment

many of the forces. An emphasis of this chapter is the implementation of the new track-terrain interaction model into a particular software environment. There are some modifications made to the baseline equations to prevent issues such as discontinuities from occurring. This introduces computational parameters into the model, which are discussed along with any limiting assumptions in the computational implementation.

At the end of the chapter, a summary is given of the assumptions made in developing the track-terrain model. Also given is a list of all the parameters required to simulate the track-terrain model, and the chapter concludes by comparing the new model presented in this chapter with one found in the literature.

3.2 Overview Of Vehicle Model

A solid model of the robotic tracked vehicle was created using the SolidWorks CAD software package. This model was imported into ADAMS, a multi-body modeling and simulation software environment. Figure 3.2 illustrates the general scheme used to model the vehicle in ADAMS. The lines with arrowheads on both ends are meant to represent physical interaction and power exchange. The main components of the model consist of the main body, tracks, dual motor and drive train systems, and the terrain. The inputs to the model are the motor voltages, which are supplied

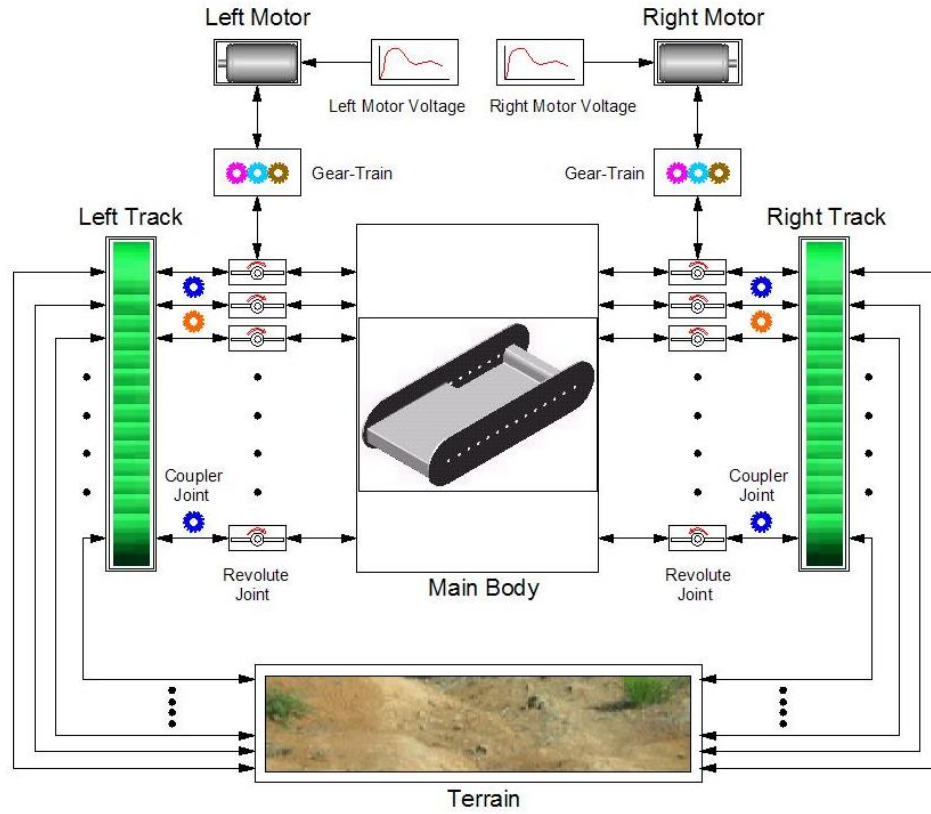


Figure 3.2: Model Scheme Implemented in ADAMS Environment

independently to each motor. The motor and drive train model is presented in the next chapter.

The left and right tracks are each replaced by a set of longitudinally cascaded and closely spaced wheels that are each connected to the main body via revolute joints. It is important to note that the wheels used in this track model do not function as wheels used on a traditional multi-wheeled vehicle. The use of the wheels in this track model serve three main purposes: 1) ADAMS assigns a reference frame to the center-of-mass of each wheel and it is these reference frames that are most important to the track-terrain interaction model. The frames are used to calculate both the longitudinal and lateral slip velocities at discrete points along the bottom portion of the track. The wheels' reference frames are also used to define the location of both the longitudinal and lateral shear forces and the ground normal force acting at discrete points along the track-terrain interface. 2) The inertias of the wheels are

required for ADAMS to calculate the rotational dynamics of the tracks. The total effective inertia of the motor, drive train, and track systems is distributed evenly to each wheel. 3) The configuration of the wheels visually resembles a track. Therefore, the wheels geometry is not used to interact with the terrain geometry as might be done in a conventional multi-wheeled vehicle model.

The sprocket of each track on this vehicle is coupled to a dc motor via a fixed gear drive train. In the model, each sprocket is represented by the first wheel, which is kinematically coupled to the remaining wheels in the track model using coupler joints. Consequently, when a torque is applied to the sprocket, all the wheels on the track model rotate at the same velocity. When the wheels contact with the terrain, shearing action is developed between the track model and the terrain. This creates shear forces that cause the motion of the vehicle.

ADAMS is a versatile modeling and simulation environment. It enables the designer to design, visualize, and evaluate improvements to a mechanical system at hand prior to building a physical prototype. ADAMS assembles and numerically solves the equations of motion for the mechanical system. This allows the designer to focus most of his/her attention on both defining how the system is coupled together and modeling the forces acting on the system. For this reason, the rest of the chapter focuses on the modeling the dynamics at the track-terrain interface.

3.3 The Discrete Approach to Modeling the Dynamics at the Track-Terrain Interface

This section discusses the concepts of a new approach to modeling the dynamics at the track-terrain interface. In this discussion, the expression “track model” will refer to the modeling of the track-terrain interaction.

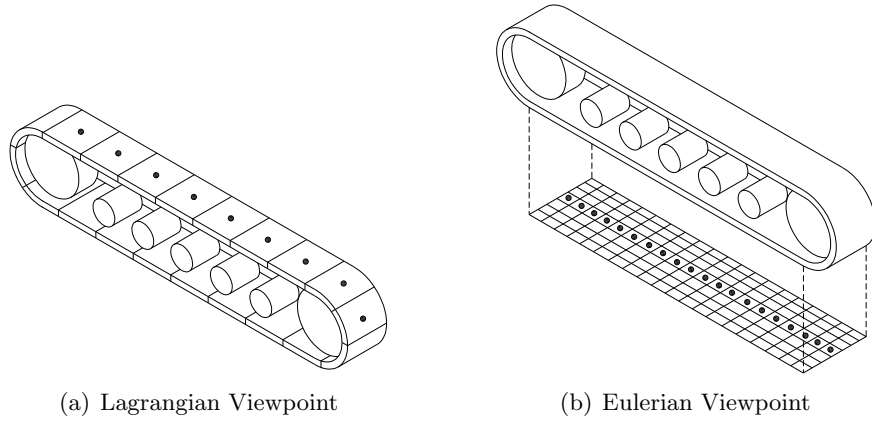


Figure 3.3: Different Approaches to Modeling Track-Terrain Interaction

3.3.1 Motivation

Various track models have been presented in the literature for analyzing the mobility performance of tracked vehicles operating over flat terrain. These models vary in complexity influenced by factors such as: size of tracks, type of terrain, average vehicle speed, and the use of a suspension system. Generally, however, these models adopt one of two different approaches for modeling the tracks of a tracked vehicle.

The first approach is analogous to a Lagrangian viewpoint (used in fluid mechanics), in which we focus attention on material particles as they move through the flow. In the case of modeling the tracks, focus is directed on the individual track links as they move around the track, as shown in Figure 3.3(a). The individual track links are modeled as rigid bodies and are usually coupled together using revolute joints [19]. Because such track models involve numerous bodies, they are usually modeled using computer-aided software.

The second approach used for modeling the tracks is analogous to an Eulerian viewpoint (often used in fluid mechanics), in which we focus attention on fixed points in space as time proceeds. In the Eulerian approach for modeling the tracks, focus

is made on points fixed along the track-terrain interface, as shown in Figure 3.3(b). These points are moving in space, but are fixed relative to the motion of the track. Since this approach focuses on points fixed to the track-terrain interface, modeling of the moving track links is typically not required.

There are some advantages and disadvantages in using either one of these approaches for modeling the tracks. In the Lagrangian approach, the individual track links are modeled. Constraints defining the coupling between the sprocket, idler, roadwheels, and track links must be set to ensure that the track remains in the sprocket-idler plane. This increases the number of dynamical equations that must be solved leading to higher computational costs. If our concern was with the design of the track, this viewpoint would be very desired. Track models based on the Eulerian approach involve less bodies to be modeled and are usually less complex, yet practical for motion analysis and control system design and are efficient from the computational point of view. The drawback is that details related to the track would not be accessible.

In the Lagrangian approach, the shear displacement of an individual track link is computed by integrating its slip velocity with respect to time. Integration is activated when the track link comes into contact with the terrain. The integration starts from the beginning with each new contact. In the Eulerian approach, calculating the shear displacement underneath the track is complicated by the need to solve a partial differential equation [4]. Either the partial differential equation must be solved or assumptions must be made to simplify the model.

In the Eulerian approach, the points fixed to the track-terrain interface are often modeled as infinitesimal elements. Integration is performed along the length of the track contact patch to compute the total shear forces developed at the track-terrain interface. This does not present a problem if only stationary (steady-state) motions are of interest, as in Chapter 2. However, if a dynamical model of a

tracked vehicle maneuvering over soft terrain is desired, integration along the contact patch can be difficult because the dynamics at the track-terrain interface are constantly changing. Moreover, integration along the track contact patch would have to be performed at each time step during the simulation, which could lead to high computational costs.

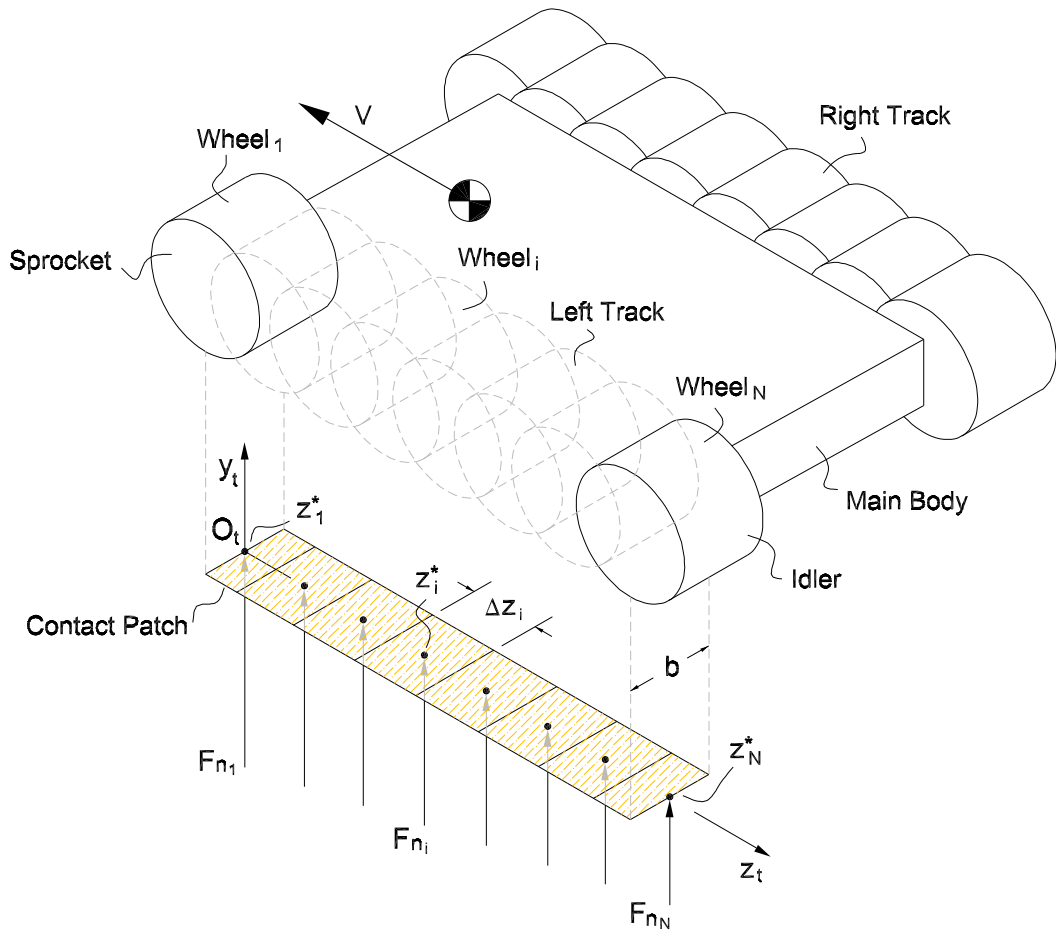
Motivated by these arguments, a track model was developed to satisfy the following requirements.

1. reduce the number of bodies to be modeled
2. can be easily implemented into a multi-body dynamics software environment
3. simple, yet practical for motion analysis over deformable terrain
4. computationally efficient
5. can easily be modified or extended in order to include, for example, the dynamics of motors, or other actuation sources.

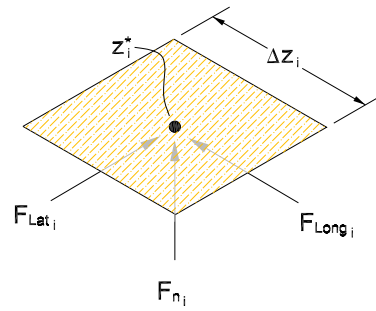
Based on these requirements, a new track model was developed adopting the Eulerian viewpoint and is referred to as the discrete approach.

3.3.2 Concept of Discrete Approach

The idea behind the discrete approach is to partition the contact patch between the track and the terrain into N discrete elements having an area of $b(\Delta z_i)$, where b is the width of the track and Δz_i is the length of the i^{th} discrete element as shown in Figure 3.4(a). Each element is assigned a point z_i^* that is referenced to a coordinate system (x_t, y_t, z_t) fixed to the track, where the value of z_i^* represents its fixed distance relative to the origin O_t of the track coordinate system. The purpose of the point z_i^* is similar to that taken in an Eulerian viewpoint used in fluid mechanics in which a fixed point in space, x_i , is of interest as time t proceeds. All of the flow properties



(a) Discretized Track-Terrain Interface



(b) Track-Terrain Interface Element

Figure 3.4: Illustration of Discrete Approach

(e.g. density, velocity and vorticity) are considered functions of x_i and t . The discrete approach uses the same concept, except the points of interest, z_i^* , are fixed to the track coordinate system that is moving in space.

The value of z_i^* is used to calculate the shear displacement at its location and once this has been calculated the shear stress at z_i^* can be determined using one of the shear stress-shear displacement relationships discussed in Chapter 2. Using the discrete area $b(\Delta z_i)$ of the element along with the calculated shear stress at z_i^* , the shearing force components acting at z_i^* can be approximated, taking the orientation shown in Figure 3.4(b). The normal pressure acting on the i^{th} element must be computed using a contact model to determine the normal force at the point z_i^* . Dividing this normal force by the area of the discrete element $b(\Delta z_i)$, gives the normal pressure acting on the i^{th} element. Using one of the pressure-sinkage relationships as discussed in Chapter 2, the motion resistance due to compacting of the terrain can be calculated.

The discrete approach makes use of a concept analogous to the problem of calculating the area under the curve $y = f(x)$ on the interval $[0, a]$ as shown in Figure 3.5. The actual area under the curve is found by integrating $f(x)$ and then using the Fundamental Theorem of Calculus. However, we can approximate the area under the curve by using a Riemann Sum, so that

$$Area = \int_0^a f(x) dx \approx \sum_{i=1}^N f(x_i^*) \Delta x_i. \quad (3.1)$$

The point z_i^* used in the discrete approach serves the purpose of the independent variable x_i^* used in the Riemann Sum. The function $f(x_i^*)$ is analogous to any dynamical variable $T(z_i^*, t)$ (e.g. shear displacement, shear force or normal force) of interest evaluated at the point z_i^* . Finally, the area of the i^{th} element ΔA_i used in the discrete approach is analogous to the discrete length Δx_i used in the Riemann Sum. Therefore, if $T(z_i^*, t)$ represents the longitudinal shear stress acting on the i^{th}

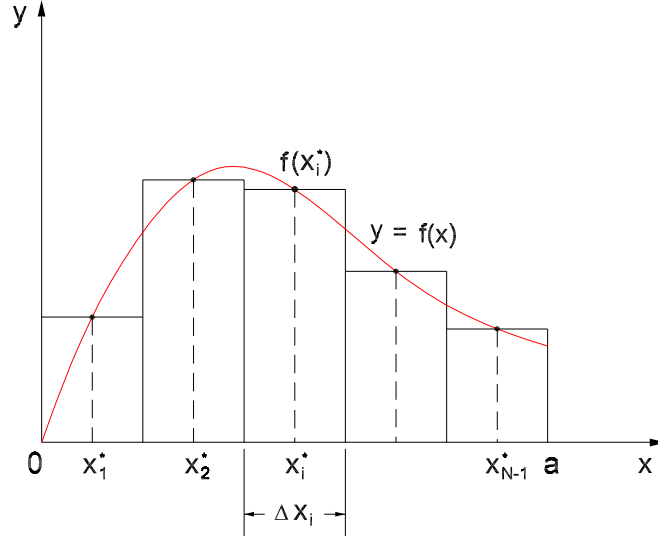


Figure 3.5: Approximating the Area Under a Curve Using a Riemann Sum

element at time t the total longitudinal force developed by the track is,

$$T_{total} = \sum_{i=1}^N T(z_i^*, t) \Delta A_i. \quad (3.2)$$

An advantage of the discrete approach is that it can easily be integrated into a dynamic system model for the vehicle (e.g. a system simulation environment or multi-body modeling environment like ADAMS or DADS). For example, using a multi-body system (MBS) modeling environment like ADAMS has many benefits and can save the designer valuable time. Because ADAMS generates and solves the equations of motion numerically, the designer can focus his/her attention on implementing the discrete approach to model the forces acting at the track-terrain interface. In ADAMS, a force is defined by both specifying the body it acts on and its orientation. The characteristics of the force are then defined by using ADAMS code. The constitutive laws used to model the force must be specified by the designer, and may need to be changed in case new data becomes available allowing for a more

accurate force model or if conditions change significantly. The next section discusses the modeling of the track-terrain interface using the discrete concept, and a specific implementation of the model using ADAMS is described. The forces are modeled using Bekker and Janosi correlations discussed in Chapter 2.

3.4 Modeling of the Dynamics at the Track-Terrain Interface Using the Discrete Concept

This section gives a derivation, based on the discrete approach, of the baseline equations used to model the track-terrain interaction. After each baseline equation is presented, a discussion is given of how it is implemented into ADAMS. Figure 3.6 shows a flow diagram of the main variables used in the track model. The lines with arrows are meant to represent variable dependence. For example, before the lateral shear displacement j_x can be calculated the variables z_i^* and \tilde{z}_i^* must be known. This section has six subsections. In Section 3.4.1, a model is given for computing the normal pressure acting on an individual discrete segment. In Section 3.4.2, a model is given for calculating the longitudinal shear displacement developed by a single element, along with the logic for computing the values of the points z_i^* for $i = 1..N$. In Section 3.4.3, a model for the longitudinal shear force acting on a discrete element is presented. This process is then repeated for the lateral variables. Finally in Section 3.4.6, a model is given for the resistive forces acting on the track of the tracked vehicle.

3.4.1 Discrete Normal Force Distribution Underneath the Track

The forces acting at the track-terrain interface are modeled using semi-empirical relationships, discussed in Chapter 2, that are influenced by the normal pressure developed under the track. The normal pressure is exerted by the terrain onto the

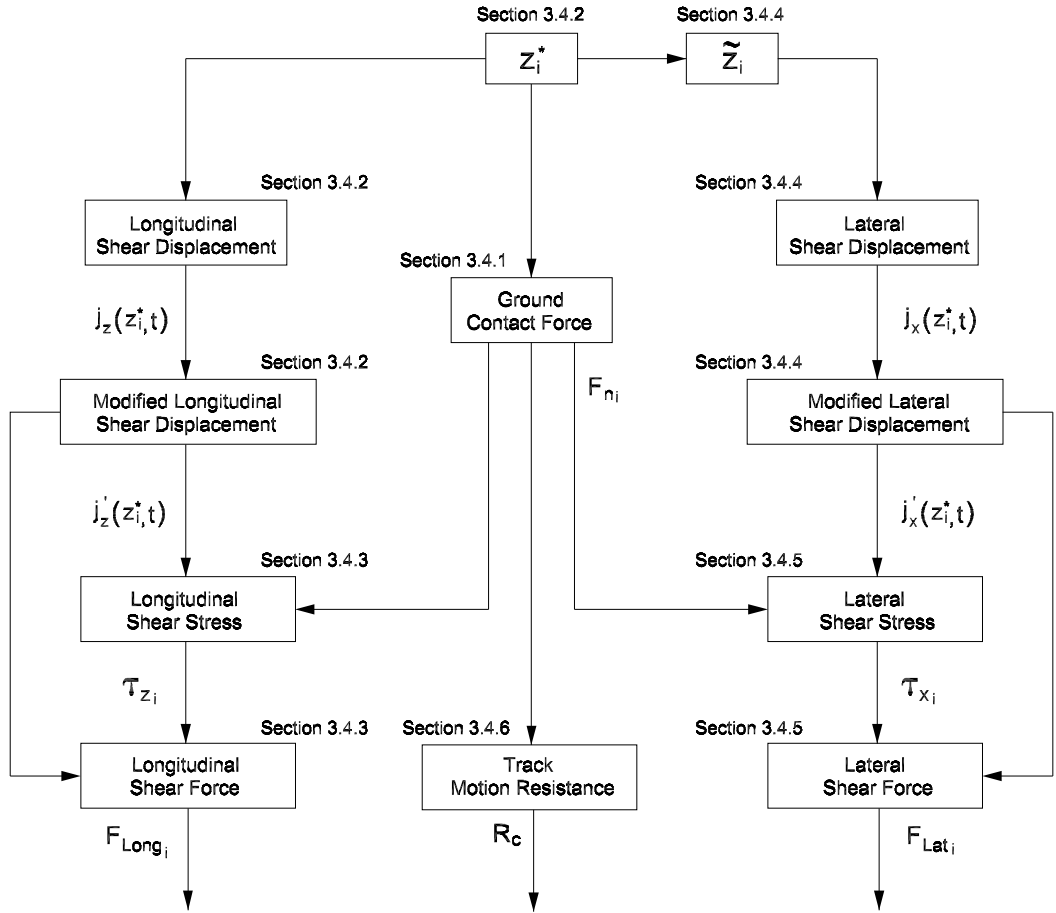


Figure 3.6: Flow Diagram for Modeling the Forces at the Track-Terrain Interface

tracks, which support the vehicle in a plane normal to the ground. In the discrete approach, the normal force acting on a discrete element is assumed to act at a single point, namely z_i^* . The normal pressure acting on the element is evenly distributed across the area of the element multiplying the computed normal force computed at z_i^* by the area of the element ΔA_i .

There are several contact models available in the ADAMS environment¹. These contact models use either the restitution method or the impact method. In general, the impact method is more numerically smooth and will result in faster simulations. Moreover, the impact method provides greater control of the contact behavior such as inclusion of damping, and force exponent, which can help tune a numerically smoother result. Therefore, the impact method was used to model the contact forces in ADAMS.

The impact method models the contact of two bodies as a compression-only nonlinear spring/damper system. ADAMS provides several types of impact models including solid-to-solid, one-sided impact function, and the two-sided impact function. The solid-to-solid model is not as numerically smooth as the one-sided and two-sided impact functions. The two-sided impact was not used since the track comes into contact on one side only, the ground. Therefore, the one-sided impact function was used to calculate the normal forces acting on the discrete elements. The impact force is computed as,

$$F_{Impact} = MAX \{0, K_s(q_0 - q)^e - C\dot{q}STEP(q, q_0 - d, q_0, 0)\}. \quad (3.3)$$

There are N impact functions required, one for each element composing the track-terrain model. Using Figure 3.7 as an aid, the following gives a description of both the variables q and \dot{q} and of the parameters K_s , C , e , d , and q_0 given in equation 3.3. Notice in the descriptions that only the wheel's reference frames are of importance,

¹See ADAMS/VIEW Function Builder Reference Manual

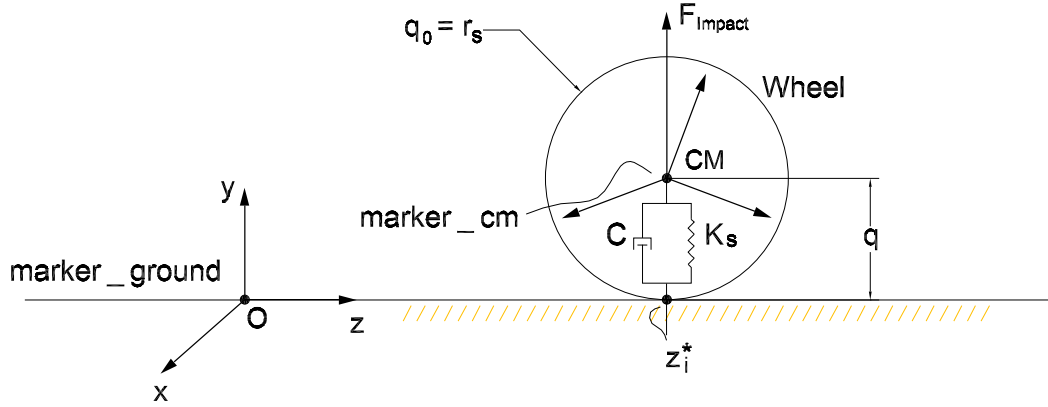


Figure 3.7: One-Sided Impact Model Used in ADAMS to Compute Normal Forces Acting on Discrete Elements

as these are needed by the impact function.

Position Variable (q) A measure of the distance between the two colliding bodies.

The value of q is computed by using the displacement function DY in ADAMS so that,

$$q = DY(marker_cm, marker_ground, marker_ground),$$

which defines the instantaneous displacement of $marker_cm$ with respect to $marker_ground$ along the y -axis of $marker_ground$.

Velocity Variable (\dot{q}) A measure of the time derivative of the distance between colliding bodies. The value of \dot{q} is computed using the velocity function in ADAMS so that

$$\dot{q} = VY(marker_cm, 0, marker_ground)$$

which defines the velocity of $marker_cm$ minus the velocity of $marker_ground$ (zero in this case since ground is fixed) along the y -axis of $marker_ground$.

Trigger for Displacement Variable (q_0) The independent variable value at which to turn the one-sided impact on and off. The impact function is turned on when the distance between marker_cm and marker_ground DY is less than the radius r_s of the wheel (compression). Therefore,

$$q_0 = r_s$$

Stiffness Coefficient (K_s) Stiffness coefficient of the spring force.

Stiffness Force Exponent (e) Exponent of nonlinear spring force.

Damping Coefficient (C) Damping coefficient for damper force.

Damping Ramp-up Distance (d) Distance over which to gradually turn on damping once impact is triggered.

Within a reasonable range, the values of the parameters K_s , C , e and d do not significantly change the results of the normal forces calculated by the impact function in ADAMS, but they do affect the distance DY the wheels sink into the ground. However, this does not create a problem because ADAMS does not know how sinkage influences the motion of the vehicle until it is explicitly defined. Recall from Section 2.5 that the sinkage of the vehicle causes external resistive forces to develop on the vehicle, and the sinkage is related to pressure using empirical soil parameters (e.g. k_ϕ , k_c and n). Thus, the external resistive forces due to sinkage are modeled in ADAMS (Section 2.5) using user-defined functions based on pressure-sinkage relationships as discussed in Chapter 2. These relationships are independent of the parameters K_s , C , e and d and of the displacement measurement DY . This implies that there are two “sinkages” used in the model: 1) The displacement DY of the wheel with respect to the ground, which is used in computing the normal force F_{Impact} , and 2) The sinkage \tilde{y} (Section 2.5) of the wheel due to any compacting of

Parameter	Value
K_s (N/m)	1000
C (N/s)	100
e	1
d (m)	0.001

Table 3.1: One-sided Impact Parameters

the soil, which is used in computing the external resistive forces.

The most significant consequence of the choice of values for the parameters K_s , C , e and d is their effect on the numerical solvers. A relatively stiff spring/damper system makes it more difficult for numerical solvers to integrate the equations of motion. Through a trial and error process, a set of values for K_s , C , e and d can be chosen that allow a simulation to run efficiently. Table 3.1 summarizes nominal values found to work well for the problem at hand.

In using the one-sided impact function, the point of application of the force must also be specified. Applying the principle of transmissibility, which states that “The external effect of a force on a rigid body is the same for all points of application of the force along its line of action”, each normal force was applied to the main body coincident with the center of its corresponding wheel and collinear with a line that passes through the center of the wheel and the corresponding point z_i^* as shown in Figure 3.4.

Using the normal force calculated by the impact function, the normal pressure σ_i acting on the i^{th} discrete element is given by,

$$\sigma_i = \frac{Fn_i}{\Delta A_i}, \quad (3.4)$$

where $Fn_i \equiv F_{Impact_i}$ and ΔA_i is the discrete area of the element. This pressure is used to calculate the shearing and resistive forces generated at each discrete element.

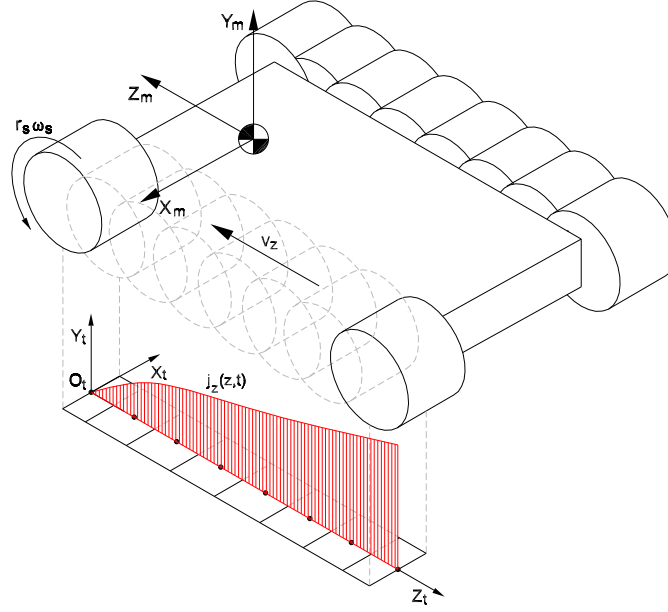


Figure 3.8: Longitudinal Shear Displacement Developed Underneath Track

3.4.2 Development of Kinematical Model for Longitudinal Shear Displacement

3.4.2.1 Base-Line Equations for Modeling Longitudinal Shear Displacement

During non-stationary motion the longitudinal shear displacement j_z in a reference frame fixed to the track (x_t, y_t, z_t) is generally a function of both time t and of the distance z from the origin O_t of the track coordinate system, as shown in Figure 3.8. A dynamic model of the longitudinal shear displacement, j_z , was derived by [4], in which they propose a model,

$$\frac{\partial j_z}{\partial t} + r_s \omega_s \frac{\partial j_z}{\partial z} = r_s \omega_s - v_z. \quad (3.5)$$

Here, the longitudinal shear displacement is solved along the z_t -axis of the track coordinate system. The right-hand-side of equation 3.5 is the slip velocity of the track with respect to the ground, which is common to all points z along the z_t -axis. The variables r_s and ω_s are the sprocket radius and the angular velocity of the sprocket, respectively, and v_z is the absolute longitudinal velocity of the track referenced to the reference frame fixed to the main body (x_m, y_m, z_m) . Equation 3.5 describes the dynamics of the shear displacement as a transport process, characterized by the boundary conditions,

$$\begin{cases} j_z(0, t) = 0 & \text{if } \omega > 0 \text{ (foreward motion)} \\ j_z(l, t) = 0 & \text{if } \omega < 0 \text{ (backward motion)} \end{cases} \quad (3.6)$$

and the initial condition,

$$j_z(z, 0) = 0. \quad (3.7)$$

Recall, in the “discrete” approach the longitudinal shear displacement at each point z_i^* for $i = 1..N$ is needed in order to compute the longitudinal shear stress acting on a corresponding discrete element. Ideally, equation 3.5 would be solved numerically for $j_z(z = z_i^*, t)$ for $i = 1..N$. However, this would be difficult to implement into the simulation since equation 3.5 is a partial differential equation containing both initial and boundary conditions. Therefore, the idea is to recover an ordinary differential equation from equation 3.5 to approximate the longitudinal shear displacement at the points z_i^* for $i = 1..N$. In the end, there will be N ordinary differential equations for each track, one for each point z_i^* .

We begin by assuming that,

$$\frac{\partial j_z}{\partial z} = \psi(t). \quad (3.8)$$

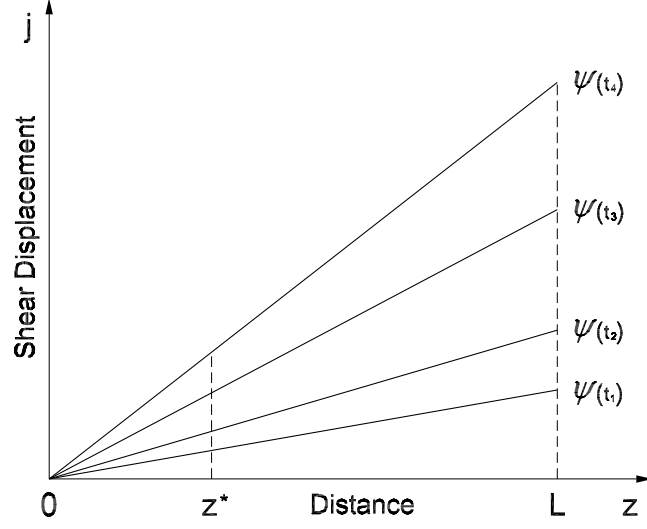


Figure 3.9: Longitudinal Shear Displacement Increasing Linearly Along the Track

Integrating equation 3.8 with respect to z yields,

$$j_z(z, t) = \psi(t)z + f(t). \quad (3.9)$$

Further assuming that $f(t) = 0$ gives,

$$j_z(z, t) = \psi(t)z. \quad (3.10)$$

Thus, the assumptions that have been made imply that the shear displacement increases linearly with respect to the spatial variable, z , along the length of the track with the slope of the line being a function of time, $\psi(t)$, as shown in Figure 3.9. Equation 3.10 is a rough approximation for transient motion conditions, but a linear profile for the shear displacement is indeed obtained under steady-state motion conditions [4]. Solving equation 3.10 for $\psi(t)$ and equating the result to

equation 3.8 yields,

$$\frac{\partial j_z}{\partial z} = \frac{j_z(z, t)}{z}. \quad (3.11)$$

Setting $z = z_i^*$ equation 3.11 becomes,

$$\left. \frac{\partial j_z}{\partial z} \right|_{z=z_i^*} = \frac{j_z(z_i^*, t)}{z_i^*}. \quad (3.12)$$

Similarly, setting $z = z_i^*$ yields the following relationship since z_i^* is essentially a parameter,

$$\left. \frac{\partial j_z}{\partial t} \right|_{z=z_i^*} = \frac{d}{dt} \psi(t) z_i^* \equiv \frac{d}{dt} j_z(z_i^*, t). \quad (3.13)$$

Evaluating equation 3.5 with $z = z_i^*$ and inserting equations 3.12 and 3.13 yields an ordinary differential equation for j_z as,

$$\frac{d}{dt} j_z(z_i^*, t) + \frac{r_s \omega_s}{z_i^*} j_z(z_i^*, t) = r_s \omega_s - v_z. \quad (3.14)$$

Equation 3.14 is an approximate dynamic model for the longitudinal shear displacement at a point z_i^* and there are N of these equations for each track. Equation 3.14 is a nonlinear first-order differential equation of the form

$$\frac{dy}{dt} + \alpha(t) y = g(t).$$

At steady-state, the variables j_z , ω_s , and v_z are independent of time, reducing equation 3.14 to

$$\frac{r_s \omega_s}{z_i^*} j_{z_{ssi}} = r_s \omega_s - v_z.$$

Solving for the steady-state shear displacement $j_{z_{ssi}}$ yields

$$j_{z_{ssi}} = \frac{r_s \omega_s - v_z}{r_s \omega_s} z_i^*. \quad (3.15)$$

Notice that this result is similar to the steady-state shear displacement derived in Section 2.4.3 given by equation 2.22 with the independent variable x replaced by z and with $V_t = r_s \omega_s$. The difference between the two equations is that equation 3.15 represents a number whose value depends on the index i , whereas equation 2.22 represents a function with x as the independent variable. Therefore, the steady-state solution of equation 3.14 is exact (theoretically) and the transient response is approximated.

Equation 3.14 satisfies the initial condition given by 3.7 by setting,

$$j(z_i^*, t = 0) = 0.$$

In order to have equation 3.14 satisfy the boundary conditions given by equation 3.6, the proper value of z_i^* must be used. The following section shows how the value of z_i^* is determined so that equation 3.14 satisfies the boundary conditions.

3.4.2.2 Defining the Value of z^* To Satisfy Boundary Conditions

The value of any point z_i^* for $i = 1..N$ depends on two things: 1) its location within its element and 2) the location of the track coordinate system along the contact patch. Both the size of the elements and the location of the points z_i^* within their respective element should be chosen to fit the application. Figure 3.10 shows a general partitioning of the track with various size elements with the points z_i^* positioned at arbitrary locations along the z_t -axis. A detailed description of the partitioning of the contact patch used for this model is given in Appendix C.

Once the locations of the points z_i^* have been fixed, the location of the track coordinate system (x_t, y_t, z_t) must be chosen so that the boundary conditions are satisfied. For ease of explanation, consider the steady-state shear displacement given

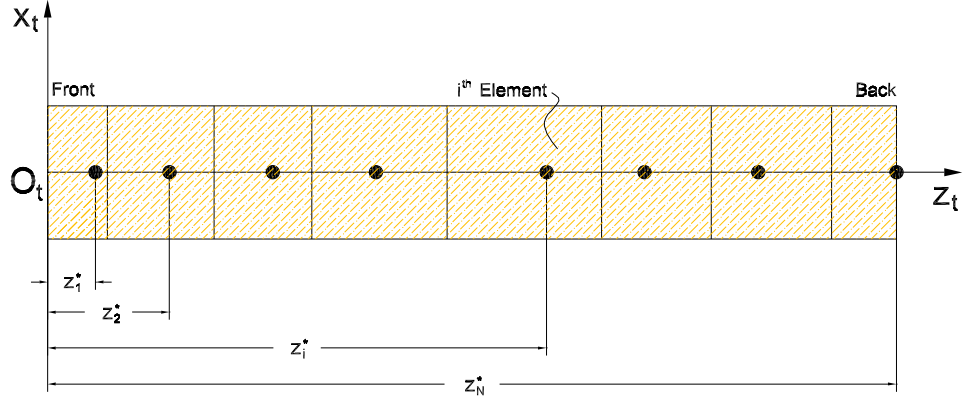


Figure 3.10: Top View of Partitioned Contact Patch

by equation 2.22 with $x = z$,

$$j_z = \frac{r_s \omega_s - v_z}{r_s \omega_s} z,$$

and the steady-state solution of equation 3.14 given by equation 3.15 which is,

$$j_{z_{ssi}} = \frac{r_s \omega_s - v_z}{r_s \omega_s} z_i^*.$$

Recall, equation 2.22 represents a function, while equation 3.15 represents a number. From Section 2.4.3, it was shown that when the vehicle is being driven forward $|r_s \omega_s| > |v_z|$ & $v_z > 0$, with all velocities measured relative to the main body reference frame, (x_m, y_m, z_m) , the shear displacement along the length of the track increases linearly from the front to the back of the contact patch. This solution is depicted by equation 2.22, which satisfies the boundary condition 3.6. It must be noted that in this section the velocity, v_z , is the longitudinal velocity of the track, which equals the longitudinal velocity at the center-of-mass of the vehicle for *only* straight-line motion. For equation 3.15 to satisfy the boundary equation 3.6 when the track is being driven forward requires $z_1^* = 0$, if z_1^* is chosen to be at the front

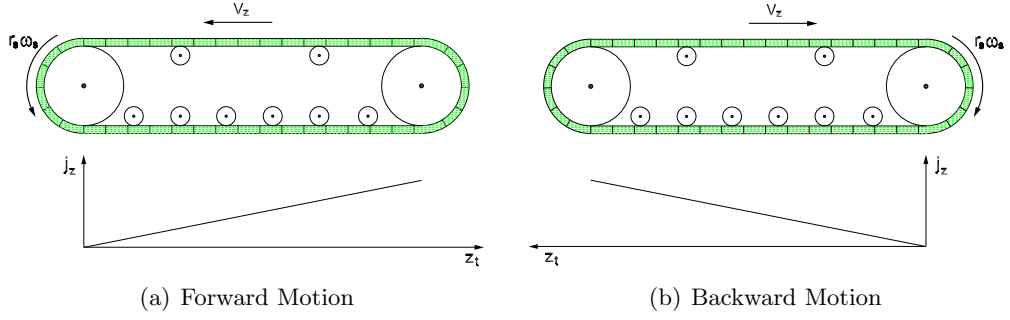


Figure 3.11: Determining the Position of Track Frame

of the contact patch. This also implies that,

$$z_1^* < z_2^* < \dots < z_i^* < \dots < z_N^*.$$

In other words, the origin of the track coordinate system is located at the front of the contact patch, with the points z_i^* for $i = 1..N$ increasing from the front to the back of the contact patch as shown in Figure 3.11(a).

Now suppose the track is being driven backwards $|r_s \omega_s| > |v_z|$ & $v_z < 0$. This would require a modification of equation 2.22 to be,

$$j_z = \frac{r_s \omega_s - v_z}{r_s \omega_s} (L - z),$$

so that the shear displacement increases linearly from the back to the front of the contact patch. An equivalent approach is to have the origin O_t of the track coordinate system be located at the rear of the contact patch as in Figure 3.11(b) so that equation 2.22 remains valid. This would imply,

$$z_1^* > z_2^* > \dots > z_i^* > \dots > z_N^*,$$

and if z_N^* is located at the very end of the contact patch the boundary condition

equation 3.6 requires $z_N^* = 0$.

There are other possible conditions that can arise, such as braking. The following logic determines the direction the values of z_i^* increase along the z_t -axis of the track coordinate system.

$$\begin{aligned} \text{(Front-to-Back)} & \left\{ \begin{array}{l} \text{if } r_s \omega_s = 0 \text{ and if } v_z \geq 0 \\ \text{or} \\ \text{if } r_s \omega_s \geq 0 \end{array} \right. \\ \text{(Back-to-Front)} & \left\{ \begin{array}{l} \text{if } r_s \omega_s = 0 \text{ and if } v_z < 0 \\ \text{or} \\ \text{if } r_s \omega_s < 0 \end{array} \right. \end{aligned}$$

Notice that some conditions require a value to be exactly zero. This can lead to computational errors when using numerical solvers. The value of a given variable will rarely be exactly zero. For this reason, a variable was introduced as ΔV_z so that a condition requiring a value of zero was satisfied as long as the value of the variable fell within the interval $(-\Delta V_z, \Delta V_z)$. For example, the last condition in the logic given above would be satisfied if,

$$|r_s \omega_s| - \Delta V_z > 0 \quad \text{and} \quad r_s \omega_s < 0.$$

3.4.2.3 Implementing Longitudinal Shear Displacement Model in ADAMS

The longitudinal shear displacement model given by equation 3.14,

$$\frac{d}{dt} j_z(z_i^*, t) + \frac{r_s \omega_s}{z_i^*} j_z(z_i^*, t) = r_s \omega_s - v_z,$$

was derived assuming a partial solution to equation 3.5. Therefore, equation 3.14 does not capture all the dynamics characterizing the longitudinal shear displace-

ment at a given point z_i^* . The steady state response depicted by equation 3.14 is theoretically exact, but the transient response is relatively slow. This creates a problem when the longitudinal slip velocity of the track $r_s\omega_s - v_z$ declines rapidly towards zero. When the longitudinal slip velocity suddenly approaches zero the shear displacement along the length of the track and in turn the longitudinal forces should approach zero fairly quickly (assuming no resistive losses). However, because the transient response predicted by equation 3.14 is relatively slow, predicted longitudinal forces would be nonzero even after the slip velocity has dropped towards zero for a period of time. Therefore, the idea is to saturate the longitudinal shear displacement at very low slip velocities and have equation 3.14 model the shear displacement for low to high slip velocities.

There is a function provided in ADAMS (called the STEP5 function) that can be used to fix this problem. The STEP5 function has a syntax,

$$M = STEP5[x, x_0, h_0, x_1, h_1]. \quad (3.16)$$

With the aid of Figure 3.12, a description of each parameter in equation 3.16 is given along with the variables used to model the longitudinal shear displacement.

M : This is the dependent variable. For the shear stress model, the dependent variable is the modified shear stress $j'_z(z_i^*, t)$.

x : This is the independent variable. For the shear stress model, the dependent variable is the absolute value of the longitudinal slip velocity $|r_s\omega_s - v_z|$, since we are only interested in the magnitude.

x_0 : Value of independent variable at which STEP5 begins. Since the absolute value of the slip velocity is the independent variable, x_0 is a positive real number.

x_1 : Value of independent variable at which STEP5 ends. Since the absolute value of the slip velocity is the independent variable, x_1 is positive real number.

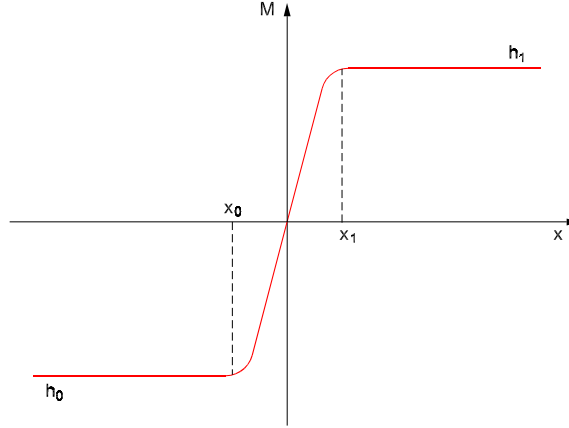


Figure 3.12: Illustration of STEP5 Function

h_0 : This is the initial function value. At very low slip velocities, less than x_0 , we set the shear displacement to zero.

h_1 : This is the final value function. At slip velocities larger than x_1 we let equation 3.14 compute the shear displacement.

Therefore, using the STEP5 function the modified longitudinal shear displacement is defined in ADAMS as,

$$j'_z(z_i^*, t) = STEP5 \left[|r_s \omega_s - v_z|, x_{0_{jz}}, 0, x_{1_{jz}}, j_z(z_i^*, t) \right]. \quad (3.17)$$

Figure 3.13 illustrates how equation 3.17 is defined in ADAMS. Although Figure 3.13 looks odd and nothing like Figure 3.12 there is a reason. In Figure 3.12 the function values h_0 and h_1 are illustrated as being constants. In Figure 3.13 the final function value $j_z(z_i^*, t)$ is a variable. For slip velocity values greater than $x_{1_{jz}}$, the shear displacement is modeled by equation 3.14. When the slip velocity becomes less than $x_{1_{jz}}$, the STEP5 function takes over modeling the shear displacement. This process is illustrated by the paths taken by the points shown in Figure 3.13 as the slip velocity decreases with respect to time. The slope of the shear displacement

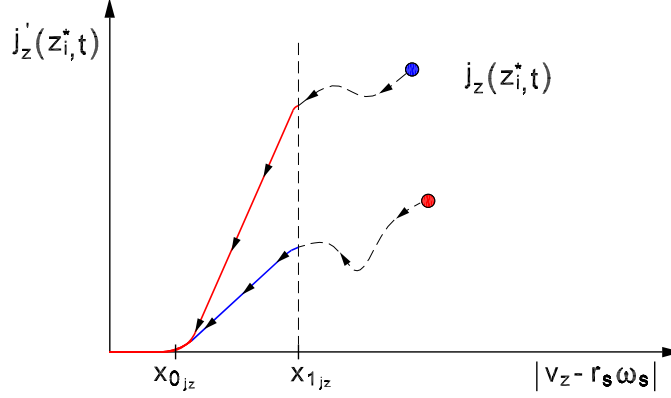


Figure 3.13: Modified Longitudinal Shear Displacement Modeled Using the STEP5 Function in ADAMS

vs. slip line used by STEP5 depends on the location where the point crosses the vertical dashed line defined by $x_{1_{jz}}$.

There is a drawback in using the STEP5 function for modeling the longitudinal shear displacement. This function introduces two additional parameters into the model, $x_{0_{jz}}$ and $x_{1_{jz}}$, and values for these parameters must be selected by tuning the model. The values of these parameters may depend either on how the track is discretized or on the length of the track. However, the same values (see Appendix C) for the parameters $x_{0_{jz}}$ and $x_{1_{jz}}$ may be used for all STEP5 functions used in this model to represent the longitudinal shear displacements at the points z_i^* for $i = 1..N$.

3.4.3 Model Derivation of Longitudinal Shear Forces

3.4.3.1 Baseline Equations for Modeling Longitudinal Shear Forces

The thrust developed by the vehicle during driving operation is composed of the longitudinal forces acting on the discrete elements making-up the contact patch. When the vehicle is braking, the longitudinal forces act as resistive forces retarding

the motion of the vehicle. The longitudinal force acting on the i^{th} discrete element is given by,

$$F_{Long_i} = SIGN(j'_{z_i}) \tau_{z_i} \Delta A_i, \quad (3.18)$$

where j'_{z_i} is the modified longitudinal shear displacement, τ_{z_i} is the longitudinal shear stress acting on the i^{th} element, and ΔA_i is the area of the i^{th} discrete element. The longitudinal shear stress acting on an element is found using one of the shear stress-shear displacement relationships discussed in Chapter 2, depending on the type of the terrain. For most disturbed soils, the longitudinal shear stress τ_{z_i} acting on the i^{th} discrete element may be given by,

$$\tau_{z_i} = (c + \sigma_i \tan \phi)(1 - e^{-|j'_{z_i}|/K}), \quad (3.19)$$

where j'_{z_i} is the modified longitudinal shear displacement calculated at the point z_i^* , σ_i is the normal pressure acting on the i^{th} element and c , ϕ , and K are empirical soil parameters discussed in Chapter 2.

Ideally, the longitudinal force would be applied at its corresponding point z_i^* (lowest point of the wheel). However, this is not an easy force to represent in ADAMS because you can't place a force at the moving interface without changing the orientation of the force. Instead, the longitudinal force acting on each element is replaced with an equivalent force-couple system as shown in Figure 3.14. The force is applied at the center of the wheel and is given by equation 3.18. A couple is needed to compensate for the change of the line of action of the original force. The couple is also applied at the center of the wheel and is given by,

$$\tau_{Back_i} = r_s F_{Long_i} \quad (3.20)$$

This couple is referred to as the back torque, which tends to oppose the torque applied by the motor.

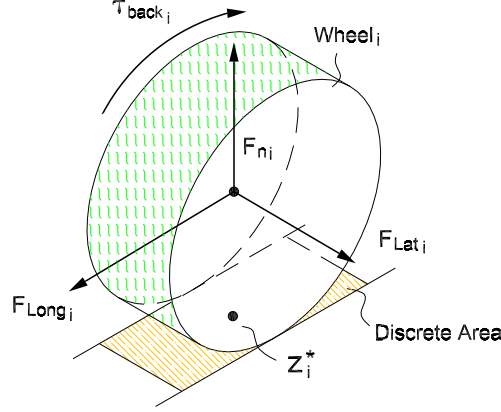


Figure 3.14: Forces Applied at the Origin of the Wheel's Reference Frame

The total longitudinal force developed by a single track is simply found by summing the longitudinal forces acting on each element so that,

$$F_{Long} = \sum_{i=1}^N SIGN(j'_{z_i}) \tau_i \Delta A_i. \quad (3.21)$$

Notice the similarities between equation 3.21 and the Riemann Sum used to approximate the area under the curve given by equation 3.1. The function $f(x_i^*)$ used in the Riemann Sum is analogous to $\tau_i = \tau_i(z_i^*, t)$, and Δx_i^* is analogous to $\Delta A_i = b \Delta z_i$.

Finally, the total back torque that the motor must overcome is,

$$\tau_{Back} = r_s \sum_{i=1}^N F_{Long_i}. \quad (3.22)$$

3.4.3.2 Implementing Longitudinal Force Model In ADAMS

Equation 3.18 includes the function $SIGN(j'_{z_i})$, which is discontinuous and often causes problems for the numerical solvers in ADAMS. For this reason, the continuous STEP5 function was used in place of the SIGN function to model the longitudinal

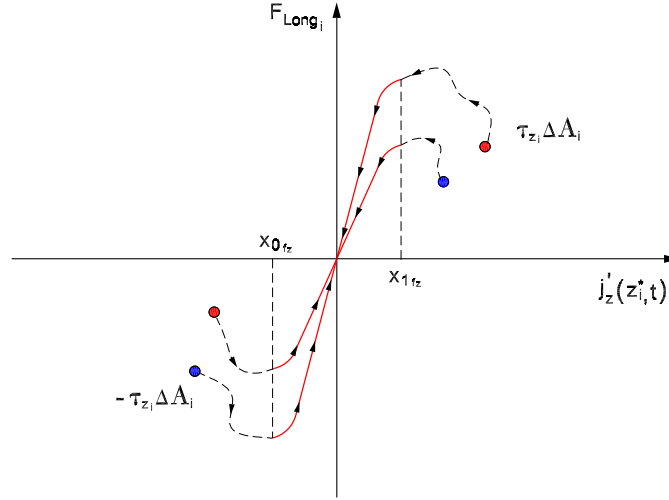


Figure 3.15: Implementation of Longitudinal Forces In ADAMS Using the STEP5 Function

force. In ADAMS the longitudinal force acting on the i^{th} element is computed as,

$$F_{Long_i} = STEP5(j'_{z_i}, x_{0_{fz}}, -\tau_{z_i} \Delta A_i, x_{1_{fz}}, \tau_{z_i} \Delta A_i). \quad (3.23)$$

Figure 3.15 illustrates how equation 3.23 is defined in ADAMS. If the value of j'_{z_i} lies outside the interval $(x_{0_{fz}}, x_{1_{fz}})$, then the longitudinal force is given by $\pm \tau_{z_i} \Delta A_i$. If the value of j'_{z_i} is within the interval $(x_{0_{fz}}, x_{1_{fz}})$, then the STEP5 function takes over modeling the longitudinal force. The points shown in Figure 3.15 illustrate this process as the magnitude of j'_{z_i} begins to decrease. The particular function STEP5 uses to model the force when the value of j'_{z_i} is within the interval $(x_{0_{fz}}, x_{1_{fz}})$ depends on the location where the points cross the vertical dashed lines.

As the points $x_{0_{fz}}$ and $x_{1_{fz}}$ are chosen to be closer to zero, the slope of the force vs. shear displacement line will increase. The SIGN function implies that points $x_{0_{fz}}$ and $x_{1_{fz}}$ are zero, meaning the value of the slope of the line between the points is infinity. This rapid change in value is what causes problems for the

numerical solvers. Once again, a drawback is that the values of the points $x_{0_{fz}}$ and $x_{1_{fz}}$ must be selected by tuning the model. It was assumed that the same values (see Appendix C) for $x_{0_{fz}}$ and $x_{1_{fz}}$ may be used for all STEP5 functions used in this model to represent the longitudinal forces. Although not proven, this seems plausible since all points z_i^* for $i = 1..N$ share the same longitudinal slip velocity. Also, the slope of the lines shown in Figure 3.15 are exaggerated. The STEP5 function is computationally smooth, even when the points $x_{0_{fz}}$ and $x_{1_{fz}}$ are relatively small. This makes the slope of the force vs. shear displacement relatively steep. Thus, any deviations in values of $x_{0_{fz}}$ and $x_{1_{fz}}$ should not be significant.

3.4.4 Development of Kinematical Model for Lateral Shear Displacement

The lateral shear forces give rise to a moment of turning resistance opposing the yaw motion of the vehicle. In the literature, various models have been presented for characterizing the lateral shear forces. In [14], Steeds assumes that the shear stress developed under the track obeys the law of Coulomb friction. This implies that the shear stress on the track-ground interface reaches a maximum value instantly, as soon as a small relative motion between the track and the ground takes place. This view was argued in both [1] and [17], in which Wong and Kar investigate the variation of the track forces with the turning radius of the vehicle. Wong and Kar argue that the lateral coefficient of friction is a function of the turning radius of the vehicle, explaining why the track forces decrease with an increasing turning radius. Based on this argument, we could model the lateral shear force acting on the i^{th} discrete element as,

$$F_{Lat_i} = \mu_t(\rho_i) F_{n_i} \quad (3.24)$$

where μ_t is the lateral coefficient of friction that is a function of the turning radius ρ_i of the i^{th} wheel, and F_{n_i} is the normal force acting on the i^{th} discrete element.

However, the relationship between μ_t and ρ_i depends on the type of terrain and the design of the track. Since no data was available quantifying the relationship between μ_t and ρ_i for the particular robotic tracked vehicle being modeled, a new approach was taken. In [19], Rubinstein and Hitron assume a model for the lateral shear forces that is similar to the model for the longitudinal forces derived in Section 3.4.3. This means that the same shear stress-shear displacement relationship may be used to model the lateral forces. This is beneficial since the same shear stress parameters c , ϕ , and K may be used without introducing additional parameters. Therefore, this approach was adopted for modeling the lateral shear forces developed at the track-terrain interface.

3.4.4.1 Baseline Equations for Modeling Lateral Shear Displacement

Similar to the longitudinal shear-displacement, the lateral shear displacement developed underneath the track is modeled as a first-order partial differential equation given by,

$$\frac{\partial j_x}{\partial t} + r_s \omega_s \frac{\partial j_x}{\partial z} = v_x \quad (3.25)$$

where v_x is the lateral slip velocity with respect to the x_m -axis of the main body of a point located a distance z from the origin O_t of the track coordinate system as shown in Figure 3.16. Focus will be on this model, although it is recognized that other models can be proposed. A derivation is presented in Appendix C showing how the lateral shear displacement model given by equation 3.25 is equivalent to the model given in [19]. The solution to equation 3.25 must satisfy the following boundary conditions,

$$\begin{cases} j_x(0, t) = 0 & \text{if } \omega > 0 \text{ (forward motion)} \\ j_x(L, t) = 0 & \text{if } \omega < 0 \text{ (backward motion)} \\ j_x(\tilde{z}, t) = 0 \end{cases} \quad (3.26)$$

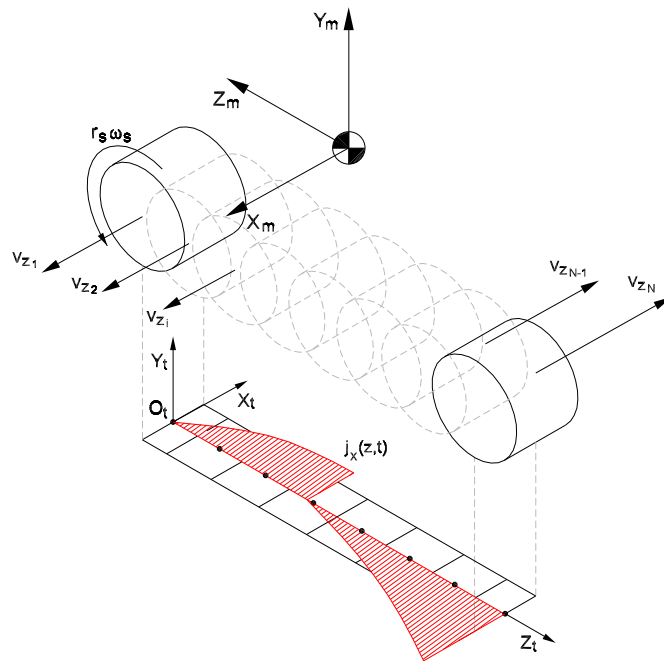


Figure 3.16: Lateral Shear Displacement Developed Underneath Track

and the following initial condition,

$$j_x(z, 0) = 0. \quad (3.27)$$

As in Section 3.4.2 for the longitudinal shear displacement, the idea is to recover an ordinary differential equation from equation 3.25 to approximate the lateral shear displacement at the points z_i^* for $i = 1..N$. Thus, there will again be N ordinary differential equations for each track. Making the same assumptions as in Section 3.4.2, the equations for lateral shear displacement are,

$$\frac{d}{dt}j_x(z_i^*, t) + \frac{r_s\omega_s}{z_i^*}j_x(z_i^*, t) = v_{x_i}, \quad (3.28)$$

where v_{x_i} is the velocity of the point z_i^* relative to the ground referenced along the x_m -axis of the main body.

3.4.4.2 Modifying Dynamic Model of Lateral Shear Displacement to Satisfy Boundary Conditions

The first two boundary conditions in 3.26 are the same as the boundary conditions for the longitudinal shear displacement given by equation 3.6. Thus, the logic used to determine the value of z_i^* discussed in Section 3.4.2 also applies to satisfying the first two boundary conditions in 3.26. The third boundary condition for the lateral shear displacement involves the variable \bar{z} . In order to understand this boundary condition, consider the simple example of a bead sliding along a rotating bar about a fixed point \bar{z} with an angular velocity Ω as shown in Figure 3.17. The bar represents the track and the bead represents a point moving along the bottom portion of the track. The bead slides along the bar (radially) with a velocity $r_s\omega_s$ and with a tangential velocity v_θ . The lateral shear displacement of the bead as it moves along

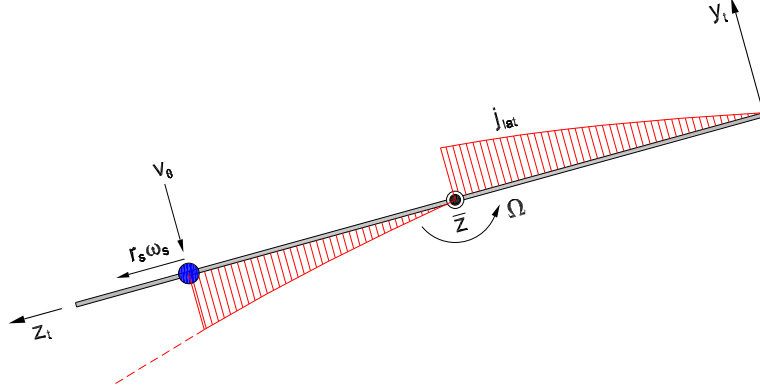


Figure 3.17: Analogy to Describe Lateral Shear Displacement

the bar is calculated by

$$j_{lat} = \int_0^{t'} v_{\theta} dt$$

Initially, the lateral shear displacement is zero and then increases as the bead approaches the fixed point \bar{z} . However, the tangential velocity of the bead decreases as it approaches \bar{z} , where its lateral velocity becomes zero. As soon as the bead crosses the fixed point \bar{z} , its tangential velocity changes directions and then increases as the bead moves further away from \bar{z} . This implies that the lateral shear displacement goes back to zero at \bar{z} and then increases as it continues down the bar. Thus, the third boundary condition in 3.26 implies that the lateral shear displacement is zero at the point \bar{z} , where the lateral velocity of the bottom portion of the track is zero.

The value of \bar{z} depends on the location of the track coordinate system. If the track coordinate system is located at the front of contact patch then the location of \bar{z} is

$$\bar{z} = \frac{v_{x1}}{v_{x1} - v_{xN}} L \quad (3.29)$$

and if the track coordinate is located at the rear of the contact patch then \bar{z} is,

$$\bar{z} = \frac{v_{x_N}}{v_{x_N} - v_{x_1}} L, \quad (3.30)$$

where v_{x_1} and v_{x_N} are the lateral velocity of the first (front) and the N^{th} (rear) wheel respectively. A new variable \tilde{z}_i^* is defined as,

$$\tilde{z}_i^* = \begin{cases} z_i^* & \text{if } z_i^* < \bar{z} \\ z_i^* - \bar{z} & \text{if } z_i^* \geq \bar{z}. \end{cases} \quad (3.31)$$

Using equation 3.31 in equation 3.28 yields,

$$\frac{d}{dt} j_x(z_i^*, t) + \frac{r_s \omega_s}{\tilde{z}_i^*} j_x(z_i^*, t) = v_{x_i}. \quad (3.32)$$

Thus, equation 3.32 is consistent with the boundary conditions set by 3.26 for the lateral shear displacement along the bottom portion of the track.

3.4.4.3 Implementing Lateral Shear Displacement Model In ADAMS

Similar to the model for the longitudinal shear displacement, the model for the transient response depicted by equation 3.32 is relatively slow. To fix this problem, the STEP5 function is used to model the lateral shear displacement for small lateral slip velocities. The lateral shear displacement was modeled in ADAMS as,

$$j_x'(z_i^*, t) = STEP5[v_{x_i}, x_{0_{j_x}}, 0, x_{1_{j_x}}, j_x(z_i^*, t)]. \quad (3.33)$$

The lateral forces are developed under the track only when the vehicle is turning and contribute to the moment of turning resistance. When the vehicle straightens out after performing a turning maneuver, such as in a lane change maneuver, the lateral forces diminish. But, the transient response of equation 3.32 is relatively

slow. In a simulation, the lateral forces would still be predicted after the vehicle has been commanded to straighten out after performing a turning maneuver. The STEP5 function fixes this problem by saturating the lateral forces to zero. As before, this introduces two additional parameters into the model, namely $x_{0_{jx}}$ and $x_{1_{jx}}$. The values for these parameters must be selected by tuning the model. The values for these parameters may depend on the size of the track and the way the track was discretized. The same values for these parameters maybe used for all STEP5 function used in this model to represent the lateral shear displacements at the points z_i^* for $i = 1..N$.

3.4.5 Model Derivation of Lateral Shear Forces

3.4.5.1 Baseline Equations for Modeling Lateral Shear Forces

The lateral forces acting on the discrete elements of the contact patch contribute to the moment of turning resistance that the longitudinal forces must overcome to turn the tracked vehicle. The lateral force developed on the i^{th} discrete element is given by,

$$F_{Lat_i} = -SIGN(j'_{x_i})\tau_{x_i}\Delta A_i \quad (3.34)$$

where j'_{x_i} is the modified lateral shear displacement, τ_{x_i} is the lateral shear stress acting on the i^{th} element, and ΔA_i is the area of the i^{th} element. The lateral force also acts in the opposite direction of the modified lateral shear displacement. For most disturbed soils, the lateral shear stress τ_{x_i} acting on the i^{th} discrete element may be given by,

$$\tau_{x_i} = (c + \sigma_i \tan \phi)(1 - e^{-|j'_{x_i}|/K}) \quad (3.35)$$

where j'_{x_i} is the modified lateral shear displacement calculated at the point z_i^* , σ_i is the normal pressure acting on the i^{th} element and c , ϕ , and K are empirical soil parameters discussed in Chapter 2.

As in the case for the longitudinal forces, the lateral forces are applied at the center of wheels. However in this case, the effects of changing the line of action of the lateral forces are neglected. In reality, the lateral forces would create a moment causing the vehicle to roll. However, the effect of forces on the roll and pitch of the vehicle are not taken into account in this model, which focus is made on the two-dimensional motion of the vehicle.

3.4.5.2 Implementing Lateral Force Model Into ADAMS

Similar to the implementation of the longitudinal force in ADAMS, the SIGN function used to compute the lateral force in equation 3.34 is replaced with the STEP5 function. Therefore, in ADAMS the longitudinal force acting on the i^{th} element is computed,

$$F_{Lat_i} = STEP5(j'_{x_i}, x_{0_{fx}}, \tau_{x_i} \Delta A_i, x_{1_{fx}}, -\tau_{x_i} \Delta A_i). \quad (3.36)$$

This introduces two additional parameters into the model, namely $x_{1_{fx}}$ and $x_{1_{fx}}$. The values of these parameters must be selected by tuning the model. The same values for these parameters maybe used for all STEP5 function used in this model to represent the lateral forces.

3.4.6 Resistive Forces

In Section 2.4 the various external resistive forces acting on a vehicle when operating over soft terrain were described. For this model, the resistive forces due to the bulldozing effect and to soil drag are neglected because the relatively light robotic vehicle does not exert enough pressure on the terrain to cause significant sinkage. Although the sinkage of the vehicle is relatively small, the resistive force due to the compacting of the terrain is included in the model and it provides a dissipating effect.

The work done in compacting the terrain by a single discrete element making

a rut of track width b , length Δz_i and depth y_{0_i} is,

$$\begin{aligned} Work_i &= \int_0^{y_{0_i}} p_i (\Delta A_i) dy \\ &= \Delta A_i \int_0^{y_{0_i}} k y_i^n dy \\ &= \frac{A_i}{n+1} k y_{0_i}^{n+1}, \end{aligned} \quad (3.37)$$

where the pressure sinkage relationship (equation 2.2) proposed by Bekker was used in the form,

$$p_i = k y_i^n \quad \text{and} \quad k = (k_c/b + k_\phi).$$

Again, using the pressure sinkage relationship, with $y = y_{0_i}$, to solve for y_{0_i} yields,

$$y_{0_i} = \left(\frac{p_i}{k} \right)^{\frac{1}{n}}.$$

Also the pressure can be expressed as,

$$p_i = \frac{F n_i}{\Delta A_i}.$$

Inserting the above two relationships into equation 3.37 yields,

$$Work_i = \frac{\Delta A_i}{(n+1)k^{(1/n)}} \left(\frac{F n_i}{\Delta A_i} \right)^{\frac{n+1}{n}}. \quad (3.38)$$

The total work of a single track in compacting the terrain is found by summing the work done by each element,

$$Work = \sum_{i=1}^N \frac{\Delta A_i}{(n+1)k^{(1/n)}} \left(\frac{F n_i}{\Delta A_i} \right)^{\frac{n+1}{n}}. \quad (3.39)$$

The work done by the motion resistance R_c as the track is pulled a distance l can be equated to the work done in compacting the terrain making a rut of length l so

that the motion resistance can be calculated by,

$$\begin{aligned} lR_c &= \sum_{i=1}^N \frac{\Delta A_i}{(n+1)k^{(1/n)}} \left(\frac{Fn_i}{\Delta A_i} \right)^{\frac{n+1}{n}} \\ R_c &= \sum_{i=1}^N \frac{\Delta A_i}{(n+1)lk^{(1/n)}} \left(\frac{Fn_i}{\Delta A_i} \right)^{\frac{n+1}{n}}. \end{aligned} \quad (3.40)$$

There is also another type of resistive force that was not mentioned in Section 2.4. This resistive force is referred to as the internal resistance of the track, which is due to the frictional losses in track pins, between the driving sprocket teeth and track, in the roadwheel bearings, and by the rolling resistance of the roadwheels on the track. However, no analytical models have been presented in the literature that accurately predict this phenomenon, so empirical models are generally applied. In this study, the internal resistance has been modeled as a linear viscous torque acting around the sprocket shaft. The internal viscous torque is given by

$$\tau_{int} = b_{int}\omega_s, \quad (3.41)$$

where b_{int} is a damping coefficient that is dependent on the terrain. Figure 3.18 shows how the resistive forces were applied to the track.

3.4.6.1 Implementing Motion Resistance Model Into ADAMS

The magnitude of the motion resistive force R_c is given by equation 3.40, which does not specify the direction of the force. The direction of the resistive force should always act in the opposite direction of the longitudinal track velocity v_z . This would require the SIGN function to be used, but as has been the case throughout this thesis the SIGN function is replaced with the STEP5 function, so that the resistive force

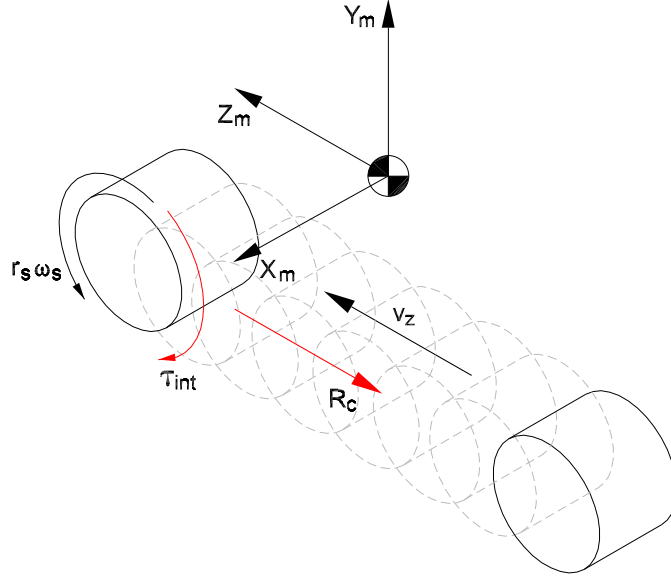


Figure 3.18: Resistive Forces Acting on Track

is modeled in ADAMS as,

$$\text{Resistive Force} = \text{STEP5} [v_z, x_{0_{Rc}}, -R_c, x_{1_{Rc}}, R_c], \quad (3.42)$$

where R_c is given by equation 3.40. Figure 3.19 shows how equation 3.42 is computed in ADAMS using the STEP5 function.

3.5 Summary of Limiting Assumptions Made for Track-Terrain Model

The basic concept of the discrete approach is to model the track-terrain interaction similar to a rigid footing, in which the interface is partitioned into N discrete elements. Each element has an area ΔA_i and is assigned a fixed point z_i^* . A coordinate system, fixed to the track, is set to determine the relative location of the

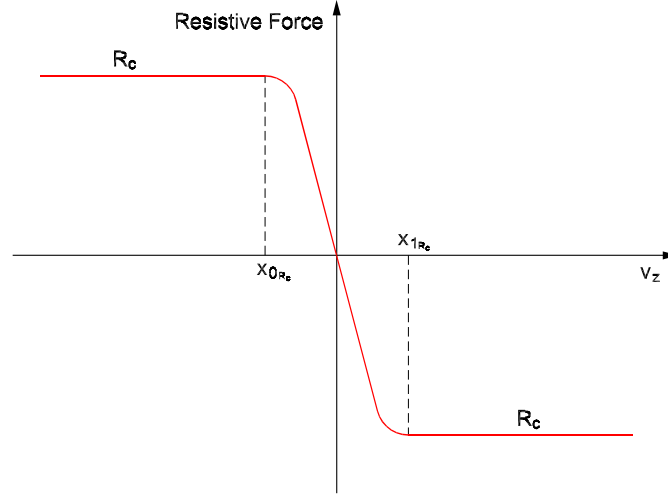


Figure 3.19: Illustration of Motion Resistive Force Implemented Into ADAMS

points z_i^* for $i = 1..N$ from the origin of the coordinate system. All of the dynamical variables (e.g. shear displacement, shear stress, normal pressure, etc...) describing the interaction of the i^{th} element with the terrain are functions of the independent variables z_i^* and time t . Three mutually perpendicular forces are modeled to act at the point z_i^* : the longitudinal shear force, the lateral shear force, and the ground normal force. In its basic form, this entails the discrete approach. The process in which to model the various forces, such as Bekker and Wong correlations used in classical soil mechanics, is completely up to the designer.

This chapter presented a derivation of a track model for a particular tracked vehicle using the discrete approach. In this process various assumptions were made. These assumptions are categorized into two groups: model/physics based assumptions and computational based assumptions. The following assumptions have been introduced.

Model/Physics Based Assumptions

- The track is modeled similar to a rigid footing.
- The ground contact force is modeled in ADAMS as a nonlinear spring/damper system acting at a single point (Section 3.4.1).
- The interaction of the grousers with the terrain is neglected.
- The track is assumed to be inextensible and it is assumed there is no slip between the sprocket and track. As a consequence, the linear velocity of the belt relative to the track and the angular velocity of the sprocket are algebraically related.
- The effect of forces on the roll and pitch of the vehicle are not taken into account in this model, which focus is made on the two-dimensional motion of the vehicle. These effects can be accounted for in an extended (more complex) model that accounts for the three-dimensional nature of a terrain.
- Air drag is neglected.
- The frictional losses due to the rolling resistance of the track is modeled using a linear viscous friction torque acting around the sprocket shaft (section 3.4.6).
- The longitudinal and lateral shear stress developed under the track are assumed to be decoupled.
- Lateral bulldozing effect is neglected, which can be significant in soft terrains like dry sand.
- The lateral shear forces acting under the track are modeled using the shear stress-shear displacement relationship,

$$\tau = (c + \sigma \tan \phi) \left(1 - e^{-j/K}\right),$$

where τ is the shear stress, j is the shear displacement, σ is the normal pressure, and c , ϕ , and K are soil parameters. Commonly, in the literature, the amplitude of the lateral resistive force is modeled to be directly related to the normal load through a coefficient of lateral resistance $\mu_t(\rho)$, which is a function of turning radius ρ . This relationship depends on the terrain and the design of the track. Since data is not available for the particular robotic tracked vehicle being model, the shear stress-shear displacement relationship is used (Section 3.4.5.2).

- The baseline equations used to model the longitudinal and lateral shear displacements were derived by assuming a solution to more accurate models characterized by partial differential equations. The transient response depicted by these baseline equations were relatively slow causing problems when the slip velocity components of the track declined rapidly towards zero. Therefore, the STEP5 function in ADAMS was used to saturate the shear displacements to zero at very low slip velocities (sections 3.4.3.2 and 3.4.4.3).

Computational Based Assumptions

The baseline equations used to model both the longitudinal and lateral forces and the external motion resistance use the SIGN function, which is discontinuous and often causes problems for the numerical solvers. The continuous STEP5 function provided in ADAMS was used in replace of the discontinuous SIGN function (sections 3.4.3.2 and 3.4.5.2 and 3.4.6.1).

The last page of the chapter gives a description of all the parameters needed to simulate the track-terrain model.

3.6 Conclusion

A new approach to modeling the dynamics at the track-terrain interface has been discussed. Based on this new approach, a development of the baseline equations used to describe the various forces acting on the vehicle have been derived. Also, a discussion of how these baseline equations were implemented in the ADAMS modeling environment was discussed.

To conclude this chapter, a comparison is made between the track model presented in the work [4] and the track model presented in this chapter using the discrete approach. The two models are similar, yet there are distinct differences. In [4], Ferretti and Girelli partition the bottom portion of the track into two equal sections, whereas in the discrete model presented here the track is partitioned into N discrete elements. Ferretti and Girelli assign a reference frame to the center of both the idler and sprocket of the track. These reference frames are used in a similar manner as the wheel reference frames used in the discrete model, discussed in Section 3.2. Ferretti and Girelli compute a mean value for the longitudinal shear displacement for the entire track, whereas in the discrete model the shear displacement is calculated at various points, z_i^* , along the bottom portion of the track. Ferretti and Girelli apply a single longitudinal force at the lowest end of the sprocket pitch circle and a lateral force at the middle of each section. In the discrete model, each element develops a longitudinal and lateral shear force. These forces are applied at the origin of the wheel's reference frame. In addition, a torque is applied to each wheel to compensate for the change in the line of action of the longitudinal force. The effect in changing the line of action for the lateral force in the discrete approach is neglected, since roll and pitch dynamics of the vehicle are neglected. In [4], Ferretti and Girelli assume a uniform ground pressure distribution and apply equal normal forces at the lowest ends of the sprocket and idler. In the discrete model, no assumption is made of the ground pressure distribution under the track.

The ground normal force acting on each element is computed using a contact model provided in the ADAMS environment. The normal force is applied at the origin of the wheel's reference frame. Ferretti and Girelli apply an external resistive force at the lowest end of the idler pitch circle. In the discrete model, the external resistive force is applied at the origin of the sprocket's reference frame.

Model Based Parameters

Description	Parameter	Section
cohesive modulus of terrain deformation	k_c	2.3.1
frictional modulus of terrain deformation	k_ϕ	2.3.1
exponent of terrain deformation	n	2.3.1
cohesion	c	2.3.2
angle of internal shearing resistance	ϕ	2.3.2
shear deformation modulus	K	2.3.2
stiffness coefficient for contact model	K_s	3.4.1
damping coefficient for contact model	C	3.4.1
stiffness force exponent for contact model	e	3.4.1
damping ramp-up distance	d	3.4.1
discrete points along track-terrain interface	z_i^*	3.4.2.2
coefficient of internal resistance	b_{int}	3.4.6

Table 3.2: List of Model Based Parameters

Computational Based Parameters

Description	Parameter	Section
parameter to compute z_i^*	ΔV_z	3.4.2.2
STEP5 parameters to compute long. shear disp.	$x_{0_{jz}}, x_{1_{jz}}$	3.4.2.3
STEP5 parameters to compute long. force	$x_{0_{fz}}, x_{1_{fz}}$	3.4.3.2
STEP5 parameters to compute lat. shear disp.	$x_{0_{jx}}, x_{1_{jx}}$	3.4.4.3
STEP5 parameters to compute lat. force	$x_{0_{fx}}, x_{1_{fx}}$	3.4.5.2
STEP5 parameters to compute motion resistance	$x_{0_{Rc}}, x_{1_{Rc}}$	3.4.6

Table 3.3: List of Computational Based Parameters

Chapter 4

Modeling and Testing of Power System and Description of Field Test Experiments

4.1 Introduction

There are two main subjects presented in this chapter. The first subject entails the power system used to drive the robotic tracked vehicle, in which a description of the baseline model of the power system is given. The limiting assumptions made in deriving the state equations for the power system model are given, along with a discussion of the implementation of the model into ADAMS. Values for certain parameters used in the power system model were estimated from experimental tests on the actual vehicle. Thus, a discussion of the experimental procedure for estimating the values for these parameters will be presented. Finally, the power system model is validated by comparing simulated results with those obtained from experimental tests of the actual power system of the vehicle.

In the previous chapter, the discrete approach was presented for modeling

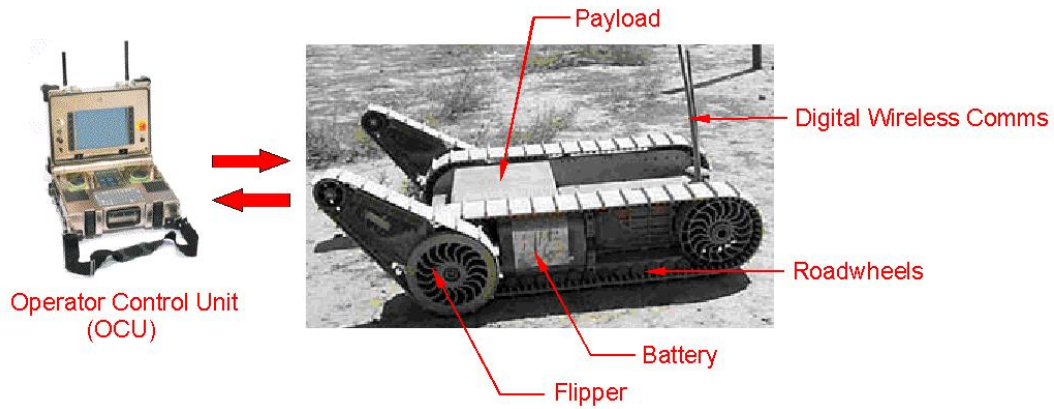


Figure 4.1: PackBot System

the track-terrain interaction for a multi-body dynamics model of a robotic tracked vehicle. The discrete approach provided a simple model for track-terrain interaction, facilitating computationally efficient estimates of the mobility performance of the vehicle on deformable terrain. To evaluate the effectiveness of the discrete approach, comparisons are made between simulated results and those obtained from field-testing of a remotely-operated unmanned tracked vehicle which is to be discussed in the next chapter. Thus, the second major subject presented in this chapter discusses the field tests conducted on the actual robotic tracked vehicle. Descriptions of the metrics measured and the instruments used to measure them in the field tests will be given.

4.2 Physical Description of Actual Robotic Tracked Vehicle

A photograph of the robotic test vehicle is shown in Figure 4.1. The remotely-operated unmanned tracked vehicle, known as the PackBot, was developed by the iRobot Corporation under DARPA's Tactical Mobile Robotics program in 1997 to provide reconnaissance and manipulation of a remote environment while the operator remains safe. The PackBot was designed to maneuver across both urban

and wilderness environments and has recently seen operational use at the World Trade Center and in tactical military operations in both Afghanistan and Iraq. In particular, the PackBot was designed with considerations for impact resistance, waterproofing, vibration resistance, electromagnetic resistance, low electromagnetic signature, and a wide operation temperature range [11]. Depending on the payload, the PackBot can weigh in excess of 45 lb, and can achieve speeds in excess of 8 mph. The geometric dimensions of the PackBot are given in Appendix A.

The mobility of the vehicle derives from a combination of “standard” tracks, front-mounted articulator flippers, and a dual-motor drive system. The tracks are made from Santoprene ®, which is a high-performance elastomer having high tear strength, high resistance to fatigue, good flexibility, low compression set, and a process ease of thermoplastics. The tracks are 3 in wide and have grousers with a height of approximately 5/16 in. The articulator flippers are used to assist the PackBot to maneuver over various obstacles and can be used to flip the entire platform over should it become inverted. The PackBot can also be fitted with extra treads at the rear of the vehicle for additional mobility. Since the tracked vehicle model presented in this work is only concerned with motions over level terrain, the flippers were not included in this model.

The operation of the PackBot is controlled by the Operator Control Unit (OCU), in which a single 802.11 digital link is required to transmit information between the OCU and the PackBot [26]. This link carries real-time digital video stream as well as the status of other information. The PackBot can be equipped with various sensors including: a differential GPS system, compass, roll sensor, tilt sensor, 3-axis accelerometers, cameras, infrared sensors, and thermal sensors. The information from these sensors are sent to the OCU increasing situational awareness by providing the operator with additional information on the PackBot’s status and position.

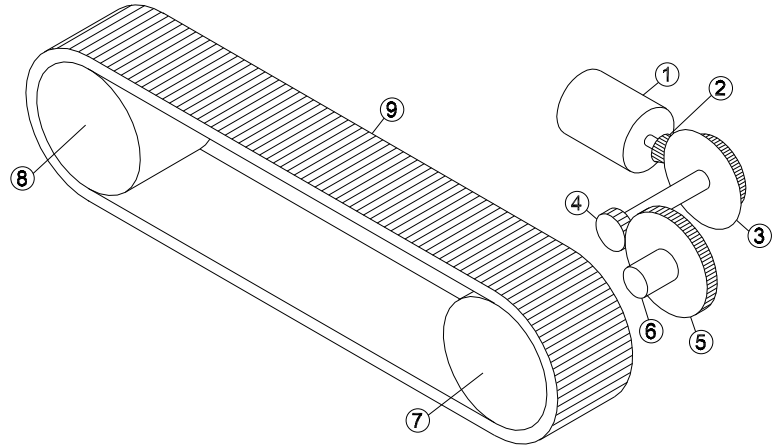
4.3 Motor and Drive Train Model

This section presents the motor and drive train model used to drive the vehicle model presented in Chapter 3. The baseline equations used to model the motor and drive train system are presented and a discussion is given about the implementation of these baseline equations into ADAMS. Also, descriptions of the experimental tests conducted both to estimate values of certain parameters and to validate the motor and drive train model are given.

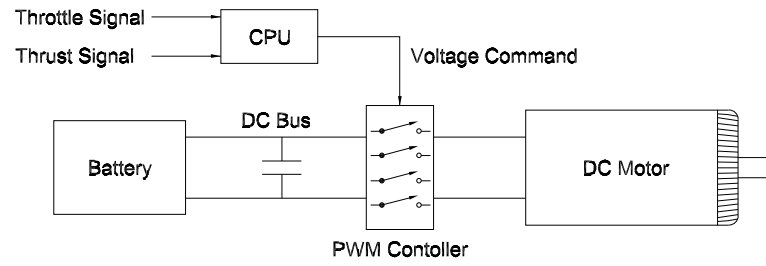
4.3.1 Description of Motor and Drive Train Model

The vehicle is driven using dual brushed permanent magnet DC motors that apply a torque to the sprocket of their respective track through a drive train as shown in Figure 4.2(a). The speed of each motor is controlled by a throttle and steer signal sent from the OCU to the PackBot's onboard computer system, which produces a voltage command for the motor. A battery supplies a voltage to a dc bus, which in turn powers a pulse-width-modulated (PWM) controller as illustrated in Figure 4.2(b). The PWM controller amplifies the voltage supplied by the dc bus to attain the command voltage. Since the focus of this study is on the motion analysis of a tracked vehicle, models for the battery, dc bus, and the PWM controllers are not included. Hence, the voltages supplied to the motors are assumed to be the ideal amplified voltages produced by the PWM controllers.

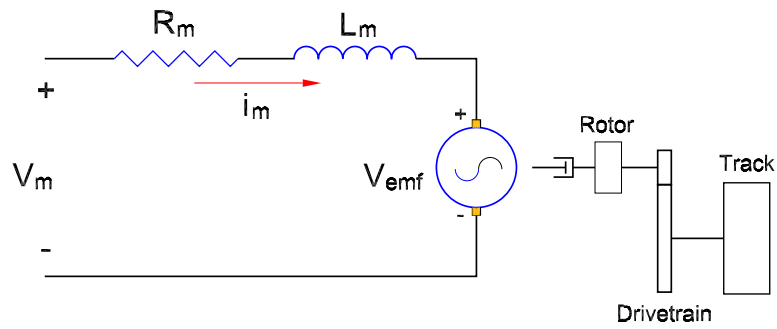
A circuit diagram of the motor and drive train model is shown in Figure 4.2(c). The DC motor armature current is modeled to include the terminal inductance and resistance of the motor, labeled L_m and R_m , respectively. When a voltage V_m is applied to the motor terminals, current flows through the armature windings inducing a magnetic field. This magnetic field tends to align itself with the orientation of the magnetic field of the permanent magnets, which develops a torque on the armature causing it to rotate. As the armature rotates, an induced voltage V_{emf} is



(a) Drive Train Components: 1-motor, 2-bevel pinion, 3-bevel gear, 4-wheel driven pinion, 5-wheel driven gear, 6-wheel hub, 7-sprocket, 8-idler, 9-belt



(b) Power System Used to Drive the PackBot



(c) Circuit Diagram of Motor and Drive Train Model

Figure 4.2: Illustration of Power System Components and Model

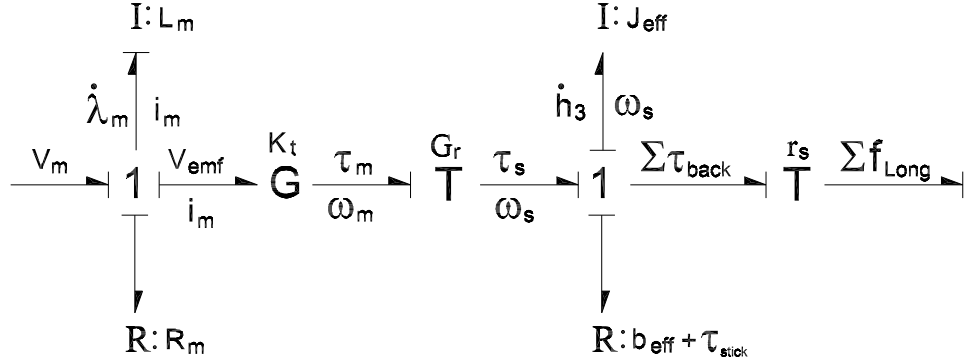


Figure 4.3: Reduced Bond Graph of Motor and Drive Train Model

developed, which has a polarity opposite that of the input motor voltage V_m .

The state equations for the motor and drive train model were derived (see Appendix B) using the bond graph approach. Figure 4.3 shows the reduced bond graph of the motor and drive train system. The model represents a second order system with the states of the system being chosen as the angular velocity of the sprocket ω_s and the current going to the DC motor i_m . The first state equation comes from the rate-of-change of momentum of the sprocket and is given by,

$$\dot{h}_3 = J_{eff} \frac{d\omega_s}{dt} = G_r K_t i_m - b_{eff} \omega_s - b_{int} \omega_s - SIGN(\omega_s) \tau_{stick} - \sum_{i=1}^N \tau_{Back_i}. \quad (4.1)$$

Notice that a single inertia J_{eff} is defined in equation 4.1. This inertia is the effective rotational inertia of the motor, drive train, and track system, “felt” at the sprocket. In other words, the rotational inertias of the components illustrated in Figure 4.2(a) are lumped to the inertia of the sprocket. The effective inertia J_{eff} is evenly distributed to each wheel of the track model (see Section 3.2) so that each wheel has a rotational inertia of J_{eff}/N .

The terms on the right-hand-side of equation 4.1 represent torques. The following gives a detailed description of each torque term in equation 4.1 and an

explanation of how it was defined in ADAMS the ADAMS simulation environment.

$J_{eff} \frac{d\omega_s}{dt}$: The effective rate-of-change of the angular momentum of the sprocket, where J_{eff} is the effective inertia “observed” at the sprocket and ω_s is the angular velocity of the sprocket.

$GR K_t i_m$: Torque applied by the motor and drive train system to the sprocket, where GR is the overall gain of the drive train, K_t is the motor torque constant and i_m is the current flowing through the motor. This torque is directly applied to the sprocket in ADAMS.

$b_{eff} \omega_s$: The effective rotational losses due to friction “observed” at the sprocket. The rotational damping losses of the motor, drive train, and track system are lumped to the losses in the sprocket. The parameter b_{eff} is the effective damping coefficient. This damping torque is directly applied to the sprocket in ADAMS.

$b_{int} \omega_s$: The resistive torque modeling the internal resistance of the track due to factors such as: frictional losses between the driving sprocket teeth and track, in the roadwheel bearings, and the rolling resistance of the roadwheels on the track (see Section 3.4.6).

$SIGN(\omega_s) \tau_{stick}$: The effective stiction “observed” at the sprocket. Notice that the discontinuous SIGN function is used in defining the orientation of the stiction torque. As in Chapter 3, the continuous STEP5 function is used in place of the SIGN function to provide a numerically smooth model. The stiction torque is directly applied to the sprocket.

$\sum_{i=1}^N \tau_{Back_i}$: Total back-torque due to the longitudinal forces developed due to the longitudinal shearing of the terrain (see Section 3.4.3.1).

The second state equation comes from the rate-of-change of the flux linkage of the motor and is given by,

$$L_m \frac{di_m}{dt} = V_m - R_m i_m - K_v G_r \omega_s. \quad (4.2)$$

Equation 4.2 is explicitly defined in ADAMS using the differential equation functionality. The following gives a detailed description of each term given in equation 4.2.

$L_m \frac{di_m}{dt}$: The rate-of-change of the flux linkage, where L_m is the inductance and i_m is the current going to the motor.

V_m : Voltage supplied to the motor.

$R_m i_m$: Voltage drop due to the resistance of the coils, where R_m is the resistance of the coils.

$K_v G_r \omega_s$: Back emf due to the rotation speed of the rotor, $\omega_m = G_r \omega_s$, where K_v is the speed constant of the motor.

The nominal values for the motor parameters L_m, R_m, K_t, K_v and the value of the motor inertia J_m were obtained from a specifications available from the manufacturer of the motor, Maxon Precision Motors Inc. Also, the geometric and mass properties of the motor, drive train, and track system were obtained from a CAD model provided by PackBot manufacture, iRobot Corporation. All of these values are given in Appendix B. The only values that were not provided or attainable analytically were for the friction parameters b_{eff} and τ_{stick} . Therefore, a series of experimental tests were conducted on the PackBot to obtain data so that the values for the friction parameters could be estimated.

4.3.2 Experimental Motor and Drive Train Tests

If a constant torque is applied to the sprocket of the track, the rotational dynamics of the motor, drive train, and track system will reach steady-state operation after a short period of time (neglecting track-terrain interaction). Mathematically, this scenario may be captured by reducing equation 4.1 to

$$\begin{aligned}
 \overset{=0}{J_{eff}} \frac{d\omega_s}{dt} &= G_r K_t i_{m_{steady}} - b_{eff} \omega_{s_{steady}} - \tau_{stick} - \overset{=0}{b_{int}} \omega_s - \sum_{i=1}^N \overset{=0}{\tau_{Back_i}}, \\
 0 &= \tau_{steady} - b_{eff} \omega_{s_{steady}} - \tau_{stick},
 \end{aligned} \tag{4.3}$$

where the steady-state torque applied to the sprocket by the motor and drive train system, τ_{steady} , is defined as

$$\tau_{steady} \equiv G_r K_t i_{m_{steady}}, \tag{4.4}$$

where G_r is the overall gain of the drivetrain, K_t is the torque constant of the motor, and $i_{m_{steady}}$ is the steady-state motor current. Solving for τ_{steady} in equation 4.3 yields

$$\tau_{steady} = b_{eff} \omega_{s_{steady}} + \tau_{stick}. \tag{4.5}$$

Equation 4.5 shows that at steady-state operation, the torque applied to the sprocket balances the resistive torques caused by friction. This steady-state model also implies that the steady-state torque τ_{steady} is linearly related to the steady-state angular velocity of the sprocket $\omega_{s_{steady}}$, where the slope and intercept of the line are b_{eff} and τ_{stick} , respectively. If several operating points $(\omega_{s_{steady}}, \tau_{steady})$ are given, then the friction parameters b_{eff} and τ_{stick} may be estimated using linear regression analysis.

Therefore, experimental tests were conducted on the PackBot to measure

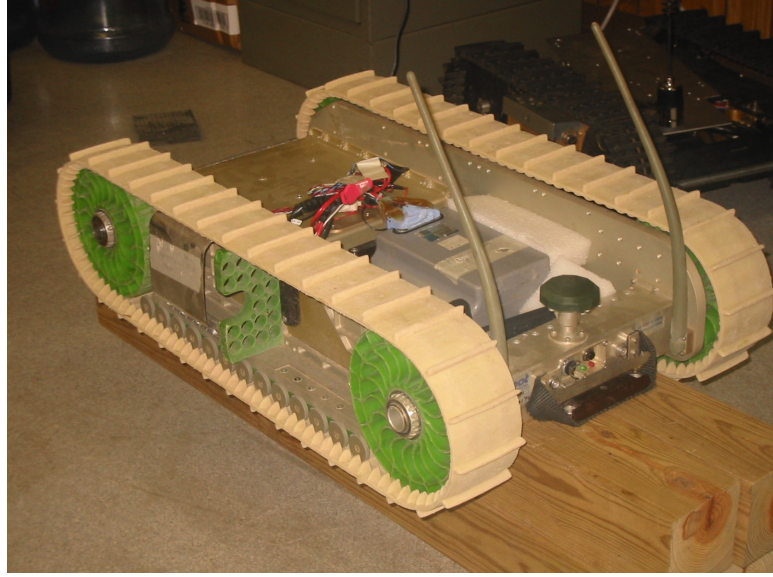


Figure 4.4: Experimental Tests Conducted to Obtain Unknown Friction Parameters

various operating points $(\omega_{steady}, \tau_{steady})$. First, the PackBot was elevated (see Figure 4.4) so that no external loads by the ground were applied to the track. Next a constant torque was applied to the sprocket of the track, in which the sprocket was then allowed to reach a steady-state angular velocity. An encoder on the PackBot was used to measure the angular velocity of the sprocket, but there was no sensor available to directly measure the torque applied to the sprocket. However, there was a sensor on the PackBot that measured the motor current. Ideally, the torque applied to the sprocket by the motor and drive train system may be computed by equation 4.4. Thus, τ_{steady} was estimated by using equation 4.4 and the measured motor current $i_{m_{steady}}$. Figure 4.5 shows the measured results for a particular experiment. The first plot shows the measured motor current. Notice that the current has a high degree of oscillation. This “noise” is partially caused both by the on-off contact of the brushes used to mechanically control the orientation of the rotor magnetic field and of the fast switching of the PWM controller used to amplify the voltage supplied from the dc bus. Therefore, the steady-state current $i_{m_{steady}}$ was estimated by taking an average value over the time interval of steady-state operation, shown by the dashed (red) boxes in Figure 4.5.

Various operating points $(\omega_{steady}, \tau_{steady})$ were recorded. This process was

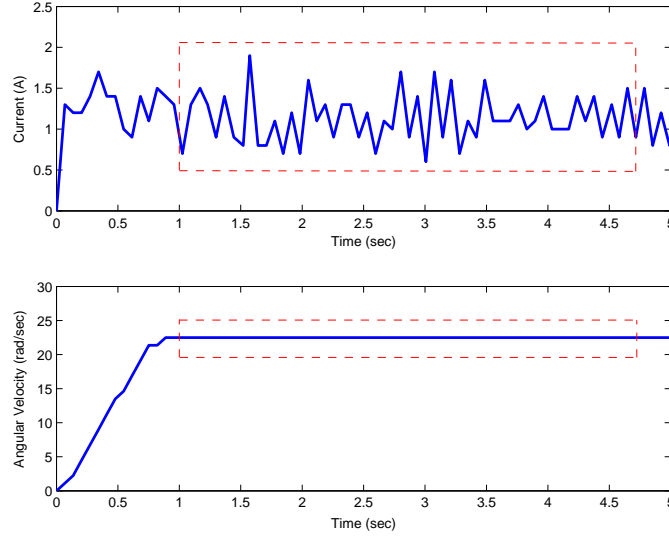


Figure 4.5: Estimating the Steady State Torque

done for both the left and right sprocket of the vehicle. The data is plotted in Figure 4.6. Regression analysis was used to determine the slope and intercept of the line. Notice from the figure that two different linear profiles for the left and right sprockets were obtained. An average of the two lines was used to determine the frictional parameters used for both drives. Table 4.1 shows the values of the friction parameters obtained from the measured data. Also given in the table is the sample

Parameter	Right Sprocket	Left Sprocket	Average
b_{eff} (kg m/s)	0.02428	0.024162	0.024221
τ_{stick} (Nm)	0.58837	0.54915	0.56876
r^2 -value	0.9951	0.9925	0.9925

Table 4.1: Estimated Values for Friction Parameters

coefficient of determination r^2 which expresses the proportion of the total variation in the values of τ_{steady} that can be accounted for or explained by a linear relationship with the values of ω_{steady} . Notice that the r^2 -values for the data are close to one, which indicates that it is reasonable to model the rotational frictional losses within

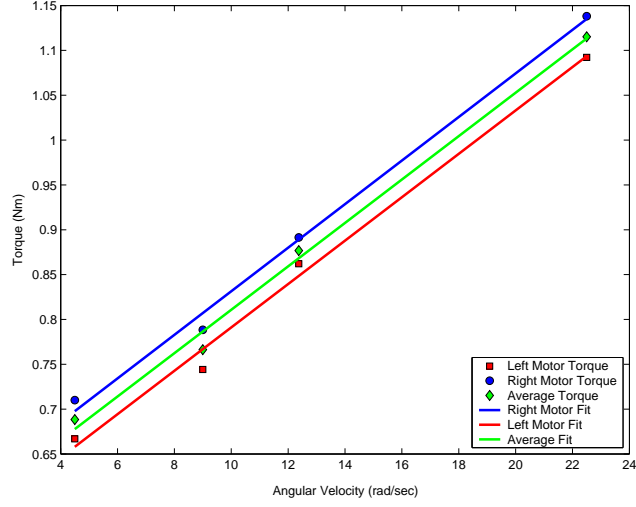


Figure 4.6: Results of Experimental Tests to Estimate the Values for the Friction Parameters b_{eff} and τ_{stick}

the motor and drive train system using a linear torque-speed relationship.

4.3.3 Verifying Motor and Drive Train Model

Once the friction parameters b_{eff} and τ_{stick} were obtained, the motor/drive-train model could be simulated. The model was validated by comparing the simulation results with those obtained from the experimental tests conducted to estimate the values for the friction parameters. Recall, the input to the model is the voltage supplied to the motor. Unfortunately, however, this metric could not be measured and therefore, the profile of the voltage had to be assumed. In the experiments, the speed of the motors were controlled using the joystick on the operator control unit (OCU). Figure 4.7 shows how the voltage profile was determined. The voltage supplied to the motor was given the following profile,

$$V_m = \begin{cases} V_{m_{trans}} t & \text{if } t < t_{steady} \\ V_{m_{steady}} & \text{otherwise} \end{cases},$$

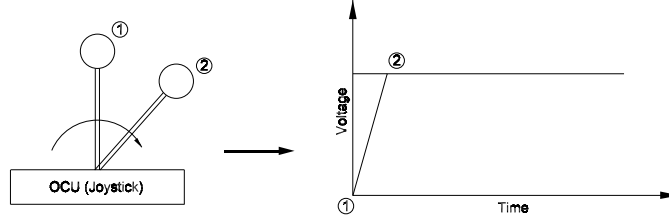


Figure 4.7: Input Motor Voltage Profile

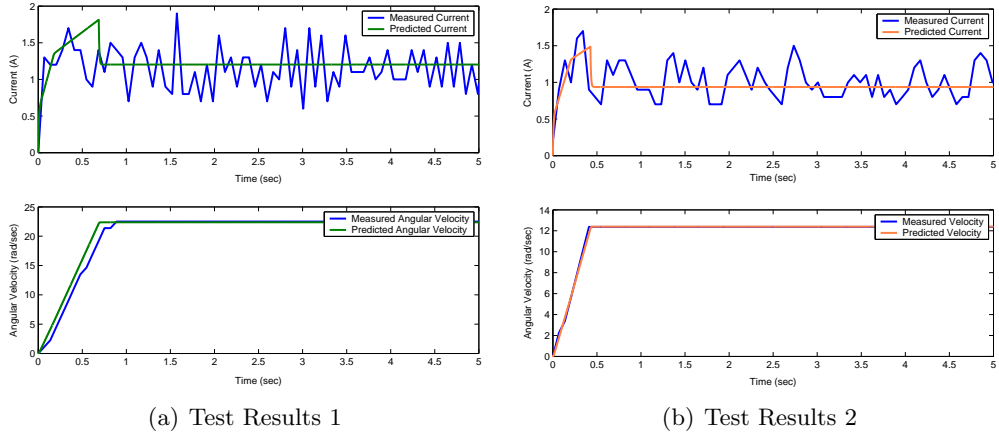


Figure 4.8: Comparisons of Motor and Drive Train Simulation Results and Experimental Results

where the transient component of the voltage is linearly related to time, $V_{m_{trans}}t$, and after a certain time t_{steady} the voltage is given as a constant value $V_{m_{steady}}$. Using this voltage profile, the system was simulated in ADAMS. The simulated results are plotted with the measured results for two different tests in Figure 4.8. The results for the first test are shown in Figure 4.8(a), in which $\omega_{s_{steady}} = 22.5 \text{ rad/sec}$. The first plot in Figure 4.8(a) shows a comparison of the simulated and measured motor current. Notice that the predicted motor current appears to be the average value of the measured current at steady-state operation. The bottom plot in Figure 4.8(a) shows a comparison of the predicted and measured angular velocity of the sprocket, in which the results are consistent. The results for the second test are shown in

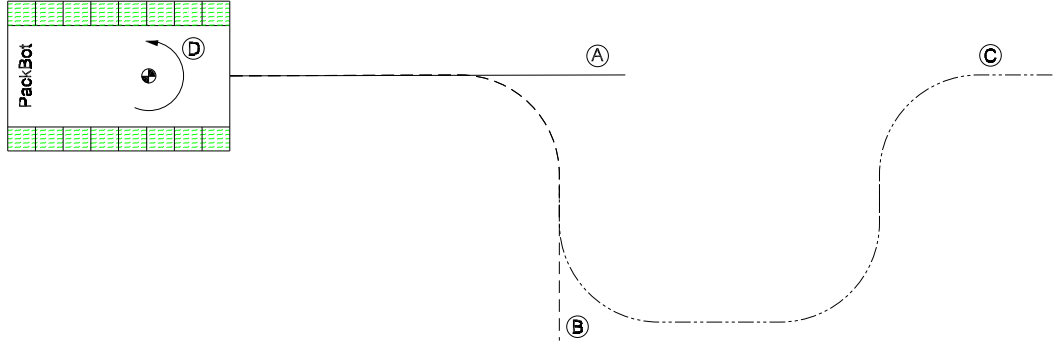


Figure 4.9: Various Maneuvers Performed to Verify Vehicle Model

Figure 4.8(b), in which $\omega_{steady} = 12.4 \text{ rad/sec}$. Notice the simulated results match very well with the measured results.

4.4 Field Test Experiments

In order to validate the model, experimental tests were conducted on the PackBot. The tests consisted of subjecting the vehicle to four different types of maneuvers on various terrains. The four maneuvers are illustrated in Figure 4.9, in which maneuver *A* is a go-stop, *B* is a j-turn, *C* is a double lane-change maneuver, and *D* is a zero radius turn maneuver. The experimental test was conducted on various terrains, but only two of the terrains had some kind of nominal values provided in literature for the parameters describing their pressure-sinkage and shear stress-shear displacement relationships. The two terrains were dry sand and asphalt (see Figure 4.10), which have distinct response properties. Dry sand can be modeled as a deformable terrain, where asphalt is considered to be non-deformable.

As mentioned earlier, the PackBot is equipped with various sensors. Unfortunately, only a few sensors on the PackBot were logged for this testing. The sensors available monitored:



(a) Dry Sand



(b) Asphalt

Figure 4.10: Terrains Used to Conduct Maneuver Tests

1. Ideal forward speed of the vehicle (from sprocket encoders)
2. Yaw rate of the vehicle
3. Currents through both motors

Ideally, to truly validate the model presented in Chapter 3 additional sensors would be needed to prove that the forces acting on the vehicle due to the shearing of the terrain are accurate. Therefore, the idea was to observe how the system behaves for the various maneuvers and check to see how close the simulation results match with the measured data. This will give some validation to conduct future experiments.

Since the input to the model could not be measured, the motor voltages had to be estimated. This was accomplished by matching simulated motor currents to measured currents. Based on these profiles, the voltage profiles were estimated. Once the currents had been matched, the forward velocity and the yaw rate were evaluated to determine how well they corresponded to measured values without making any other changes.

In all, this work shows if the kinematic motion of the vehicle is consistent with the operation of the motor model. It is important to keep in mind that ‘nominal’ data for the various terrains was used for the track-terrain interaction model.

4.5 Conclusion

A physical description of the robotic tracked vehicle has been given. The motor and drive train model used to drive the vehicle has been presented, which was validated by comparing experimental results with those obtained from simulation results using the motor and drive train model.

Also presented were the field tests conducted on the robotic tracked vehicle, in which a description was given of the maneuvers performed, type of terrain, and the metrics recorded. The results of these field tests will be used in the next chapter to validate the vehicle model presented in Chapter 3.

Chapter 5

Simulation Results and Discussion

5.1 Introduction

This chapter presents simulation results obtained from the robotic tracked vehicle model presented in chapters 3 and 4. The results are compared to those from field tests to verify the effectiveness of the vehicle model and to identify any issues that need attention. Finally, the results from parametric studies are presented to identify and highlight the sensitivity of the response of the vehicle model to perturbations in the terrain parameters c , ϕ , and K .

5.2 Simulation Environment in ADAMS

Figure 5.1 shows a picture of the solid model representation in ADAMS. There are several toolboxes provided in ADAMS to aid in the modeling and simulation process. The main tool box is used to create forces, constraints, and to control the model view options. The simulation solver options can be set to select simulation step size,

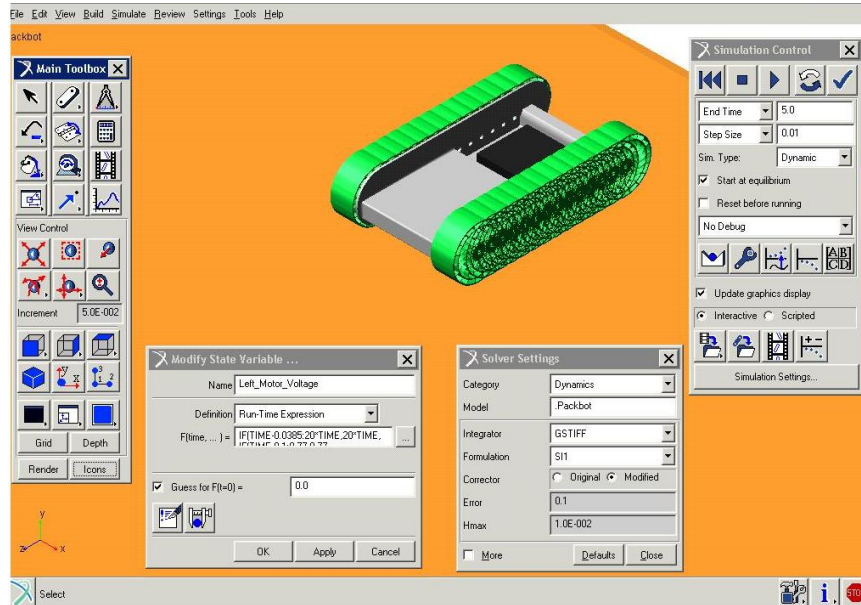


Figure 5.1: ADAMS Modeling and Simulation Environment

solver algorithms methods, and parameters such as error tolerances. The following solver settings were used for the simulations in this thesis¹.

Integrating solver: Gear Stiff - The Gear Stiff integrator (GSTIFF) uses a backwards differentiation formula to integrate differential and algebraic, standard index-three equations. It, assumes a fixed time step which results in fixed coefficients for predictions and provides good solutions for simulations of stiff models (models with a mix of high and low frequencies).

Equation Formulation: I3 - Is fast and ensures that the solution satisfied all constraints. Does not ensure that the velocities and accelerations calculated satisfy all first- and second-time derivatives. Monitors integration error only in system displacements, not in velocities.

Corrector: Original - Requires that at convergence, the error in all solution vari-

¹See ADAMS/VIEW Reference Manual

ables be less than the corrector error tolerance.

Error tolerance: 0.001 - Specifies the relative and absolute local integration error tolerances that the integrator must satisfy at each step.

Simulation time step: 0.01 - Represents the amount of time, in current model units, between output steps.

5.3 Simulation Results and Comparisons

This section presents comparisons of simulation results with those obtained from field tests of the PackBot. The tests were conducted on dry sand and asphalt. The nominal values for the characteristic parameters of the two terrains used in the simulations are reported in Table 5.1 [1] and Table 5.2 [11]. The value of K for asphalt is tuned and will be explained later on in the section. Notice that the pressure-sinkage parameters n , k_c , k_ϕ in Table 5.2 are not relevant, since asphalt is modeled as a non-deformable terrain.

In Chapter 3, the internal resistive losses of the track are modeled as a linear viscous torque. This introduces the damping coefficient b_{int} , whose value may depend on the type of terrain and the design of the track. In this model, the value of b_{int} can be estimated by tuning the model. Once the value of b_{int} is estimated for a given terrain, it is used for the rest of the simulations on that terrain. The estimated

c (kPa)	ϕ (deg)	K (m)	n (-)	k_c (kN/m ^{$n+1$})	k_ϕ (kN/m ^{$n+2$})
1.04	28	0.0254	1.1	0.99	1528

Table 5.1: Nominal Terrain Parameters for Dry Sand

c (kPa)	ϕ (deg)	K (m)	n (-)	k_c (kN/m ^{$n+1$})	k_ϕ (kN/m ^{$n+2$})
0	36.55	0.009	-	-	-

Table 5.2: Nominal Terrain Parameters for Asphalt

	Dry Sand	Asphalt
$b_{int} (kg\ m^2/s)$	0.076	0.06

Table 5.3: Estimated Values for Internal Track Damping Coefficient on Dry Sand and Asphalt

values for b_{int} on dry sand and asphalt are reported in Table 5.3. The process of tuning for the value of b_{int} is described in the following subsection.

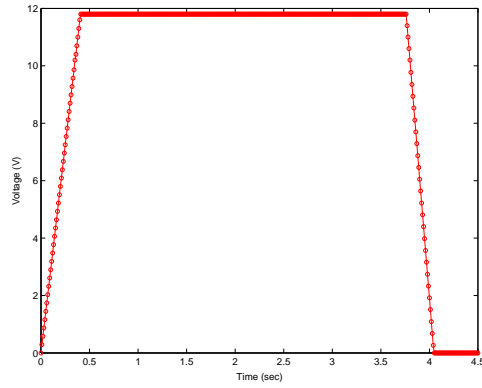
It must be emphasized that the simulated input motor voltages are estimated by matching simulated currents with the motor currents logged during the respective test. Once the measured and simulated currents are sufficiently matched, ideal speeds and yaw rates are compared *without* making any additional parameter changes to the model. Also, the ideal speed v_i is computed as,

$$v_i = \frac{\omega_{rs} + \omega_{ls}}{2} r_s, \quad (5.1)$$

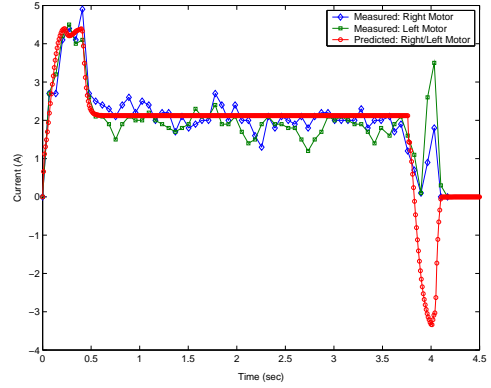
where ω_{rs} and ω_{ls} are the angular velocity of the right and left sprocket, respectively, and r_s is the sprocket radius. Finally, it must be mentioned that the amp-meter used to monitor the motor currents provides absolute values.

5.3.1 Go-Stop Maneuver

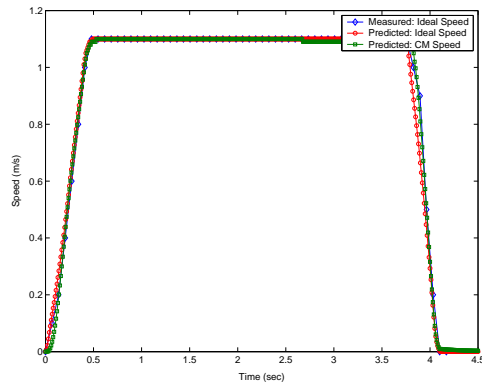
The first maneuver is the go-stop maneuver. Torques are applied to both sprockets and then suddenly removed, causing the vehicle to essentially brake and come to a complete stop after moving along a straight line. Figure 5.2 shows a comparison of the simulation results with those obtained from field tests on dry sand. Figure 5.2(a) shows the input motor voltages as they vary with time. Figure 5.2(b) shows the currents in the right and left motors. Notice that the currents initially rise rapidly (in-rush) and then drop to a steady-state value. This can be explained by looking at the second state equation, 4.2, used to model the electrical part for the track and



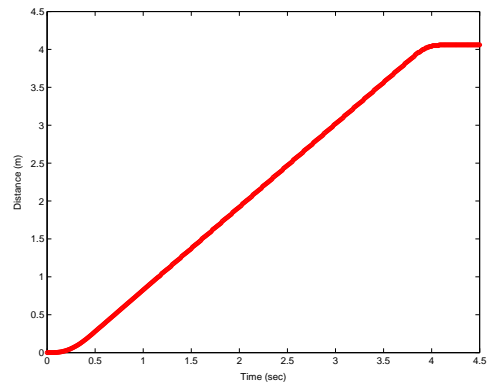
(a) Predicted Motor Voltages



(b) Motor Currents



(c) Speeds



(d) Predicted Distance Traveled

Figure 5.2: Comparisons of Simulation Results and Field Test Results for Go-Stop Maneuver on Dry Sand

motor/drivetrain system,

$$L_m \frac{di_m}{dt} = V_m - R_m i_m - K_v G_r \omega_s,$$

in which the dominant terms on the right-hand-side are the motor voltage, V_m , and the back emf, $K_v G_r \omega_s$. As the motor voltage V_m begins to increase, the current rises because the angular velocity of the sprocket is barely starting to move. In other words, the transient of V_m is faster than the response of the mechanical state ω_s . As the input voltage levels off, the angular velocity of the sprocket increases until reaching steady-state. This induces a back emf that opposes the applied voltage, so the current drops sharply to a steady-state value. At steady-state, the left-hand-side of equation 4.2 is zero so that the terms on the right-hand-side balance out obeying Kirchoff's voltage law.

When the motor voltages are suddenly dropped to zero, the ideal speed of the vehicle $r_s \omega_s$ becomes smaller in magnitude than the actual speed of the vehicle V_v causing longitudinal shear forces to brake the vehicle. The simulated motor currents go negative, while the angular velocities of the motors decline, but remain positive until they approach zero. This implies that the motors are in a generating state of operation. This is due to the same effect discussed previously. The value of the motor voltage drops faster than the value of $K_v G_r \omega_s$, resulting in the value of the right-hand-side of equation 4.2 to be negative.

Figure 5.2(c) compares the simulated and measured ideal speeds, and also shown in the figure is the predicted longitudinal velocity of the center-of-mass (CM) for the vehicle. Finally, Figure 5.2(d) shows the distance traveled by the vehicle in the simulation, which compares well with that observed (but not directly measured) during the test.

As mentioned earlier, the value of the parameter b_{int} must be selected by tuning the model. The following is a process for estimating the value of b_{int} . To

begin, consider only the dominant terms in the state equations, 4.1 and 4.2, used to model the rotational dynamics for the track and motor/drivetrain system. Doing so, we end up with,

$$\begin{aligned}
\cancel{J_{eff}} \overset{=0}{\frac{d\omega_s}{dt}} &\approx G_r K_t i_{m_{steady}} - \cancel{b_{eff}} \overset{\approx 0}{\omega_{s_{steady}}} - \cancel{\tau_{stick}} \overset{\approx 0}{\omega_s} - b_{int} \omega_s - \sum_{i=1}^N \overset{\approx 0}{\tau_{Back_i}} \\
0 &\approx \alpha i_{m_{steady}} - b_{int} \omega_{s_{steady}},
\end{aligned} \tag{5.2}$$

and

$$\begin{aligned}
\cancel{L_m} \overset{=0}{\frac{d\omega_m}{dt}} &\approx V_m - \cancel{R_m} \overset{\approx 0}{\omega_m} - K_v G_r \omega_s \\
0 &\approx V_{m_{steady}} - \alpha \omega_{s_{steady}},
\end{aligned} \tag{5.3}$$

where $\alpha \equiv K_t G_r$ and $K_v G_r$ since $K_t G_r$ and $K_v G_r$ have the same values when consistent units are used. The validity in neglecting certain terms is that the resistive torques $b_{eff} \omega_s$ and τ_{stick} are minor losses. The values for the parameters b_{eff} and τ_{stick} are obtained under no load conditions (Section 4.3.2). At steady-state, the magnitude of the longitudinal forces, which contribute to the total back torque τ_{Back} , are small. The PackBot does not exert enough static pressure on the ground to cause significant sinkage, so the magnitude of the motion resistance is negligible. Thus, the tractive effort the track must produce to overcome the motion resistance is not significant.

Using equations 5.2 and 5.3 to estimate the values of $V_{m_{steady}}$ and b_{int} in terms of $\omega_{s_{steady}}$ and $i_{m_{steady}}$ yields,

$$V_{m_{steady}} \approx \alpha \omega_{s_{steady}}, \tag{5.4}$$

and

$$b_{int} \approx \alpha \frac{i_{m_{steady}}}{\omega_{s_{steady}}}. \quad (5.5)$$

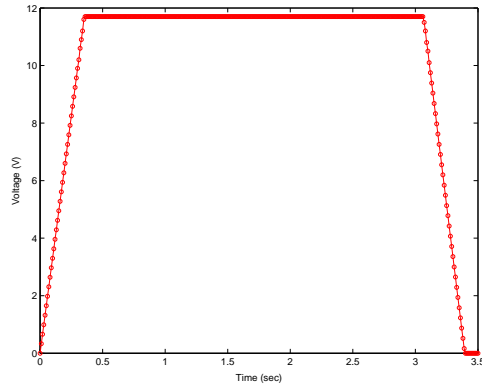
Using experimental data, equations 5.4 and 5.5 can be used as a starting point for finding a value for b_{int} and for $V_{m_{steady}}$. For example, by averaging the currents during the time interval [1-3] seconds, shown in Figure 5.2(b), the value of $i_{m_{steady}}$ can be approximated. Using the ideal speed during the same time interval in Figure 5.2(c), the value of ω_s can be computed. Once the value of b_{int} is estimated it is fixed for all other maneuver simulations on sand.

Figure 5.3 shows a comparison of the simulation results with the experimental results for the go-stop maneuver on asphalt. Notice that similar behaviors are observed on asphalt as those on sand. On asphalt, the tips of the grousers (or cleats) are the only part of the track that come into contact with the ground. Because of this, a modification was made to the value of the sprocket radius r_s used in the vehicle model. The modified radius included the height of the grouser, h_g , so that $r'_s = r_s + h_g$. However, the simulated ideal speed was computed using r_s , since the experimental ideal speed does not take into account the height of the grousers. Figure 5.3(c) shows both the ideal simulated and experimental speeds and the simulated forward speed of the CM of the vehicle. Notice the CM speed is greater than the ideal speeds because of the modified radius.

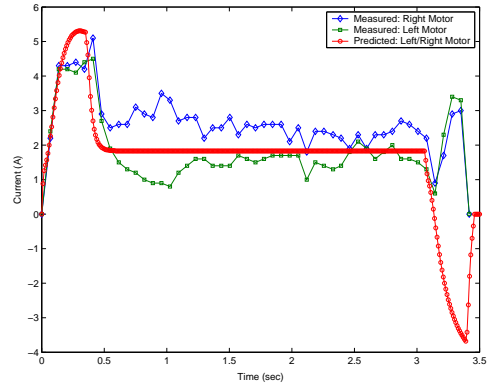
No data was available for the value of shear deformation modulus K on asphalt. Recall in Chapter 2, K is used in the shear stress-shear displacement relationship given by,

$$\tau = (c + \sigma \tan \phi) \left(1 - e^{-j/K}\right), \quad (5.6)$$

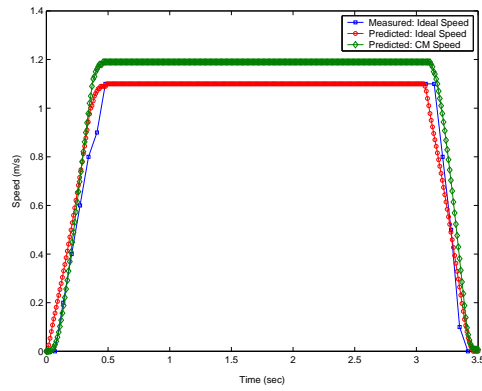
where c and ϕ are characteristic properties of the terrain, σ is normal pressure, and j is shear displacement. The value K affects the sensitivity of the shear stress τ to the shear displacement j . For large values of K it takes a large shear displacement before



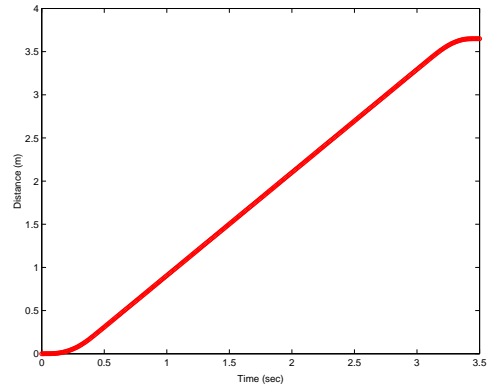
(a) Predicted Motor Voltages



(b) Motor Currents



(c) Speeds



(d) Predicted Distance Traveled

Figure 5.3: Comparisons of Simulation Results and Field Test Results for Go-Stop Maneuver on Asphalt

τ can reach a maximum value. As the value of K becomes smaller the shear stress reaches a maximum almost instantaneously even for small shear displacements. As K approaches zero equation 5.6 reduces to,

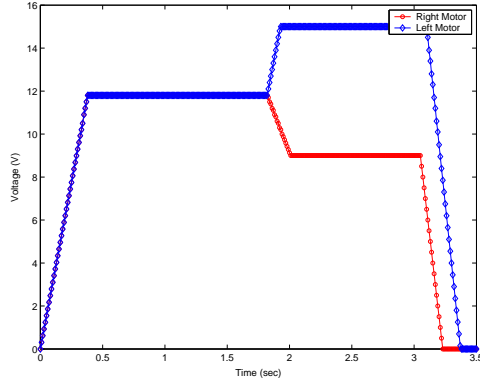
$$\tau = \sigma \tan \phi. \quad (5.7)$$

This implies that the shear stress is modeled similar to Coloumb friction. However, equation 5.7 is discontinuous, which can cause problems for numerical solvers. Therefore, the value of K was tuned to be small, but not exactly zero, so that the continuous equation 5.7 is used. The value of K was selected to be 0.009 m.

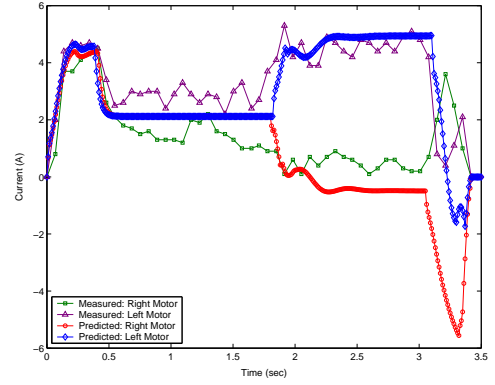
5.3.2 J-turn Maneuver

The second maneuver is a j-turn maneuver. The vehicle is accelerated along a straight path, then the torque applied to the left sprocket is increased, while the torque on the right sprocket is reduced. Note that these torques are generated in the PackBot as a result of operator input. The tractive effort developed by the left track becomes greater than the tractive effort of the right track. This creates a yaw moment causing the vehicle to turn. The torques are then removed causing the vehicle to brake and come to a complete stop. Figure 5.4 shows a comparison of the simulation results to those obtained from the field tests on dry sand. Figure 5.4(a) shows the motor voltage profiles and Figure 5.4(b) shows the resulting motor currents. Notice during the time interval, 2-3 seconds, when the vehicle is turning the value of the simulated right motor current goes negative. Although not explicitly shown, during this same time interval the simulated angular velocity of the right sprocket declines, but remains positive. This implies that the right motor is in a generating state of operation. When both torques are removed, the vehicle brakes and both motors are in a generating state of operation.

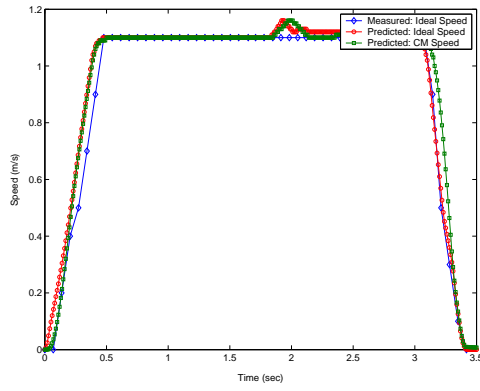
Figure 5.4(c) shows results of the speed predictions, which match well with



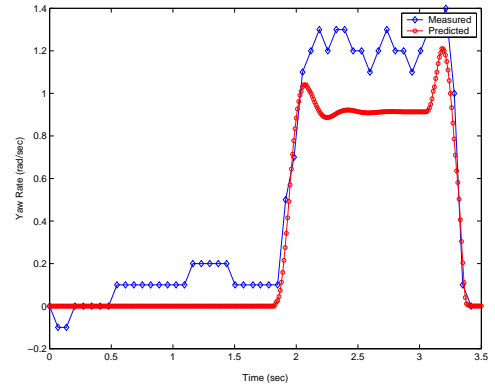
(a) Predicted Motor Voltages



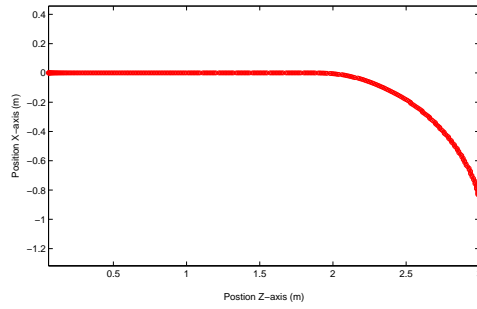
(b) Motor Currents



(c) Speeds



(d) Yaw Rate



(e) Predicted Trajectory of CM of Vehicle

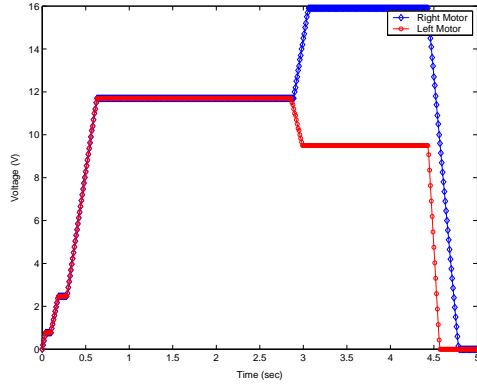
Figure 5.4: Comparisons of Simulation Results and Field Test Results for J-turn Maneuver on Dry Sand

the measured values. Figure 5.4(d) shows a comparison of the yaw rates. The simulated yaw rate is a little under estimated. Recall, the same shear force model (Section 3.2.1) is used to model the lateral forces as the longitudinal forces. It was observed that as the vehicle turns, sand accumulates along the sides of the tracks, particularly at the rear end of the tracks. This occurrence is referred to as the bulldozing effect. The lateral force model given in Section 3.4.5.1 only takes into account the shearing of the terrain and not the bulldozing effect. Yet, the simulated yaw rate is lower than the experimental yaw rate. Thus, it appears that the lateral force model used may over estimate the forces.

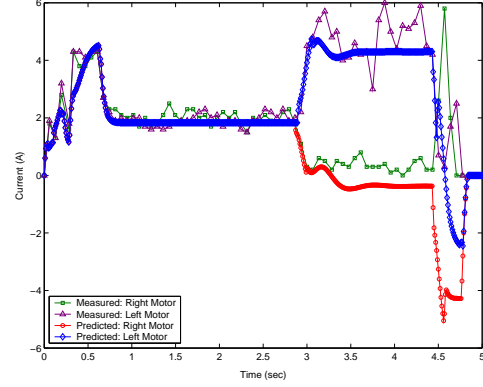
Figure 5.5 summarizes the results for the j-turn maneuver on asphalt. The simulated results appear to match very well with the experimental results. Notice again, that the simulated motor current for the inside track (right) during the turning maneuver is negative, which implies that the right motor is in a generating state of operation.

5.3.3 Double-Lane-Change Maneuver

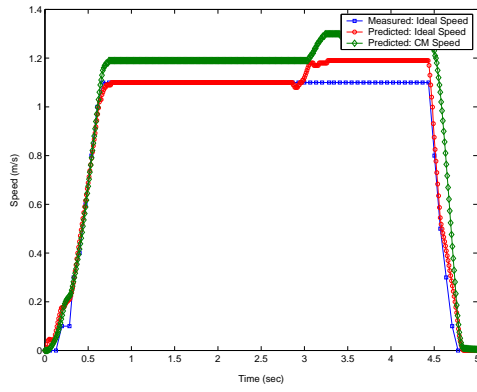
The third maneuver is a double-lane-change maneuver. The vehicle is accelerated to a steady-state velocity along a straight line, then the vehicle is turned to the right and then to the left on to the previous line of motion. The torques are then removed from the sprockets causing the vehicle to brake and come to a complete stop. Figure 5.6 shows a comparison between the simulation results and those obtained from the field tests on dry sand. It should be pointed out that no parameter changes are made for these simulations. The simulation results appear to match very well with the field test results. Notice in Figure 5.6(b) that the value for the simulated motor current for the inner track is negative, which implies that the motor of the inner track is in a generating state of operation. Also, the simulated speeds shown in Figure 5.6(c) fluctuate when the vehicle is turning, while the experimental ideal



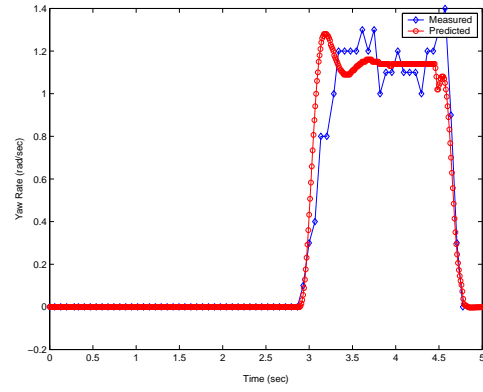
(a) Predicted Motor Voltages



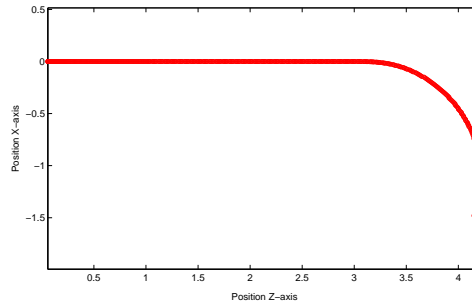
(b) Motor Currents



(c) Speeds

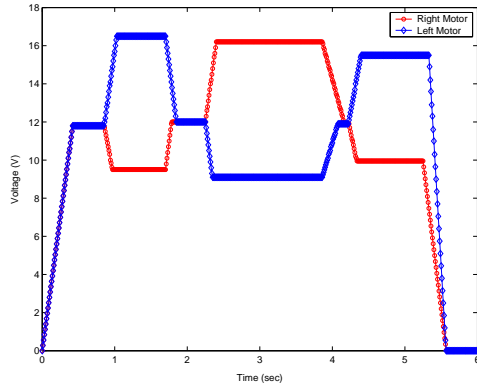


(d) Yaw Rate

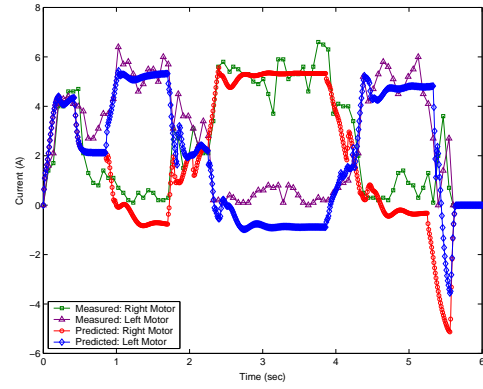


(e) Predicted Trajectory of CM of Vehicle

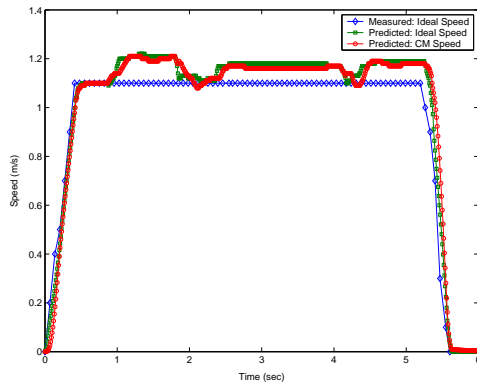
Figure 5.5: Comparisons of Simulation Results and Field Test Results for J-turn Maneuver on Asphalt



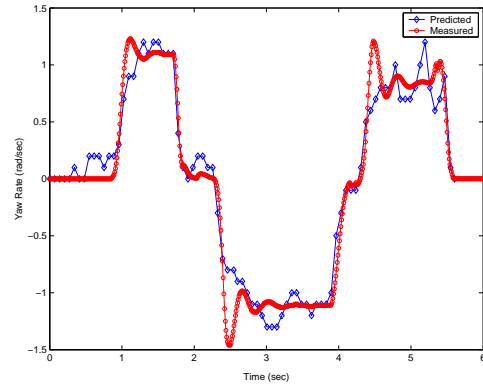
(a) Predicted Motor Voltages



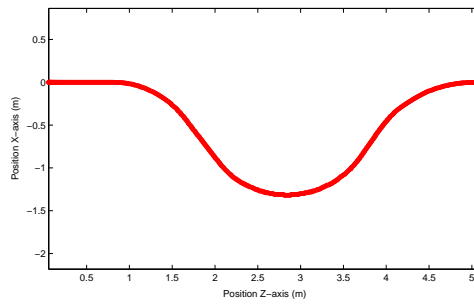
(b) Motor Currents



(c) Speeds



(d) Yaw Rate



(e) Predicted Trajectory of CM of Vehicle

Figure 5.6: Comparisons of Simulation Results and Field Test Results for Double-Lane-Change Maneuver on Dry Sand

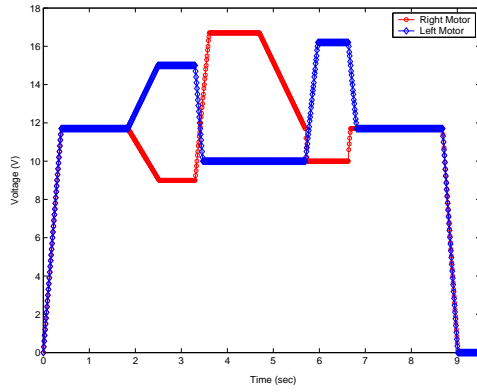
speed remains constant. This is partially due to the encoder used to measure the speed of the motor. The encoder averages pulses over a period of time. Depending on the sampling rate, the encoder may not detect the small fluctuation in speed.

The simulated yaw rate shown in Figure 5.6(d) matches well with the measured yaw rate. This appears to match better than the yaw rate in the j-turn maneuver shown in Figure 5.4(d). Again, however, the lateral force model in this work only takes into account the shearing of the terrain and not the bulldozing effect, which is observed when the vehicle is turning during the field tests. It appears that the lateral force model in Section 3.4.5.1. overestimates the lateral force, but is compensated for by the bulldozing effect. The trajectory of the CM of the vehicle is shown in Figure 5.6(e), which matches well with the path observed during the field test.

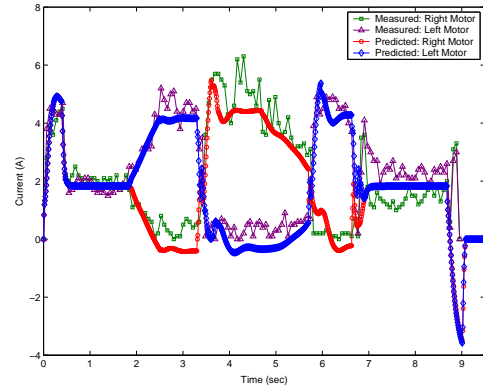
Figure 5.7 shows a comparison of the simulated results to those obtained from the field tests on asphalt. The simulation results match well with the experimental results.

5.3.4 Zero Radius Turn Maneuver

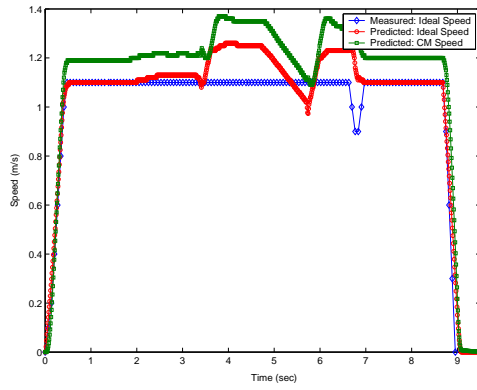
The last maneuver for comparison is a zero radius turn. Equal and opposite torques are applied to the left and right sprocket. Figure 5.8 shows a comparison of the simulation results to the field test conducted on dry sand. Notice that the simulation results do not match very well with the field test results. The simulated yaw rate is nearly eleven times greater than the experimental yaw rate. This can be explained by the observed sinkage of the vehicle. As the vehicle rotates, sand is displaced away from the vehicle causing the vehicle to sink. This phenomenon is often referred to as slip sinkage. As the vehicle sinks, the sides of the track must push against the accumulating soil, which constitutes the bulldozing effect. It was observed that the sinkage of the vehicle was anywhere from two to three inches. In fact, after



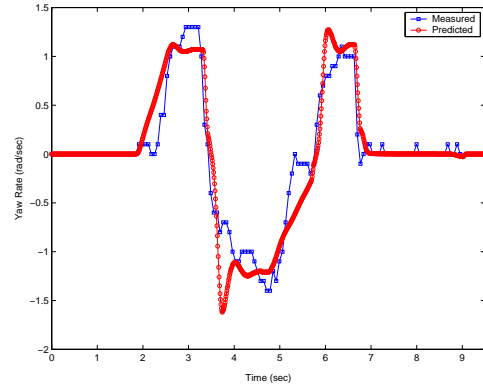
(a) Predicted Motor Voltages



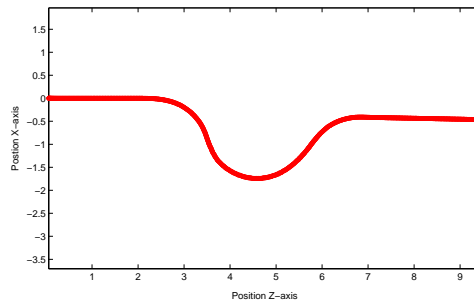
(b) Motor Currents



(c) Speeds

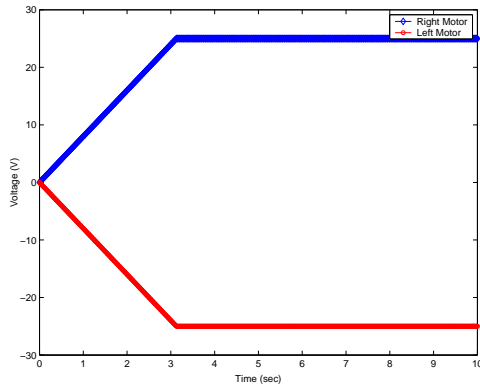


(d) Yaw Rate

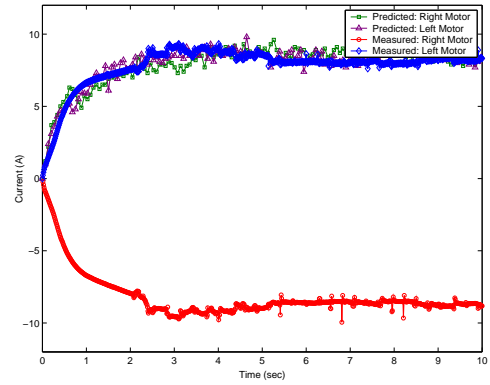


(e) Predicted Trajectory of CM of Vehicle

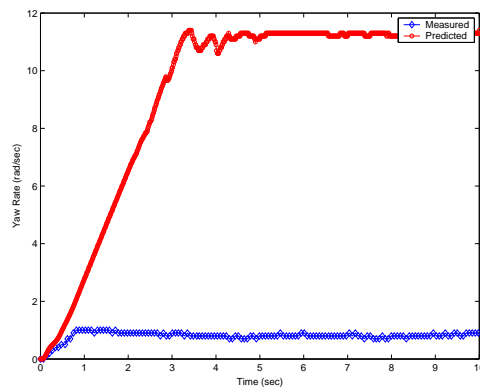
Figure 5.7: Comparisons of Simulation Results and Field Test Results for Double-Lane-Change Maneuver on Asphalt



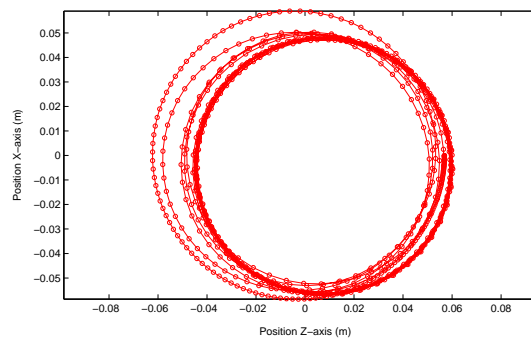
(a) Predicted Motor Voltages



(b) Motor Currents



(c) Yaw Rate



(d) Predicted Trajectory of CM of Vehicle

Figure 5.8: Comparisons of Simulation Results and Field Test Results for Zero Radius Turn Maneuver on Dry Sand

about twenty seconds of turning, the PackBot was no longer able to turn because the magnitude of the motion resistance due to the bulldozing effect was too great. Because the track-terrain interaction model used in this study does not include the effects of slip sinkage, the simulated yaw rate is greatly over estimated on dry sand.

Figure 5.8 shows a comparison of the simulation results to those of the field test conducted on asphalt. The simulation results match much better with the experimental results as compared to the results shown in Figure 5.8 for dry sand. This is because asphalt is non-deformable so that no slip sinkage occurs. Note that the values for the simulated right motor current are negative. In this case, the motor is not in a generating state because the angular velocity of the motor has the same orientation as the torque supplied by the motor. Also notice that the transient response of the simulated yaw rate is faster than the experimental yaw rate. It was observed that when the vehicle initially turns on the asphalt something hinders the turning. This maybe due to grouser clinging on small asperities (rocks) in the asphalt, and at higher yaw rates this effect reduces.

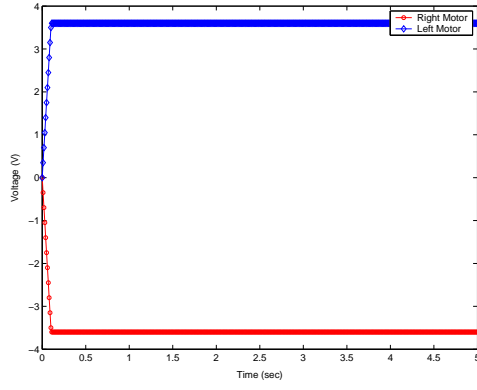
From this analysis, it apparent that the effect of slip sinkage and the bulldozing effect should be taken into account to produce realistic results on deformable terrains like dry sand. The simulation results appear to match very well on hard terrains like asphalt.

5.4 Parametric Analysis

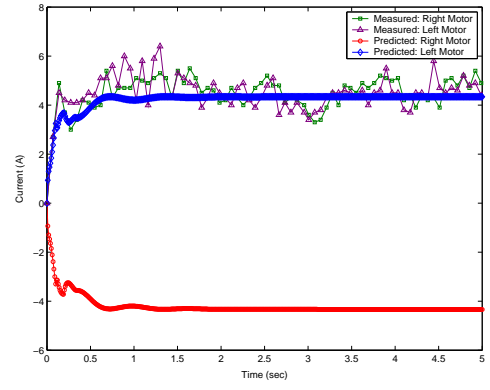
The following sections discuss the sensitivity of the model when perturbations are made to values of certain model parameters.

5.4.1 Sensitivity of Speed to Current

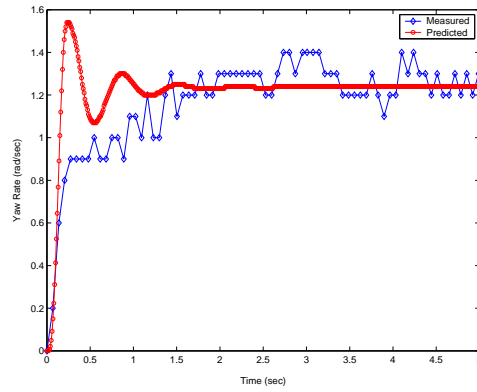
The majority of the field tests on the PackBot were performed at the same speed. In the previous section, all of the simulation results were performed at a speed of



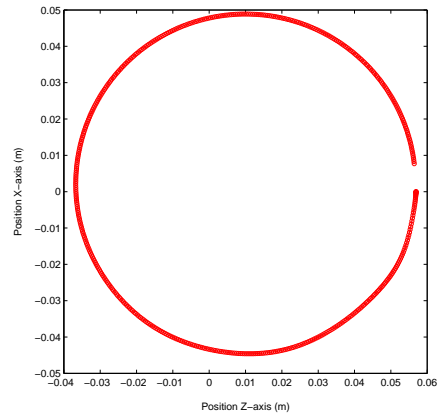
(a) Predicted Motor Voltages



(b) Motor Currents



(c) Yaw Rate



(d) Predicted Trajectory of CM of Vehicle

Figure 5.9: Comparisons of Simulation Results and Field Test Results for Zero Radius Turn Maneuver on Asphalt

1.1 m/s. There were a few tests conducted at a higher speed of 2m/s. Figure 5.10 shows a comparison of the simulation results with experimental results for a go-stop maneuver on dry sand. The first thing to notice is that the simulated ideal speed does not match the experimental ideal speed. Also, compare the experimental steady-state currents in Figure 5.2(b) and Figure 5.10(b). Notice that the currents are not that different, even when the ideal speed is doubled. This implies that the ideal speed is very sensitive to the change in current. In fact the average value of the current in Figure 5.2(b) between the interval 1-3 seconds is 1.98 A, where the average value of the experimental currents shown in Figure 5.10(b) between the interval 1-2.3 seconds is 2.23 A. Thus, a change in current of 0.34 A results in a change in ideal speed of 1.9 m/s. This can be explained by referring back to equations 5.2 and 5.3. Rearranging terms yields,

$$v_i \approx \frac{r_s}{\alpha} V_{m_{steady}}, \quad (5.8)$$

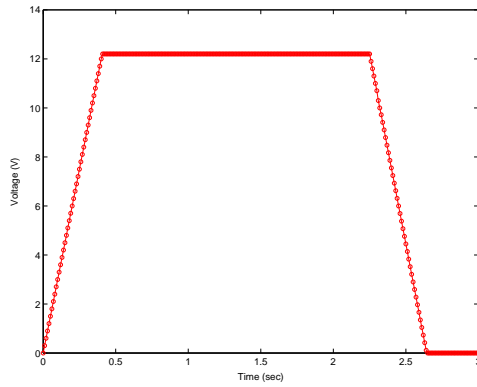
and

$$i_{m_{steady}} \approx \frac{b_{int}}{\alpha r_s} v_i, \quad (5.9)$$

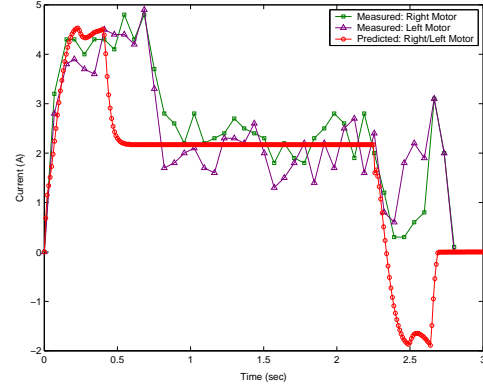
where $v_i = r_s \omega_s$ and v_i is the ideal velocity and r_s is the sprocket radius. In this model the value of $b_{int}/\alpha r_s$ is typically near unity, which implies from equation 5.9 that a unit change in current will result in an approximate unit change in ideal speed. Figure 5.11 shows simulation results showing how changing of the motor current affects the changing of the ideal speed. Notice that a unit change in current does result in an approximate unit change in ideal speed. Therefore, the model for the internal resistance given by equation 3.41 greatly affects the sensitivity of ideal speed to the change in motor current.

To fix this problem, a new model for the internal damping of the track is proposed. By modeling the internal resistance of the track as a constant,

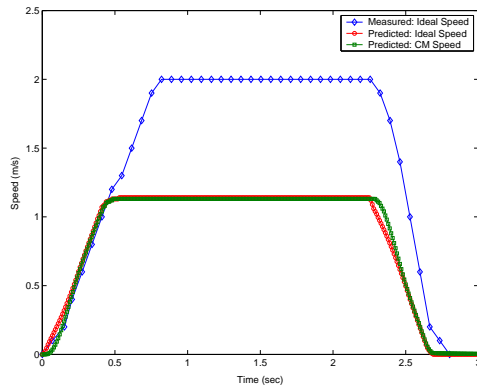
$$\tau_{int} = b_{int}^*, \quad (5.10)$$



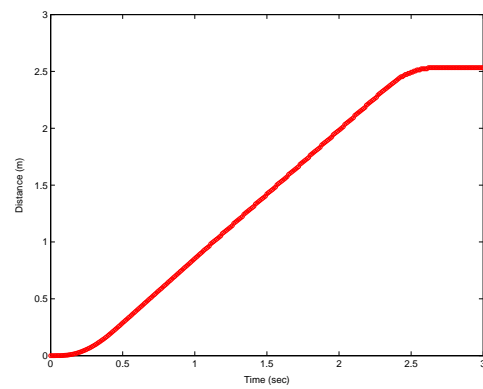
(a) Predicted Motor Voltages



(b) Motor Currents



(c) Speeds



(d) Predicted Distance Traveled

Figure 5.10: Comparisons of Simulation Results and Field Test Results for Go-Stop Maneuver on Dry Sand. The steady-state speed of the vehicle is 2 m/s

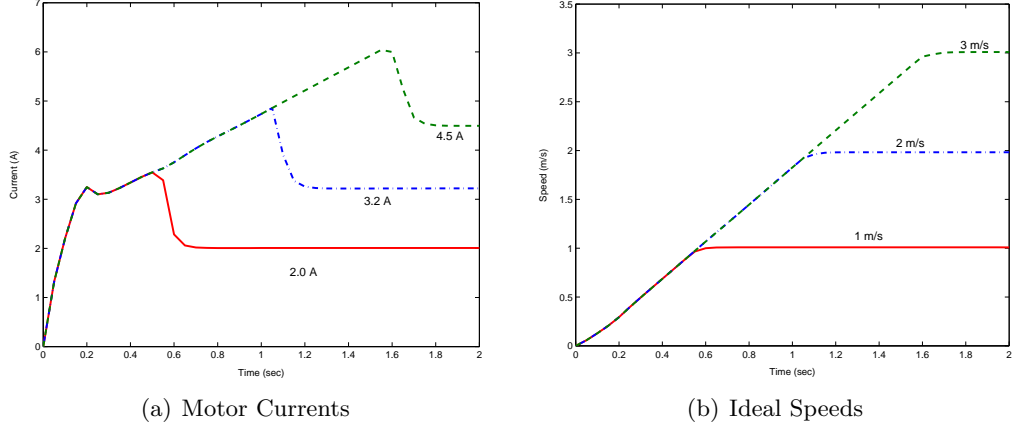


Figure 5.11: Simulations Results Showing the Sensitivity of Ideal Speed to Current

the major influence $i_{m_{steady}}$ has on v_i in equation 5.9 is removed. This is a reasonable assumption to make, since it is shown in [1] that the internal resistance may be constant within a small range of speeds. This new model changes equations 5.8 and 5.9 to,

$$v_i \approx \frac{r_s}{\alpha} V_{m_{steady}}, \quad (5.11)$$

and

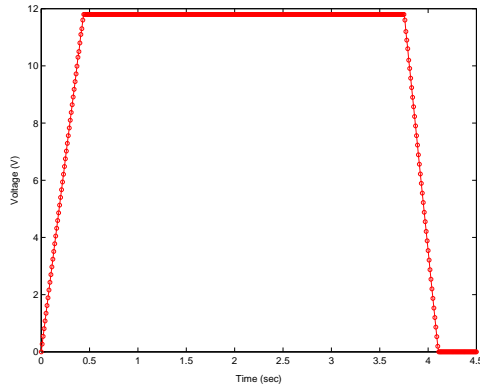
$$i_{m_{steady}} \approx \frac{b_{int}^*}{\alpha}. \quad (5.12)$$

The value of r_s/α used in this model is 0.099. This implies that a change in motor voltage of 10 V will approximately change the ideal speed by 1 m/s. Equation 5.12 implies that the current does not change very much with a change in motor voltage since b_{int}^*/α is a constant. Equations 5.11 and 5.12 can be used as starting points to estimate the value of b_{int}^* by using the experimental results at steady-state. Table 5.4 gives the values for b_{int}^* used in this model for dry sand and asphalt.

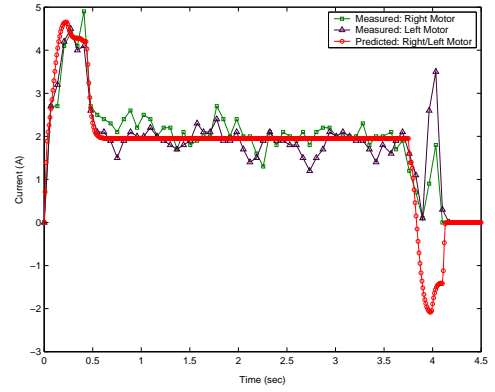
Figure 5.12 shows the simulation results using the “new internal track” resistance model for the go-stop maneuver with the steady-state ideal speed equal to 1.1 m/s. Figure 5.13 shows the results for the go-stop maneuver with the steady-

	Dry Sand	Asphalt
$b_{int}^* (N)$	0.78	0.73

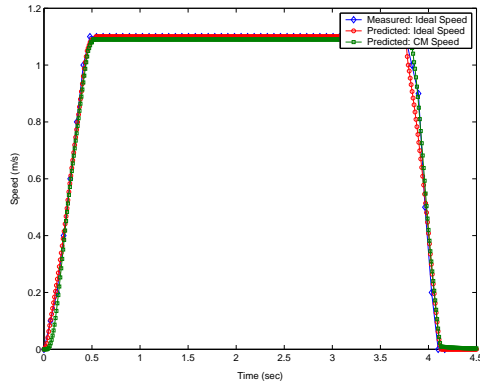
Table 5.4: Estimated Values for the Modified Internal Resistance Parameter b_{int}^* on Dry Sand and Asphalt



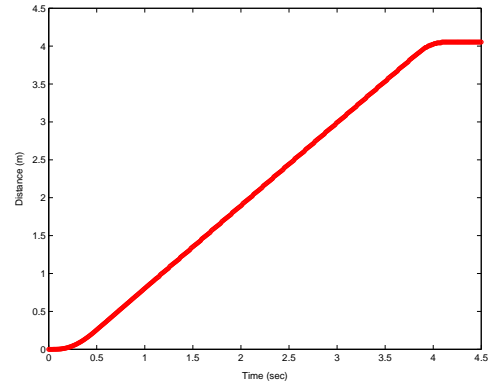
(a) Predicted Motor Voltages



(b) Motor Currents



(c) Speeds



(d) Predicted Distance Traveled

Figure 5.12: Simulation Results for Go-Stop Maneuver on Sand Using Modified Internal Track Resistance Model

Soil Type	c (kPa)	ϕ (deg)	K (cm)
dry sand 1	1.04	28	2.54
dry sand 2	0	32	2.54
sandy loam 1	1.72	29	1
sandy loam 2	4.83	20	1
sandy loam 3	1.38	38	1

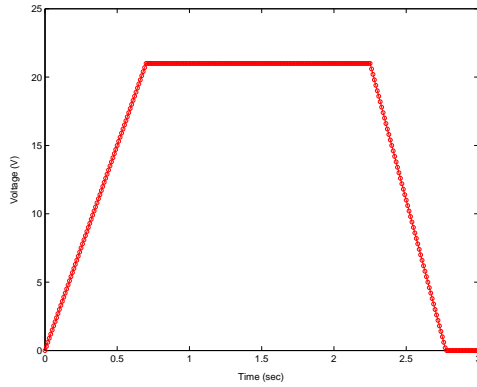
Table 5.5: Nominal Values for Terrain Parameters for Various Sands [1]

state ideal speed equal to 2 m/s. Notice that the steady-state current in Figures 5.12(b) and 5.13(b) are not that different, with the latter being a little higher. The simulated ideal speed matches the experimental speed shown in Figure 5.13(c). Also, observe from figure 5.12(a) and 5.13(a) that an approximate change of 10 V results in doubling the ideal speed.

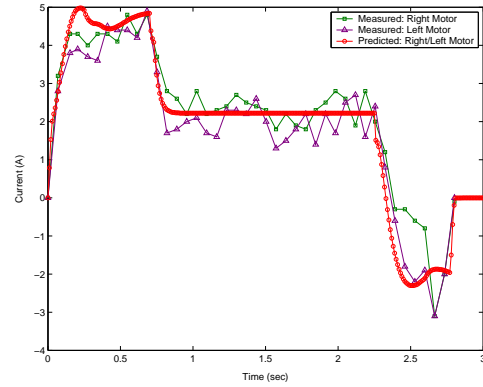
Figure 5.14 shows the results for the double-lane-change maneuver using the new model. Notice that the results agree very well with the experimental data. Therefore, it appears that the new internal track resistance model correlates much better with the experimental data than the original model. However, it is apparent from this analysis that the internal resistance of the track greatly influences the simulation results and should be further investigated.

5.4.2 Effects of Perturbations in Terrain Parameters

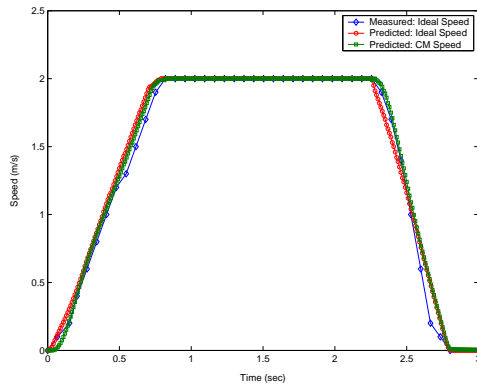
The track-terrain interaction model used in this work is dependent on parameters characterizing the response of the terrain and can influence simulation results. Therefore, parametric studies are conducted to test the sensitivity of the response predicted by the simulations to changes in soil parameters. Table 5.5 lists the values of soil parameters for various types of sands. The vehicle model was simulated on each terrain using the same input motor voltages. Figure 5.15 shows the simulated trajectories. It is apparent from the figure that the vehicle's trajectory depends to a significant extent on the nature of the soil.



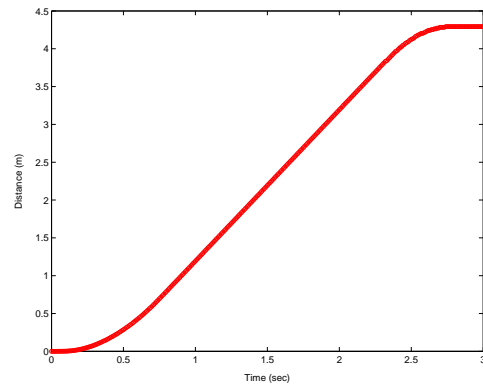
(a) Predicted Motor Voltages



(b) Motor Currents

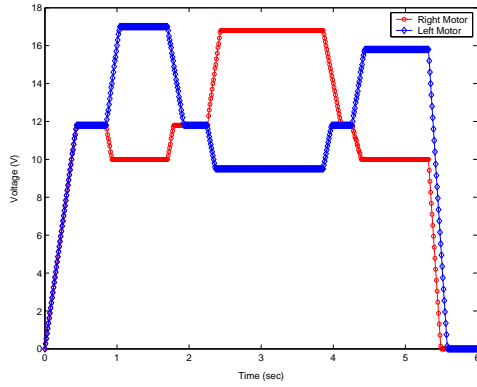


(c) Speeds

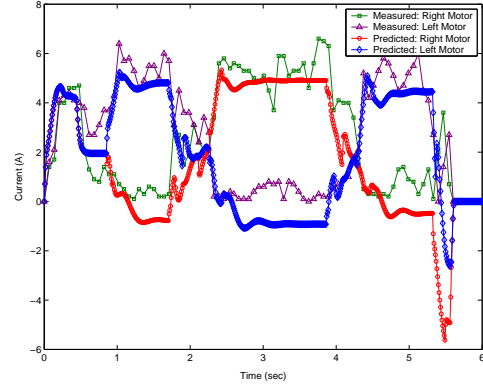


(d) Predicted Distance Traveled

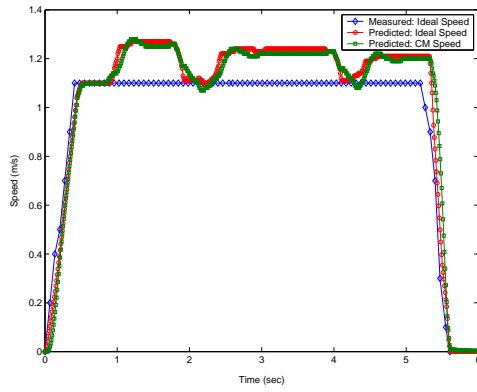
Figure 5.13: Simulation Results for Go-Stop Maneuver on Sand Using Modified Internal Track Resistance Model. The steady-state speed of the vehicle is 2 m/s



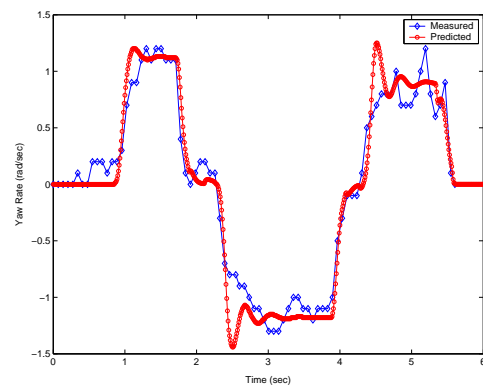
(a) Predicted Motor Voltages



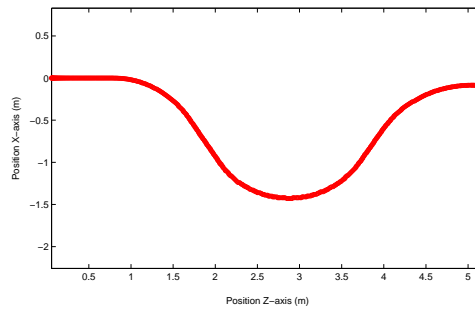
(b) Motor Currents



(c) Speeds



(d) Yaw Rate



(e) Predicted Trajectory of CM of Vehicle

Figure 5.14: Simulation Results for Double Lane Change Maneuver on Sand Using Modified Internal Track Resistance Model

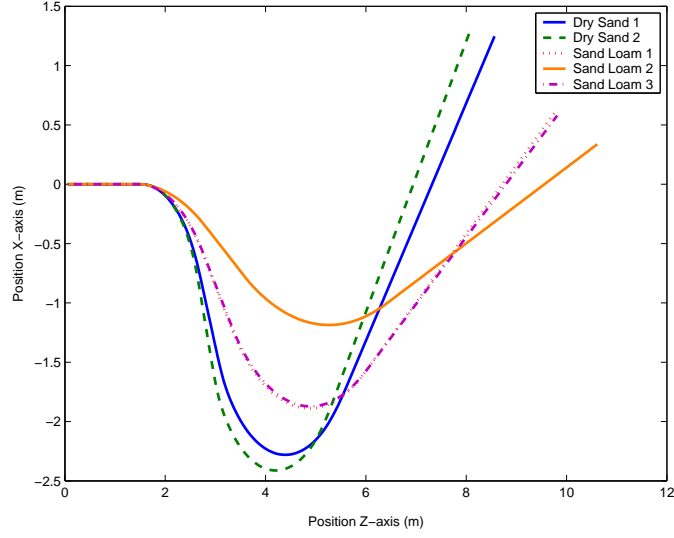


Figure 5.15: Simulated Trajectories of Vehicle Model for Various Sandy Terrains

The soils in Table 5.5 all have different values for each parameter, so it is difficult to determine how each parameter affects the simulation. Therefore, the terrain parameters given in Table 5.1 are used as baseline soil parameters. The value of a single parameter is changed keeping the others fixed. This is repeated several times and then the value of another parameter is varied keeping the others fixed. Table 5.6 shows the values of the terrain parameters. Figure 5.16 shows

c (kPa)	1.04	1.54	2.04	2.54	3.04
ϕ (deg)	23	28	33	38	43
K (in)	1.00	1.25	1.50	1.75	2.00
b_{int}^* (N)	0.780	1.170	1.755	2.633	2.896

Table 5.6: Values of Terrain Parameters Used for Sensitivity Analysis

the sensitivity response of the vehicle model to the change in value of cohesion, c . It is interesting from Figure 5.16(b) that the forward speed of the vehicle is not significantly affected by the value of c . However, the value of c has some affect on the yaw rate. Figures 5.17 and 5.18 show the sensitivity response of the vehicle

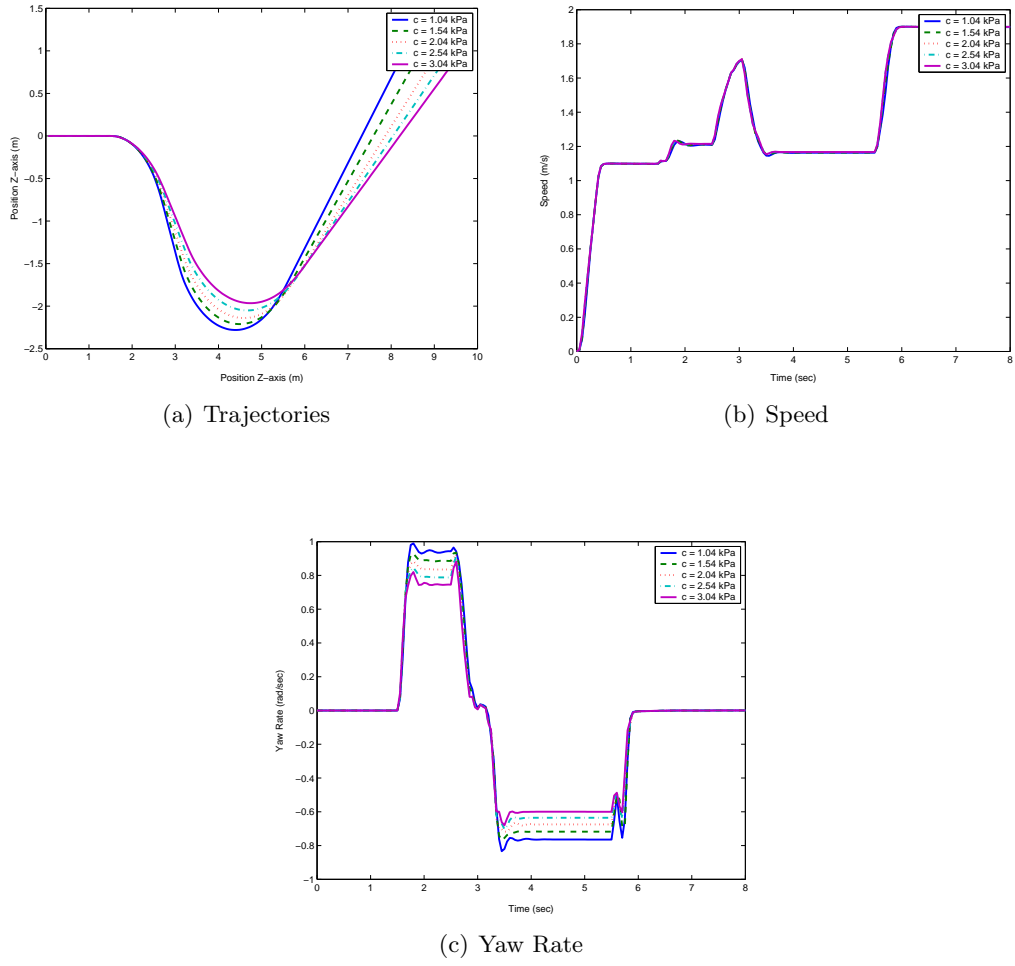


Figure 5.16: Sensitivity Response of Vehicle Model to Changing Cohesion, c

model to the change in value for friction, ϕ , and shear deformation modulus, K , respectively. Figures 5.17(b) and 5.18(b) also show that the vehicle forward speed is not significantly affected to the change in either ϕ or K . Figures 5.17(c) and 5.18(c) show that the yaw rate of the vehicle is affected to some degree to the change in these parameters. Figure 5.19 shows the sensitivity response of the vehicle model to the change in b_{int}^* . Notice, that in this case the yaw rate is not affected, but the forward speed of the vehicle does change.

It is surprising that the values of c , ϕ , and K have little affect on the forward speed of the vehicle. To get some insight on this problem, steady-state analysis is performed for the straight-line motion of a single track. The idea is to observe how the steady-state speed of the vehicle changes over a wide range in values for terrain parameters. In order to simplify the analysis (See Appendix D), it is assumed that there is an even normal pressure distribution underneath the track and that the discrete elements used to model the track-terrain interface all have the same area. Based on these assumptions, the following equations are derived,

$$\beta A \sum_{i=1}^N \left(1 - e^{-j_i/K}\right) - R_c = 0, \quad (5.13)$$

$$-r_s \beta A \sum_{i=1}^N \left(1 - e^{-j_i/K}\right) - b_{int}^* - b_{eff} \omega_s - \tau_{stick} + \alpha i_m = 0, \quad (5.14)$$

$$j_i = \frac{r_s \omega_s - v}{r_s \omega_s} z_i^*, \quad (5.15)$$

$$V_m - R_m i_m - \alpha \omega_s = 0, \quad (5.16)$$

where $\beta \equiv (c + \sigma \tan \phi)$ and is the maximum shear strength of the terrain. Equations 5.13 and 5.14 are the summation of the longitudinal forces and the torques acting on the track at steady-state, respectively. Equation 5.15 is the steady-state shear displacements at the points z_i^* for $i = 1..N$. Finally, equation 5.16 is the sum of the voltages for the motor circuit (see Section 4.3.1). For more information see Appendix

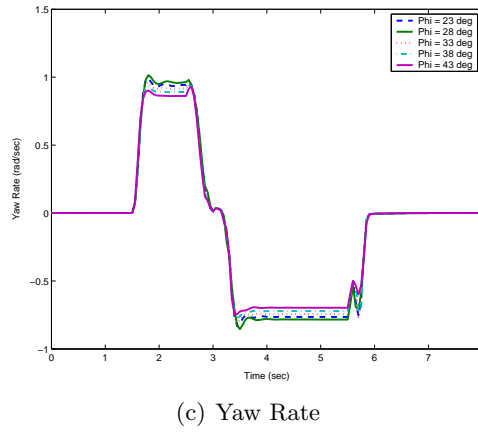
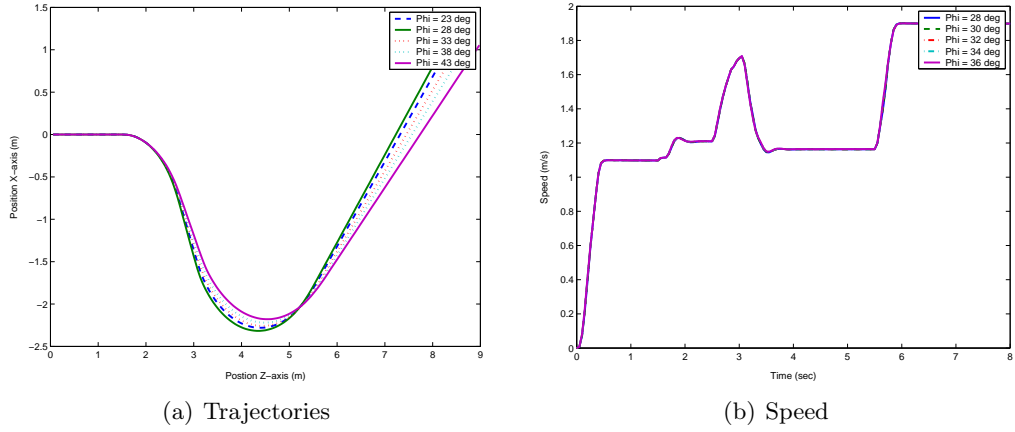


Figure 5.17: Sensitivity Response of Vehicle Model to Changing Angle of Internal Shearing Resistance, ϕ

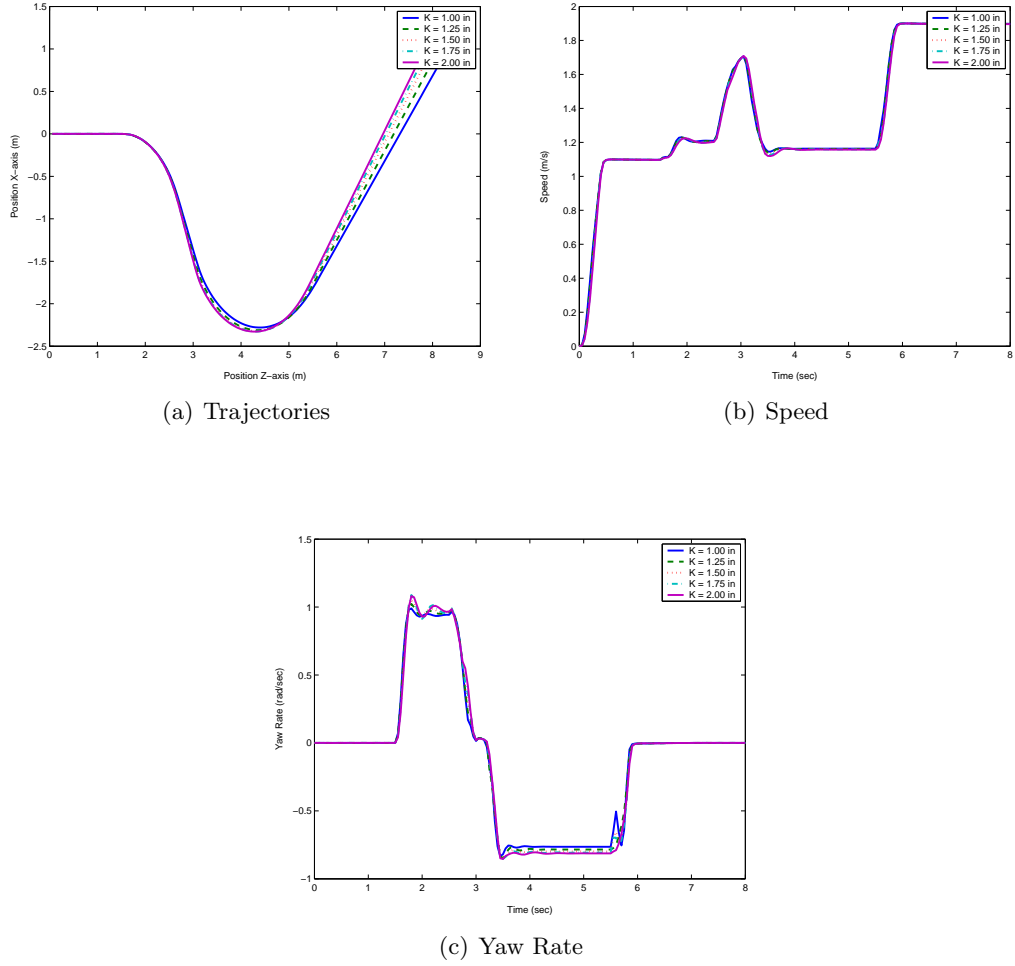
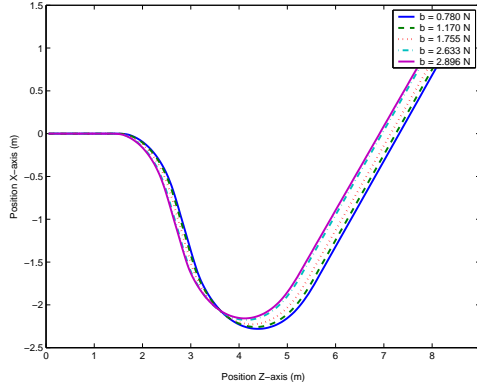
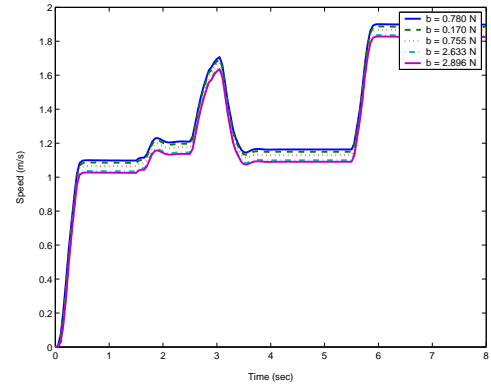


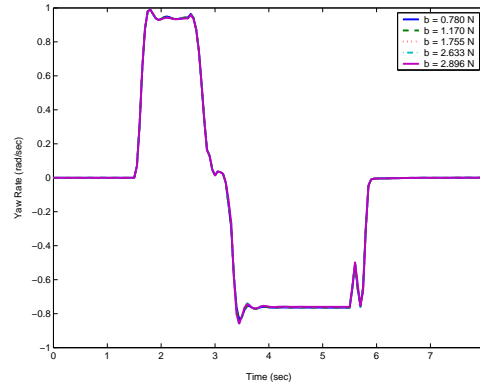
Figure 5.18: Sensitivity Response of Vehicle Model to Changing Shear Deformation Modulus, K



(a) Trajectories



(b) Speed



(c) Yaw Rate

Figure 5.19: Sensitivity Response of Vehicle Model to Changing Internal Track Resistance, b_{int}^*

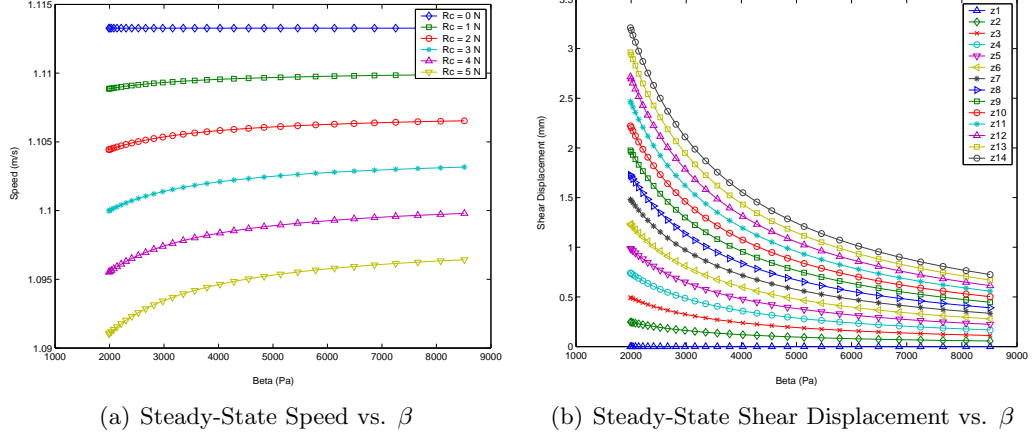


Figure 5.20: Steady-State Parametric Analysis

D. Equations 5.13-5.16 are solved to find the steady-state velocity of the track, v , angular velocity of the sprocket, ω_s , motor current, i_m , and shear displacements, j_i , at the points z_i^* . The baseline values for the parameters c , ϕ , and K used for this analysis are from Table 5.1.

From the solution to equations 5.13-5.16, Figure 5.20(a) shows how the speed of the track is influenced by β for various values of the motion resistance of the track, R_c . There are two interesting results that should be pointed out. First, notice that for a given value of R_c the simulated speed does not vary considerably as β changes, particularly as R_c approaches zero. The motion resistance of the track model presented in this thesis was computed using equation 3.40 and was found to be negligible. Because the motion resistance is practically zero, the simulated tractive forces must go to zero at steady-state in order to satisfy equation 5.13. This also implies that the longitudinal slip and the longitudinal shear displacement must go to zero at steady-state. Figure 5.20(b) shows the steady-state shear displacements at the points z_i^* for $R_c = 4\text{ N}$. Notice as β increases the simulated shear displacements decline. In other words, the greater the maximum shear stress is available, β , the less

shear displacement is required to generate enough traction to match the opposing motion resistance.

The second thing to notice is that the speed curves are insensitive to R_c . It must be noted that the values of R_c shown in Figure 5.20(a) are not computed, but are chosen arbitrary to show how the motion resistance affects the velocity to the change in β . Although small values of R_c are used for the analysis, 1-4 N, they are relatively large to what the PackBot would experience (i.e. due to static sinkage) on most distributed soils. Because the motion resistance of the vehicle model is negligible and based on the information from Figure 5.20(a) and Figure 5.20(b), this gives some insight to why the simulated speed is insensitive to the terrain parameters.

However unlike the speed, the yaw rate does appear to be affected to the change in terrain parameters. The reason for this is that the lateral slip at various points along bottom of the track are at 100% when the vehicle is turning. This occurs even if no motion resistance is present. Because of this, the lateral shear stress at most points along the bottom of the track are allowed to reach the maximum available shear stress, β . As the value of β increases the lateral shear forces also increase causing the yaw rate of the vehicle to decrease. Thus, it is apparent the lateral force model presented in Section 3.4.5 plays a big role in predicting the motion of a tracked vehicle over flat two-dimensional terrains.

5.5 Conclusion

The effectiveness of the vehicle model presented in chapters 3 and 4 has been tested. Modeling the internal resistance of the track as a function of the angular velocity of the sprocket does not correspond well with field test data. By modeling the internal resistance of the track as a constant the simulation results correlate much better with the field test data. Simulation results show that to produce realistic results on

deformable terrains, the effects of slip sinkage and the bulldozing effect should be taken into account. Finally, parametric analysis shows that the sensitivity of the vehicle simulation is affected by the value of soil parameters and may be attributed by the lateral force model (Section 3.4.5).

Chapter 6

Conclusion and Recommendation for Future Work

In this thesis, a dynamic model for predicting the mobility of a particular robotic tracked vehicle has been developed and tested for motions over flat two-dimensional terrains (deformable and non-deformable). In particular, a new approach has been presented for modeling track-terrain interaction. The “discrete approach”, as it is referred, provides a simplified model facilitating in computationally efficient estimates for motion analysis on flat terrains. In the discrete approach, the track-terrain interface continuum is approximated by discretized parameterizable force elements. A specific implementation of the discrete approach using a multi-body dynamics modeling and simulation environment, ADAMS, was presented. Normal and shear forces acting at the track-terrain interface were modeled using a parametric analysis based on the *bevameter* technique, developed by Bekker [6] and have been reviewed and revised by Wong [1, 13]. A kinematic model taking the form of a partial differential equation for shear displacement was adopted from [4]. The shear displacement

model was approximated by a series of ordinary differential equations, in which the steady-state response predicted by this model is theoretically exact, but the transient response is relatively slow.

To evaluate the effectiveness of the discrete approach, comparisons were made between simulated results and those obtained from field-testing an iRobot PackBot at Southwest Research Institute's robotic vehicle test range. The field tests consisted of subjecting the vehicle to four different types of maneuvers on both dry sand and asphalt. The maneuvers performed were a go-stop, j-turn, double-lane-change, and a zero radius turn. The nominal values for the characteristic parameters of the terrains were obtained from the literature.

The simulated results on asphalt matched very well with those obtained from field tests providing some validation that this vehicle model can be effective for motion analysis on flat non-deformable terrains. The simulated results on dry sand also matched well with those obtained from field tests, with the exception of the zero radius turn maneuver. As expected, the effect of slip-sinkage gives rise to a bulldozing effect and has a profound impact on the turning motion of the vehicle for large radius turn maneuvers. These effects were neglected in the track-terrain interaction model yielding unrealistic results for large radius turn maneuvers. The results from this study provides some validation that existing methods used for analyzing the mobility performance of large scale tracked vehicles suffice for evaluating small robotic tracked vehicles. However, parametric analysis has shown that the forward speed of the PackBot is insensitive to changes in the terrain parameters c , ϕ , and K . This may be partially explained by the fact that the motion resistance of the PackBot due to any *static* sinkage is negligible even on soft terrains like dry sand. Because of this, it may be possible to make simplifications to the track-terrain interaction model for tracked vehicles similar in size to the PackBot that may not be valid for large scale vehicles. The simulated results presented in this thesis introduce

issues that need to be addressed for future work.

6.1 Future Work

The following summarizes the issues that need to be further studied in future work.

6.1.1 Shear Displacement Model

A kinematic model for the longitudinal shear displacement was proposed by [4], which is in the form of a partial differential equation,

$$\frac{\partial j}{\partial t} + r_s \omega_s \frac{\partial j}{\partial z} = r_s \omega_s - v.$$

In this thesis, an assumption was made that the shear displacement increases linearly along the length of the track with the slope of the line being a function of time only. Although this assumption is true under steady-state conditions, it is not valid for transient motion conditions. Because of the assumption made, the model required a modification to better handle the transient motions of the track. The particular function used to modify the simplified shear displacement model was the STEP5 function provided in the ADAMS environment. This function introduces parameters to the model whose values must be selected by tuning the model. This can generate inaccurate results since logic is used in modeling the shear displacements. Therefore, further study is needed to either develop a better simplified model or develop and implement a numerical algorithm to solve the partial differential equation.

The sensitivity analysis presented in Chapter 6 showed that the forward velocity of the PackBot was insensitive to the change in parameters c , ϕ , and K . This issue needs to be further investigated and several tests need to be conducted on various terrains to confirm this result. If this result is found to be valid then it may be possible to simplify the longitudinal force model presented in Section 3.4.3. For

example, the forces may be characterized using a model similar to Coulomb friction, and thus simplifying the model by eliminating the need to compute the longitudinal shear displacement developed along the track-terrain interface.

6.1.2 Lateral Force Model and Slip-Sinkage

The lateral force model presented in this thesis is based on the approach taken in [19]. In this approach, the lateral shear forces are modeled using the same shear stress-shear displacement relationships used to model the longitudinal forces. This is beneficial since the same shear stress parameters c , ϕ , and K may be used without introducing additional parameters. However, the way the track engages with the terrain in the lateral direction is not the same as in the longitudinal direction. The lateral force model used in this thesis does not take into account slip-sinkage, which can give rise to the bulldozing effect and can have a profound impact on the turning motion of the vehicle.

Therefore, alternative lateral force models in the literature need to be investigated. For example, one of the more widely used models is to relate the lateral forces using a lateral coefficient of friction. Kar [17] and Wong [1] argue that the lateral coefficient of friction is a function of the turning radius of the vehicle, explaining why the track forces decrease with an increasing turning radius. Based on this argument, we could model the lateral shear force acting on the i^{th} discrete element as,

$$F_{Lat_i} = \mu_t(\rho_i) F_{n_i}$$

where μ_t is the lateral coefficient of friction that is a function of the turning radius ρ_i of the i^{th} wheel, and F_{n_i} is the normal force acting on the i^{th} discrete element. In this model, the lateral forces due to the shearing of the terrain and the bulldozing effect are lumped together. The downside to this model is that the relationship between μ_t and ρ_i depends on the type of terrain and the design of the track. Therefore,

field tests would have to be conducted to estimate the relationship between μ_t and ρ_i .

6.1.3 Internal Resistance of Track

It was shown in this thesis that the internal resistance of the track greatly affected the simulated results. In the literature, this force is modeled in different ways. In [4] the internal losses were modeled as a linear viscous friction torque acting around the sprocket shaft. A similar approach was adopted for the model presented in this thesis. In [1], Wong models the internal losses as a force acting along the length of the track and is related to the speed of the vehicle. Further study needs to be conducted in order to develop a more fundamental understanding and the nature of this force.

6.1.4 Test Vehicle

The test vehicle is equipped with various sensors. In the field tests conducted for this thesis, the motor currents, ideal speed, and the yaw rate of the vehicle were monitored. In order to provide more support for the validity of the vehicle model, additional metrics need to be monitored and modifications need to be made to sensors currently available (e.g. motor currents). Monitoring of the following metrics would be very desirable:

- longitudinal speed of the vehicle
- trajectory of the vehicle using a GPS device with adequate resolution
- estimate of the forces developed at the track-terrain interface using accelerometers
- motor voltages
- motor currents (negative and positive values)

6.2 Conclusion

The tracked vehicle model developed in this thesis presents a viable means for motion analysis over flat two-dimensional terrains. A new approach to modeling track-terrain interaction has been introduced that is simple, yet practical for motion analysis and computationally efficient. Simulation results are compared to those from field tests of a robotic tracked vehicle providing validation for the model. In light of evidence from parametric studies, future work is to be conducted to develop models that better approximate the forces acting at the track-terrain interface.

Appendix A

Specifications of PackBot

This appendix gives the basic dimensions of the PackBot and some specifications.

DIMENSIONS

Height - 7.14" ground to top of clear

Width - 16" main track to track

Length - 27" with flippers stowed and 34.5" with flippers fully extended

SPECIFICATIONS

Weight - 40 pounds (depending on payload)

Max Shock - 400G's

Waterproof - up to 3 meters depth

Speed - Nominal 2.2 m/s and up to 3.7 m/s in high speed mode

Flipper Velocity - 100 deg/sec

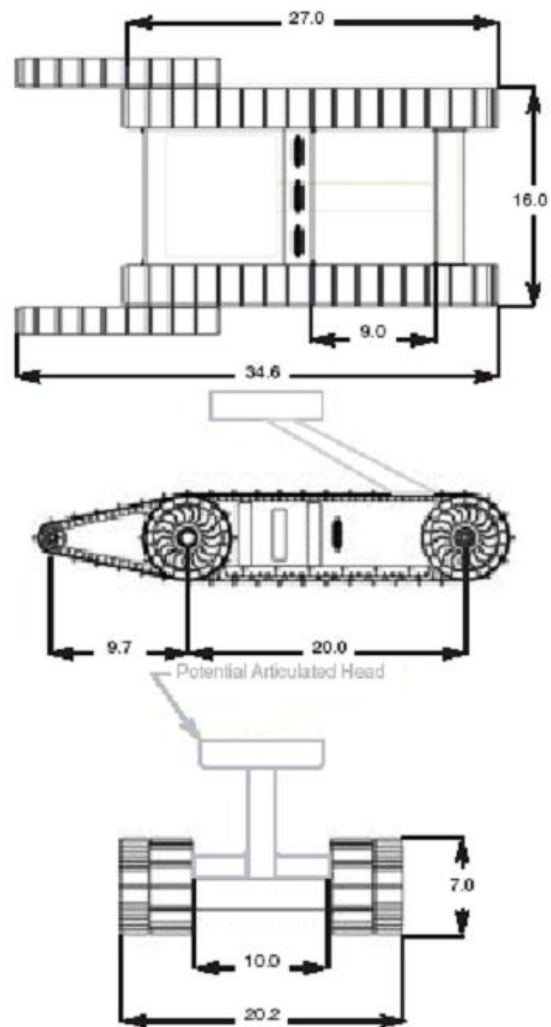


Figure A.1: Geometric Dimensions of PackBot

Appendix B

Derivation of Motor and Drive Train Model

This appendix gives a derivation of the motor and drive train model. Also, the values of the parameters used in the model are given.

B.1 Deriving the Effective Inertias of Motor/Drivetrain System

Figure B.1 shows an illustration of the basic components comprising the motor, drive train, and track system of the PackBot. The system is constrained resulting in a single degree-of-freedom defined by a rotation. The state equations used to model the rotational dynamics of the motor, drive train, and track system are derived using the bond graph approach. The bond graph of the system is shown in Figure B.2. The DC motor armature current is modeled to include the terminal inductance and resistance of the motor, labeled L_m and R_m , respectively. On the mechanical side of the model (i.e. to the right of the gyrator) there are three 1-junctions. There are three distinct angular velocities observed throughout the system. Each

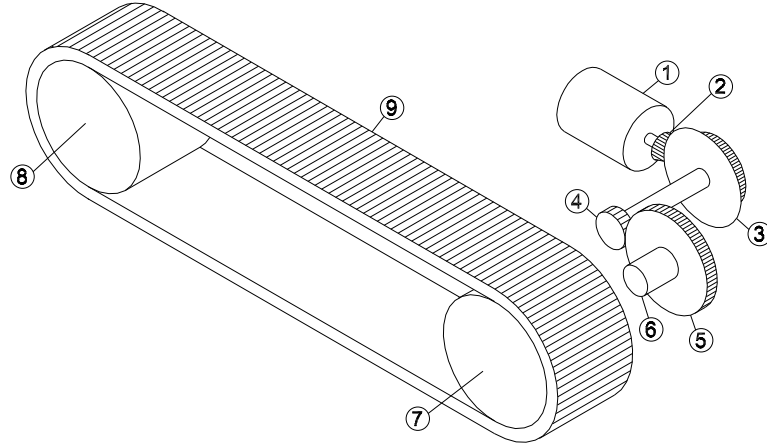


Figure B.1: Track/Drive-train Components

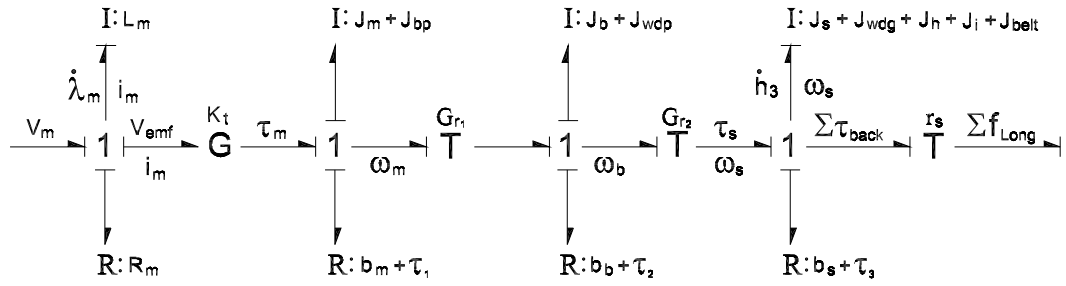


Figure B.2: Bond Graph of Motor and Drive Train System

1-junction has an I -element and a R -element. To simplify the model, the inertias of the components having the same angular velocity are summed together. Beginning with the track, the total kinetic energy of the track (i.e. sprocket, idler and the belt) is computed as follows,

$$\begin{aligned} KE_{track} &= \frac{1}{2} J_s \omega_s^2 + \frac{1}{2} J_i \omega_s^2 + \frac{1}{2} \left(\int_l \rho_{belt} dl \right) v_{belt}^2, \\ &= \frac{1}{2} J_s \omega_s^2 + \frac{1}{2} J_i \omega_s^2 + \frac{1}{2} (m_{belt} r_s^2) \omega_s^2. \end{aligned} \quad (B.1)$$

Collecting terms yields,

$$KE_{track} = \frac{1}{2} (J_s + J_i + m_{belt} r_s^2) \omega_s^2. \quad (B.2)$$

Therefore, the effective inertia of the track is

$$J_{track} = J_s + J_i + m_{belt} r_s^2. \quad (B.3)$$

The inertias of the sprocket, idler, and the sprocket can be summed together to form an “effective” inertia because they share the same angular velocity. Applying this concept to the rest of the system, the following effective inertias are defined,

$$J_1 = J_m + J_{bp} \quad (B.4)$$

$$J_2 = J_b + J_{wdp} \quad (B.5)$$

$$J_3 = J_{track} + J_h + J_{wdg}. \quad (B.6)$$

A description of these inertia parameters is given in Table B.2. The R -element at each 1-junction represents the losses due to friction.

Assigning causality to the bond graph shows that only one I -element can be chosen to have integral causality, which is to be expected since the system has

one degree-of-freedom. Letting the J_3 element have integral causality, we choose the angular velocity of the sprocket, ω_s , to be a state variable. The second state variable is chosen to be the current, i_m , going to the dc motor. The first state equation comes from the rate-of-change of momentum of the sprocket and is given by,

$$\begin{aligned} \dot{h}_3 = J_3 \frac{d\omega_s}{dt} = & G_r K_t i_m - (G_{r2}^2 J_2 + G_r^2 J_1) \omega_s - (b_3 + G_{r2}^2 b_2 + G_r^2 b_1) \omega_s \\ & - (\tau_{stick3} + G_{r2} \tau_{stick2} + G_r \tau_{stick1}) - \sum_{i=1}^N \tau_{back_i}, \end{aligned} \quad (\text{B.7})$$

where $G_r \equiv G_{r1} G_{r2}$. Rearranging and collecting terms yields,

$$\begin{aligned} (J_3 + G_{r2}^2 J_2 + G_r^2 J_1) \frac{d\omega_s}{dt} = & G_r K_t i_m - (b_3 + G_{r2}^2 b_2 + G_r^2 b_1) \omega_s \\ & - (\tau_{stick3} + G_{r2} \tau_{stick2} + G_r \tau_{stick1}) - \sum_{i=1}^N \tau_{back_i}. \end{aligned} \quad (\text{B.8})$$

Defining the terms,

$$J_{eff} \equiv J_3 + G_{r2}^2 J_2 + G_r^2 J_1 \quad (\text{B.9})$$

$$b_{eff} \equiv b_3 + G_{r2}^2 b_2 + G_r^2 b_1 \quad (\text{B.10})$$

$$\tau_{stick} \equiv \tau_{stick3} + G_{r2} \tau_{stick2} + G_r \tau_{stick1}, \quad (\text{B.11})$$

and inserting them into equation B.8 gives,

$$J_{eff} \frac{d\omega_s}{dt} = G_r K_t i_m - b_{eff} \omega_s - \tau_{stick} - \sum_{i=1}^N \tau_{back_i}. \quad (\text{B.12})$$

The terms on the right-hand-side of equation B.12 represent torques. The following gives a detailed description of each torque term in equation B.12.

$J_{eff} \frac{d\omega_s}{dt}$: The effective rate-of-change of the angular momentum of the sprocket,

where J_{eff} is the effective inertia “observed” at the sprocket and ω_s is the angular velocity of the sprocket.

$G_r K_t i_m$: Torque applied by the motor and drive train system to the sprocket, where GR is the overall gain of the drive train, K_t is the motor torque constant and i_m is the current flowing through the motor. This torque is directly applied to the sprocket.

$b_{eff} \omega_s$: The effective rotational losses due to friction “observed” at the sprocket. The rotational damping losses of the motor, drive train, and track system are lumped to the losses in the sprocket. The parameter b_{eff} is the effective damping coefficient. This damping torque is directly applied to the sprocket.

$SIGN(\omega_s) \tau_{stick}$: The effective stiction “observed” at the sprocket. The stiction torque is directly applied to the sprocket.

$\sum_{i=1}^N \tau_{Back_i}$: Total back-torque due to the longitudinal forces developed due to the longitudinal shearing of the terrain (see section 3.4.3.1).

Dividing equation B.12 by J_{eff} yields the first state equation and is given by,

$$\frac{d\omega_s}{dt} = \frac{1}{J_{eff}} \left[G_r K_t i_m - b_{eff} \omega_s - \tau_{stick} - \sum_{i=1}^N \tau_{back_i} \right]. \quad (B.13)$$

The second state equation comes from the rate-of-change of the flux linkage of the motor and is given by,

$$L_m \frac{di_m}{dt} = V_m - R_m i_m - K_v G_r \omega_s. \quad (B.14)$$

The following gives a detailed description of each term given in equation B.14.

$L_m \frac{di_m}{dt}$: The rate-of-change of the flux linkage, where L_m is the inductance and i_m is the current going to the motor.

V_m : Voltage supplied to the motor.

$R_m i_m$: Voltage drop due to the resistance of the coils, where R_m is the resistance of the coils.

$K_v G_r \omega_s$: Back emf due to the rotation speed of the rotor, $\omega_m = G R \omega_s$, where K_v is the speed constant of the motor.

Dividing equation B.14 by L_m yields the second state equation and is given by,

$$\frac{di_m}{dt} = \frac{1}{L_m} [V_m - R_m i_m - K_v G_r \omega_s]. \quad (\text{B.15})$$

The following tables give values for the parameters used in the motor, drive train, and track model.

Parameter	Description	Value
J_m (g cm ²)	Rotor inertia	134
L_m (mH)	Terminal inductance	0.08
R_m (Ohm)	Terminal resistance	0.316
K_t (mNm/A)	Torque constant	30.2
K_v (rpm/V)	Speed constant	317

Table B.1: Motor Data

Part	Parameter	Component	Value
1	J_m (g cm ²)	Rotor inertia	0.007
2	J_{bp} (lb in ²)	Bevel pinion	2.25×10^{-4}
3	J_b (lb in ²)	Bevel	0.007
4	J_{wp} (lb in ²)	Wheel pinion	0.002
5	J_{wg} (lb in ²)	Wheel gear	0.056
6	J_{wh} (lb in ²)	Wheel hub	0.017
7	J_s (lb in ²)	Sprocket	1.196
8	J_i (lb in ²)	Idler	1.196
9	J_{belt} (lb in ²)	Belt	14.308

Table B.2: Inertia Values of Motor, Drive Train, and Track Components

Parameter	Description	Value
J_{eff} (kg m ²)	Effective inertia	0.017
b_{eff} (kg m/s)	Effective damping coefficient	0.0244221
τ_{stick} (Nm)	Effective stiction	0.56876
G_{r1}	Drive train gain	64/16
G_{r2}	Drive train gain	112/15

Table B.3: Values for Motor, Drive Train, and Track Parameters

Appendix C

Extended Information for Chapter 3

This appendix gives additional information for Chapter 3.

C.1 Validation of Lateral Shear Displacement Model

Figure C.1 shows a point P moving along the track-terrain interface. The track has a longitudinal velocity of v_{track} and has an angular velocity normal to the ground represented by ω_y . Let j_x represent the lateral shear displacement developed at the point P as it moves along the contact patch. The lateral shear displacement may be expressed in Lagrangian variables as,

$$j_{x_L} = j_{x_L}(x_0, z_0, \hat{t}), \quad (\text{C.1})$$

where x_0 and z_0 define the initial position of the point P and \hat{t} is time. The shear displacement of any point along the track-terrain interface may be expressed in Eulerian variables as,

$$j_{x_E} = j_{x_E}(x, z, t), \quad (\text{C.2})$$

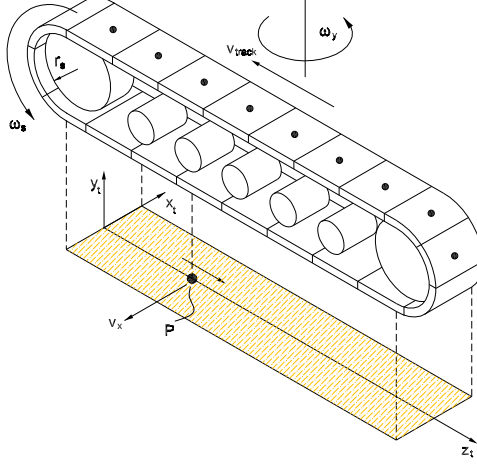


Figure C.1: Characterizing the Lateral Shear Displacement Using the Eulerian Viewpoint for Modeling Track-Terrain Interaction

where x and z define the location of the point of interest and t is time. In order to equate equations C.1 and C.2, the following transformations

$$x = r_x(x_0, z_0, \hat{t}) \quad (\text{C.3})$$

$$y = r_y(x_0, z_0, \hat{t}) \quad (\text{C.4})$$

$$t = \hat{t}, \quad (\text{C.5})$$

must be substituted into equation C.2 so that the same point, P , is being followed using both viewpoints. Substituting the transformations into equation C.2 yields,

$$j_x = j_{x_L}(x_0, z_0, \hat{t}) = j_{x_E}(r_x(x_0, z_0, \hat{t}), r_y(x_0, z_0, \hat{t}), t = \hat{t}). \quad (\text{C.6})$$

The rate of change of j_x is found using the chain rules of calculus so that,

$$\frac{\partial j_{x_L}}{\partial \hat{t}} = \frac{\partial j_{x_E}}{\partial x} \frac{\partial r_x}{\partial \hat{t}} + \frac{\partial j_{x_E}}{\partial z} \frac{\partial r_z}{\partial \hat{t}} + \frac{\partial j_{x_E}}{\partial t} \frac{\partial t}{\partial \hat{t}}. \quad (\text{C.7})$$

The terms $\frac{\partial r_x}{\partial t}$ and $\frac{\partial r_z}{\partial t}$ represent the velocity of the point P relative to the track (i.e. as if the track was fixed). The point P has a relative velocity of $r_s\omega_s$ along the z_t -axis, where r_s and ω_s are the sprocket radius and rotation velocity, respectively. The point P does not have a relative velocity component along the x_t axis (not to confused with v_x which is an absolute velocity), so that $\frac{\partial r_x}{\partial t} = 0$. Therefore, equation C.7 reduces to,

$$\frac{\partial j_{x_L}}{\partial \hat{t}} = r_s\omega_s \frac{\partial j_{x_E}}{\partial z} + \frac{\partial j_{x_E}}{\partial t}. \quad (\text{C.8})$$

In [19], Rubinstein and Hitron adopt the Lagrangian viewpoint to modeling the tracks of the vehicle (see Section 3.3.1). Rubinstein and Hitron calculate the lateral shear displacement j_x of a particular track link by integrating its lateral slip velocity, v_x , with respect to the time, \hat{t} , it is in contact with the ground. This is given by,

$$j_x = \int_{\hat{t}} v_x dt. \quad (\text{C.9})$$

Differentiating equation C.9 with respect to \hat{t} yields,

$$\frac{dj_x}{d\hat{t}} = v_x. \quad (\text{C.10})$$

The left-hand-side of equation C.10 is equivalent to the left-hand-side of equation C.8. Therefore, we have the following relationship,

$$\frac{\partial j_{x_L}}{\partial \hat{t}} = r_s\omega_s \frac{\partial j_{x_E}}{\partial z} + \frac{\partial j_{x_E}}{\partial t} = v_x \quad (\text{C.11})$$

This result shows that the lateral shear displacement model proposed in [19] and the model given by equation 3.25 are equivalent.

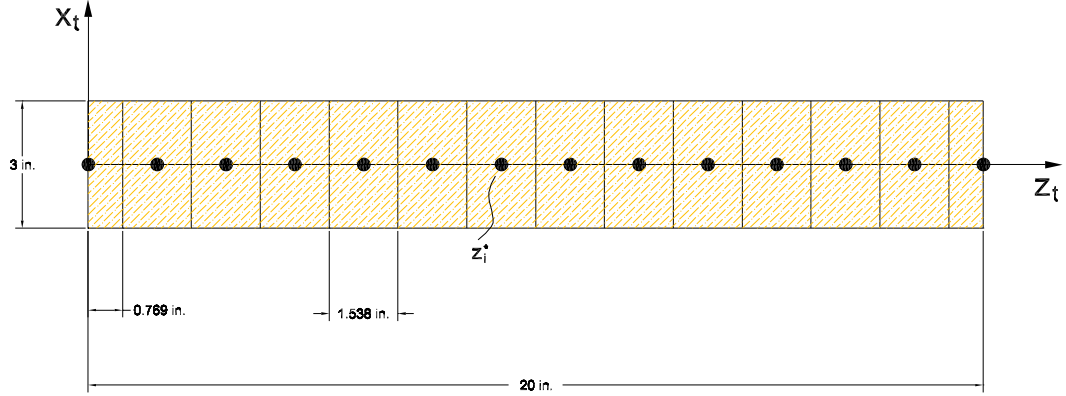


Figure C.2: Discretizing of Contact Patch for PackBot Track-Terrain Interaction Model

C.2 Dimensions of Discretized Track-Terrain Interface

Figure C.2 illustrates how the track-terrain interface is discretized using the discrete approach to model the track-terrain interaction of the PackBot. The contact patch has a length of 20 in. and a width of 3 in. The main tracks of the PackBot have grousers that are approximately 1.5 in. apart. The number of discrete element was determined by dividing the length of the track by the distance between the grousers. This gave a total of 13 discrete elements each having a length of 1.538 in. However, one of the elements was divided into two equal elements, which were assigned to the extreme ends of the contact patch. Typically, the shear stress at the extreme ends of the contact patch are either at a minimum or a maximum value relative to the other points along the contact patch. In the discrete approach, the shear stresses are evenly distributed across the area of the element. By reducing the area of the elements, the overall forces will less likely to be dominated by the dynamics at the extreme ends (although not yet proven). As a result, a total of 14 discrete elements were used in modeling the track-terrain interaction for the PackBot.

C.3 Values for Computational Based Parameters

Description	Parameter	Value
parameter to compute z_i^*	ΔV_z	1.0 e-2
parameter to prevent division by zero	ΔZ	1.0 e-6
STEP5 parameters to compute long. shear disp.	$x_{0_{jz}}, x_{0_{jz}}$	1.0 e-3, 1.5 e-2
STEP5 parameters to compute long. force	$x_{0_{fz}}, x_{0_{fz}}$	-1.0 e-9, 1.0 e-9
STEP5 parameters to compute lat. shear disp.	$x_{0_{jx}}, x_{0_{jx}}$	-5.0 e-4, 5.0 e-3
STEP5 parameters to compute lat. force	$x_{0_{fx}}, x_{0_{fx}}$	-3.0 e-2, 3.0 e-2
STEP5 parameters to compute motion resistance	$x_{0_{Rc}}, x_{0_{Rc}}$	-2 e-1, 2 e-1

Table C.1: Values for Computational Based Parameters

Appendix D

Sensitivity of Vehicle Response to the Change in Terrain Parameters

Figure D.1 shows the forces acting on a single track when moving along a straight line. At steady-state the tractive forces and the motion resistance sum to zero so that,

$$\sum_{i=1}^N F_{Long_i} - R_c = 0,$$
$$\sum_{i=1}^N \left\{ (c + \sigma_i \tan \phi) \left(1 - e^{-j_i/K} \right) A_i \right\} - R_c = 0, \quad (D.1)$$

where c , ϕ , and K are terrain parameters, σ_i , A_i , and, j_i are the normal pressure, area, and shear displacement of the i^{th} element, respectively and R_c is the motion resistance due to the compaction of the terrain. At steady-state, the torques acting

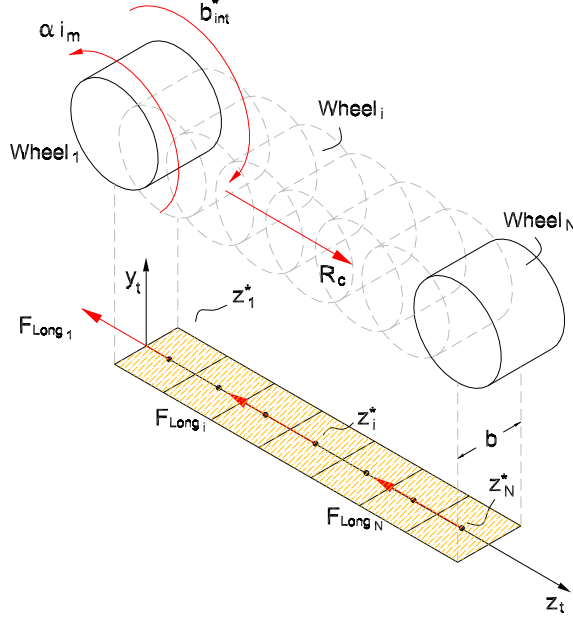


Figure D.1: Forces Acting on a Single Track

on the track (see Section 4.3.1) sum to zero so that,

$$\begin{aligned}
 & -r_s \sum_{i=1}^N F_{Long_i} - b_{int}^* + \alpha i_m = 0, \\
 & -r_s \sum_{i=1}^N \left\{ (c + \sigma_i \tan \phi) \left(1 - e^{-j_i/K} \right) A_i \right\} - b_{int}^* - b_{eff} \omega_s - \tau_{stick} + \alpha i_m = 0,
 \end{aligned} \tag{D.2}$$

where r_s is the sprocket radius, b_{int}^* is the internal damping of the track, b_{eff} and τ_{stick} are friction parameters, i_m is the motor current, and $\alpha \equiv K_t G_r$ and $K_v G_r$ since $K_t G_r$ and $K_v G_r$ have the same values when consistent units are used. The steady-state shear displacement developed at the points z_i^* is given by,

$$j_i = \frac{r_s \omega_s - v}{r_s \omega_s} z_i^* \tag{D.3}$$

Finally, at steady-state the motor circuit is modeled as (see Section 4.3.1),

$$V_m - R_m i_m - \alpha \omega_s = 0, \quad (\text{D.4})$$

where V_m is the motor voltage and R_m is the terminal resistance. To simplify the analysis without any loss in generality, it is assumed that there is an even normal pressure distribution σ underneath the track and that each element has the same discrete area A . Based on these assumptions we define,

$$A_i \equiv \frac{A}{N}, \quad (\text{D.5})$$

$$\sigma_i \equiv \sigma = \frac{1}{2} \frac{W}{A}, \quad (\text{D.6})$$

$$\beta \equiv c + \sigma \tan \phi, \quad (\text{D.7})$$

where W is the weight of the vehicle and N is the number of elements. Inserting these definitions into equations D.1-D.4 yields the following,

$$\beta A \sum_{i=1}^N \left(1 - e^{-j_i/K} \right) - R_c = 0, \quad (\text{D.8})$$

$$-r_s \beta A \sum_{i=1}^N \left(1 - e^{-j_i/K} \right) - b_{int}^* + \alpha i_m = 0, \quad (\text{D.9})$$

$$j_i = \frac{r_s \omega_s - v}{r_s \omega_s} z_i^*, \quad (\text{D.10})$$

$$V_m - R_m i_m - \alpha \omega_s = 0. \quad (\text{D.11})$$

Equations D.8-D.11 are solved to find the steady-state velocity of the track v , angular velocity of the sprocket ω_s , motor current i_m , and shear displacements j_i at the points z_i^* . The parameter β represents the maximum shear strength of the terrain and is a free parameter. The motor voltage, V_m , motion resistance, R_c , and the values of z_i^* for $i = 1..N$ are also free parameters. Once the values for V_m and z_i^* are

chosen, they are fixed. For a given value of R_c , equations D.8-D.11 are then solved multiple times by varying β over a range of values. The process is then repeated for various values of R_c . The unknown variables v , ω_s , j_i , and i_m can then be plotted versus β as shown in figures 5.20(a) and 5.20(b).

Bibliography

- [1] J.Y. Wong. *Theory of Ground Vehicles*. John Wiley & Sons, Inc, New York,NY, 3rd edition, 2001.
- [2] M.G. Bekker. *Introduction to Terrain-Vehicle Systems*. University of Michigan Press, 1969.
- [3] A. Bodin. Development of a tracked vehicle to study the influence of vehicle parameters on tractive performance in soft terrain. *Journal of Terramechanics*, 36:167–181, 1999.
- [4] Gianni Ferretti and Roberto Girelli. Modelling and simulation of an agricultural tracked vehicle. *Journal of Terramechanics*, 36:139–158, 1999.
- [5] M. Kitano, K. Watanabe, Y. Takaba, and K. Togo. Lane-change maneuver of high speed tracked vehicles. *Journal of Terramechanics*, 25:91–102, 1988.
- [6] M.G. Bekker. *Theory of Land Locomotion*. University of Michigan Press, 1956.
- [7] K. Kühner. “das kraftfahrzeug im gelände”. (Motor vehicle in terrain), 1935.
- [8] Gruzdev. Tanki-teorya. *IKTM*, 1944.
- [9] Z.J. Janosi. Obstacle performance of tracklayer vehicles. pages 40–60. J.N. Siddall and P.H. Southwell, August 29-September 2 1966.

- [10] K. Terzaghi. *Theoretical Soil Mechanics*. J. Wiley & Sons, New York, N.Y., 1944.
- [11] Bill McBride, Raul Longoria, and Eric Krotkov. Measurement and prediction of the off-road of small robotic ground vehicles. SwRI, 2003.
- [12] M.G. Bekker. *Off-the-Road Locomotion*. University of Michigan Press, 1960.
- [13] J.Y. Wong. Data processing methodology in the characterization of the mechanical properties of terrain. *Journal of Terramechanics*, 17(1):13–41, 1980.
- [14] W. Steeds. An analysis of the factors involved in steering. *Automobile Engineer*, pages 143–148, April 1950.
- [15] M. Kitano and H. Jyozaki. A theoretical analysis of steerability of tracked vehicles. *Journal of Terramechanics*, 13:241–258, 1976.
- [16] M. Kitano and M. Kuma. An analysis of horizontal plane motion of tracked vehicles. *Journal of Terramechanics*, 14:211–225, 1977.
- [17] Malay K. Kar. Prediction of track forces in skid-steering of military tracked vehicles. *Journal of Terramechanics*, 24:75–86, 1987.
- [18] W. Ehler, B. Hug, and I.C. Schmid. Field measurements and analytical models as a basis of test stand simulation of the turning resistance of tracked vehicles. *Journal of Terramechanics*, 29:57–69, 1992.
- [19] D. Rubinstein and R. Hitron. A detailed multi-body model for dynamic simulation of off-road tracked vehicles. *Journal of Terramechanics*, 41:163–173, 2004.
- [20] M. Berli, J.M. Kirby, S.M. Springman, and R. Schulin. Modeling compaction of agricultural subsoils by tracked heavy construction machinery under various moisture conditions in Switzerland. *Soil & Tillage Research*, (73):57–66, 2003.

- [21] L.L. Karafiath and E.A. Nowatzki. *Soil Mechanics For Off-Road Vehicle Engineering*. Trans Tech Publications, 1978.
- [22] D. Rowland. Tracked vehicle ground pressure and its effects on soft ground performance. *Proc. 4th Int. Conf of the International Society for Terrain Vehicle Systems*, vol. 1, 1972.
- [23] V.P. Goriatchkin. Teoria i proizvodstvo sielskohoziaynih mashin (theory and manufacturing of agricultural machines. 1936.
- [24] A.R. Reece. Principles of soil-vehicle mechanics. *Proc. Institution of Mechanical Engineers*, 180:part 2A, 1965-1966.
- [25] B.S. Chang and W.J. Baker. Soil parameters to predict the performance of off-road vehicles. *Journal of Terramechanics*, 9(2):13–31, 1973.
- [26] Bill McBride and Greg Peri. Derived performance metrics and measurements compared to field experience for the packbot. SwRI, 2002.

Vita

Javier Mateo Solis was born in McAllen, Texas on November 10, 1978, the son of Mateo Solis and Aurora Solis. After completing his work at Edinburg High School, Edinburg, Texas in 1997, he entered The University of Texas Pan-American in Edinburg. He received the degree of Bachelor of Science in Mechanical Engineering in May 2002. In September 2002, he entered the Graduate School at the University of Texas at Austin.

Permanent Address: 1407 Sevilla Blvd
Edinburg, Texas 78539

This thesis was typeset with $\text{\LaTeX} 2_{\epsilon}$ ¹ by the author.

¹ $\text{\LaTeX} 2_{\epsilon}$ is an extension of \LaTeX . \LaTeX is a collection of macros for \TeX . \TeX is a trademark of the American Mathematical Society. The macros used in formatting this thesis were written by Dinesh Das, Department of Computer Sciences, The University of Texas at Austin, and extended by Bert Kay, James A. Bednar, and Ayman El-Khashab.